LIGHT REACTIONS OF PHOTOSYNTHESIS:
EXPLORING EARLY ENERGY AND ELECTRON TRANSFERS IN
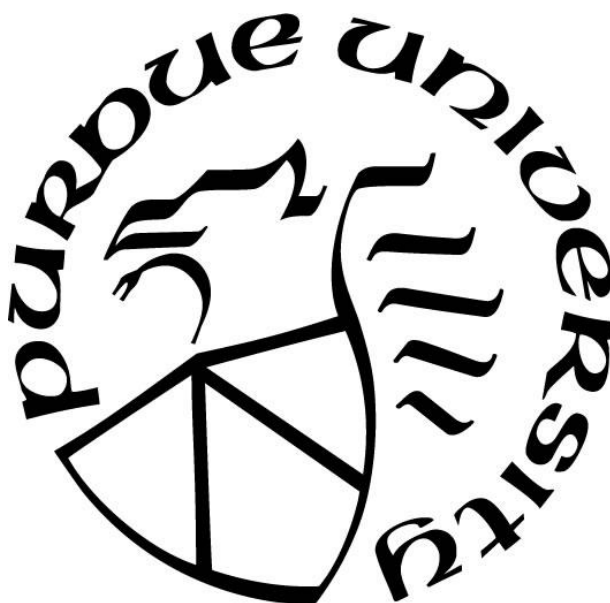# CYANOBACTERIAL PHOTOSYSTEM I VIA OPTICAL
SPECTROSCOPY

by

Antoine Pierrick Martin

A Dissertation

Submitted to the Faculty of Purdue University

In Partial Fulfillment of the Requirements for the degree of

Doctor of Philosophy

Department of Physics and Astronomy

West Lafayette, Indiana

December 2020

THE PURDUE UNIVERSITY GRADUATE SCHOOL
STATEMENT OF COMMITTEE APPROVAL

Dr. Sergei Savikhin, Chair

Department of Physics & Astronomy

Dr. Ken P. Ritchie

Department of Physics & Astronomy

Dr. Andrew Mugler

Department of Physics & Astronomy

Dr. Martin Kruczenski

Department of Physics & Astronomy

Approved by:

Dr. John P. Finley

To my family and friends, who have demonstrated love, provided support and imparted wisdom

ACKNOWLEDGMENTS

This journey through graduate school, which this document brings one step closer to completion, has been a most humbling experience; luckily, I have been blessed with support in various forms from many individuals, a few of whom shall be mentioned explicitly here.

For their steady and enthusiastic support not just in this last portion but throughout the totality of my education, my parents, Annie and Jean-Paul Martin, deserve my deepest gratitude. At the same time, I would like to thank my sister, Amandine, who, in commendable elder sibling fashion, challenged me intellectually from an early age, awakening a useful sense of skepticism.

Special thanks go to Professor Sergei Savikhin, my fearless PhD advisor, for allowing me to join his research group, introducing me to the world of photosynthesis research, explaining theory and instructing me in experimental methods. I am grateful for the comfortable leaning environment he maintained by meeting my deep ignorance with saintly patience. He has also been a role model in handling each new challenge methodically, with calm professionalism. I extend thanks to Professors Ken Ritchie, Andrew Mugler and Martin Kruczenski for taking the time to be on my committee as well.

Past and current group members have also facilitated laboratory life and the associated work. Doctors Shigeharu Kihara, Dan Hartzler and Valentyn Stadnytskyi, my most recent predecessors, welcomed me into their small community. Valentyn, whose time at Purdue overlapped substantially with mine, proactively mentored me, frequently taking the initiative to inquire about the state of my work and remaining available to assist me. I would also like to thank Zach Mitchell especially, my closest peer within the group through many shared experiences, in both research and teaching. From his generous technical assistance to our many discussions on research and diverse aspects of life, Zach has been an excellent companion, a source of solidarity and friendship extending outside the laboratory.

The experiments presented in this work would not have been possible without Professor Wu Xu and his former student, Doctor Lujun Luo, of the University of Louisiana at Lafayette, Department of Chemistry. These valuable collaborators provided all the photosystem I samples studied and deserve credit for generating figures depicting mutations in the reaction centers of these. They have also provided some useful discussions, sharing their own experimental results and biological expertise.

Within Purdue's Department of Physics & Astronomy, I would like to thank Sandy Formica and Janice Thomaz, who kindly facilitated countless administrative processes, always doing so with a smile and contagious cheerfulness.

Lastly, I have met many wonderful peers throughout my graduate studies and cultivated various friendships among them, but one deserves special mention far-above the rest: For her loving support, for her relentless encouragement, for standing right with me through these challenging years, for routinely finding ways to make life more pleasant in all circumstances, I express my profoundest thanks to my dear fiancée, Yifei He.

TABLE OF CONTENTS

LIST OF TABLES

LIST OF FIGURES

LIST OF ABBREVIATIONS

[4Fe-4S]	iron-sulfur complex
A	acceptor
A_{-1}	accessory pigment
A_0	primary electron acceptor
A_1	secondary electron acceptor
ADP	adenosine diphosphate
ascorbate	sodium L-ascorbate
Asn	asparagine
ATP	adenosine triphosphate
BBO	$\beta\text{-BaB}_2\text{O}_4$
BChl	bacteriochlorophyll
BPheo	bacteriopheophytin
CaF_2	calcium fluoride
Chl	chlorophyll
CS	charge separation/-separated
CW	continuous wave
Cyt b_6f	cytochrome b_6f complex
Cyt c_6	cytochrome c_6
D	donor
DADS	decay-associated difference spectrum
EET	excitation energy transfer
ESA	excited-state absorption
ET	electron transfer
ETC	electron transport chain
F	phenylalanine
FCWD	Franck-Condon weighted density of states
FD	ferredoxin
FNR	ferredoxin-NADP$^+$ reductase
FRET	Förster (/fluorescence) resonance energy transfer
FWHM	full width at half maximum
Gln	glutamine
GSB	green sulfur bacterium
GVD	group velocity dispersion
H	histidine
H-bond	hydrogen bond
His	histidine
IR	infrared
L	leucine
Leu	leucine
M	methionine
Met	methionine
Mg^{2+}	double magnesium ion
MOPS	3-(N-morpholino)propanesulfonic acid

N	asparagine
$NADP^+$	nicotinamide adenine dinucleotide phosphate
NADPH	reduced $NADP^+$
O_2	molecular oxygen
OPA	optical parametric amplifier
P	products
P_{700}	special pair in PS I RC
PB	photobleaching
PC	plastocyanin
Phe	phenylalanine
Pheo	pheophytin
PhQ	phylloquinone
P_i	phosphate group
PMS	N-Methylphenazonium methyl sulfate
PQ	plastoquinone
PQH_2	plastoquinol
PS I	photosystem I
PS II	photosystem II
Q	glutamine
R	reactants
RC	reaction center
RMS	root mean square
S	serine
S. sp. PCC 6803	*Synechocystis* sp. PCC 6803
SE	stimulated emission
Ser	serine
SHE	standard hydrogen electrode
Trp	tryptophan
Tyr	tyrosine, tyrosyl
UV	ultraviolet
W	tryptophan
Y	tyrosine, tyrosyl

ABSTRACT

Early processes following photon absorption by the photosynthetic pigment-protein complex photosystem I (PS I) have been the subject of decades of research, yet many questions remain in this area of study. Among the trickiest to investigate is the role of the PS I reaction center's (RC's) two accessory (A_{-1}) chlorophyll (Chl) cofactors as primary electron donors or acceptors, oxidizing the special pair (P_{700}) of Chls or reducing a nominal primary electron acceptor (A_0) Chl in the first electron transfer step. Such processes, which occur on a picosecond timescale, have long been studied via ultrafast spectroscopy, though difficulty lies in distinguishing among signals from early processes, which have similar lifetimes and involve many identical pigments. In this work, we used steady-state and ultrafast optical pump-probe spectroscopies on PS I trimers from wildtype and mutant strains of the cyanobacterium *Synechocystis* sp. PCC 6803 in which an asparagine amino acid residue near A_{-1} had been replaced with methionine on one or both sides of the RC. We also conducted an identical set of experiments on mutants in which A_0 was similarly targeted, as well as studied the effects on the A_0 absorption spectrum of a third category of mutations in which a peripheral H-bond to A_0 was lost. Steady-state absorption spectroscopy revealed that many of these mutations caused mild Chl deficiencies in the light-capturing antenna of PS I without necessarily preventing organisms' growth. More importantly, we determined that contrary to certain hypotheses, A_{-1} is the most likely true first electron acceptor, as reasoned from observing rapid triplet state formation in double A_{-1} mutants. We also concluded from non-additive detrimental effects of single-side mutations that if one RC branch is damaged at the level of A_0 or A_{-1}, electron transfer may be redirected along the intact branch. This may help explain the conservation of two functional RC branches in PS I over many generations of natural selection, despite the additional cost to organisms of manufacturing both.

CHAPTER 1.   INTRODUCTION TO PHOTOSYNTHESIS

Photosynthesis is the process whereby plants, algae and certain bacteria harvest light energy and convert it into a more durable form by storing it in chemical bonds. Oxygenic photosynthesis, such as performed by plants, produces molecular oxygen, O_2, as a byproduct, which countless species require for cellular respiration. Photosynthesis therefore supports nearly all life on Earth both for the organisms that use it themselves and for heterotrophic and oxygen-breathing organisms such as humans, depending on plants as a source of both sustenance and oxygen.

1.1   Light Reactions & Dark Reactions

Photosynthetic reactions can be classified into two categories: light reactions and dark reactions. The light reactions use light energy in a process which splits water (H_2O), reduces nicotinamide adenine dinucleotide phosphate ($NADP^+$), assembles adenosine triphosphate (ATP) from adenosine diphosphate (ADP) and a phosphate group (P_i), produces two protons (H^+), and releases O_2. These reactions can be summarized by

$$2H_2O + 2NADP^+ + 3ADP + 3P_i \xrightarrow{\hbar\omega} O_2 + 2H^+ + 2NADPH + 3ATP, \tag{1.1}$$
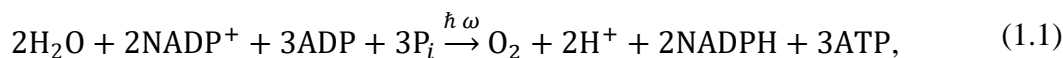
where NADPH is the reduced form of $NADP^+$ (note that $NADP^+$ must accept two electrons and one proton to achieve this reduced form). In the dark reactions, carbon from the environment is fixed and a phosphorylated sugar is produced using products from the light reactions. This can be represented by

$$3CO_2 + 6NADPH + 5H_2O + 9ATP \rightarrow G_3P + 2H^+ + 6NADP^+ + 9ADP + 8P_i, \tag{1.2}$$
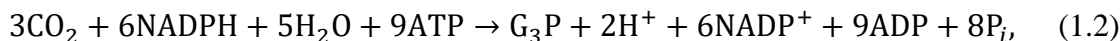
where G_3P denotes glyceraldehyde-3-phosphate, a three-carbon sugar phosphate molecule. Combining Equations (1.1) and (1.2) gives the overall oxygenic photosynthesis equation:

$$n\,H_2O + n\,CO_2 \xrightarrow{\hbar\omega} (CH_2O)_n + n\,O_2. \tag{1.3}$$
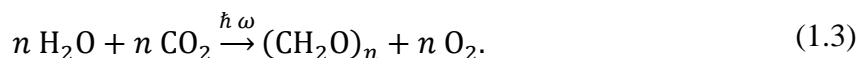
The remainder of this chapter focuses on the light reactions as these are the portion of photosynthesis under investigation in this work.

Green plants' cells contain chloroplasts, organelles in which photosynthesis takes place (Blankenship, 2013). Each chloroplast contains a thylakoid membrane bathed in one fluid, the stroma, and containing another, the lumen. The stromal side of the membrane is also called the negative or n-side as it accumulates a net negative charge in the process of photosynthesis, and likewise, the luminal side accumulates protons (H^+ products from Equations (1.1) and (1.2)) and is called the positive or p-side. The light reactions also take place on the thylakoid membrane in cyanobacteria and algae. Four main transmembrane proteins responsible for the light reactions are embedded throughout the thylakoid membrane: photosystem II (PS II), cytochrome b_6f (Cyt b_6f), photosystem I (PS I) and ATP synthase, the first three of which are illustrated in Figure 1.1.
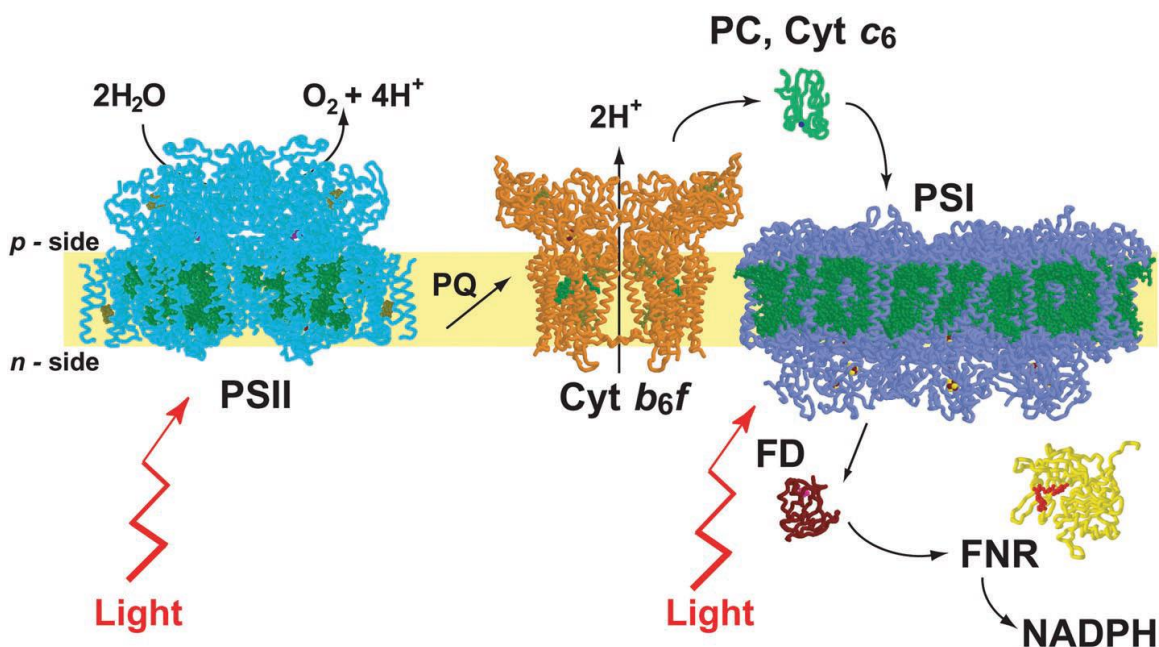
Figure 1.1 PS II dimer (blue), Cyt b_6f (orange) and PS I trimer (violet) (from left to right) are embedded in the thylakoid membrane (pale yellow). These proteins create the electrochemical gradient which powers ATP synthesis. Also shown are light reaction steps (see text), as well as electron carriers plastoquinone (PQ), plastocyanin (PC, found in plants), cytochrome c_6 (Cyt c_6, common in cyanobacteria and algae) (De la Rosa et al., 2006), and ferredoxin (FD). Ferredoxin-NADP$^+$ reductase (FNR), shown in yellow, is an enzyme catalyzing the reduction of NADP$^+$ to NADPH by FD. This representation is by Kurisu et al. (2003), incorporating PS II and PS I structures from Kamiya & Shen (2003), Zouni et al. (2001), and Jordan et al. (2001).

PS II, also known as water-plastoquinone oxidoreductase, uses light energy to split water, obtaining electrons on the p-side of the membrane. Each split water molecule yields two electrons, two protons and one oxygen atom. Absorption of a photon by PS II initiates charge transport along a chain of specialized molecules. PS II gives two electrons from the p-side to small organic

20

electron carrier plastoquinone (PQ), which also collects two H^+ from the *n*-side, becoming plastoquinol (PQH$_2$). Upon formation, PQH$_2$ leaves PS II and diffuses through the membrane until it docks to Cyt b_6f on the *p*-side of the membrane. Here, it releases its two H^+, effectively transporting two protons across the membrane from the stroma to the lumen and building an electrochemical gradient across the membrane, which drives ATP synthase. Furthermore, Cyt b_6f transports two additional protons from the stroma to the lumen via a cyclic process that also involves PQ and PQH$_2$. The electrons released by PQH$_2$ at the Cyt b_6f docking site are transported concurrently to the protein plastocyanin (PC), on the *p*-side and, on the *n*-side, reduce the soluble electron-carrying protein ferredoxin (FD) or flavodoxin (Chitnis, 2001), which in turn reduces NADP$^+$, as seen in Equation (1.1). PC then reduces PS I (Sétif, 2001) which, like PS II, requires an absorbed photon's energy to donate an electron.
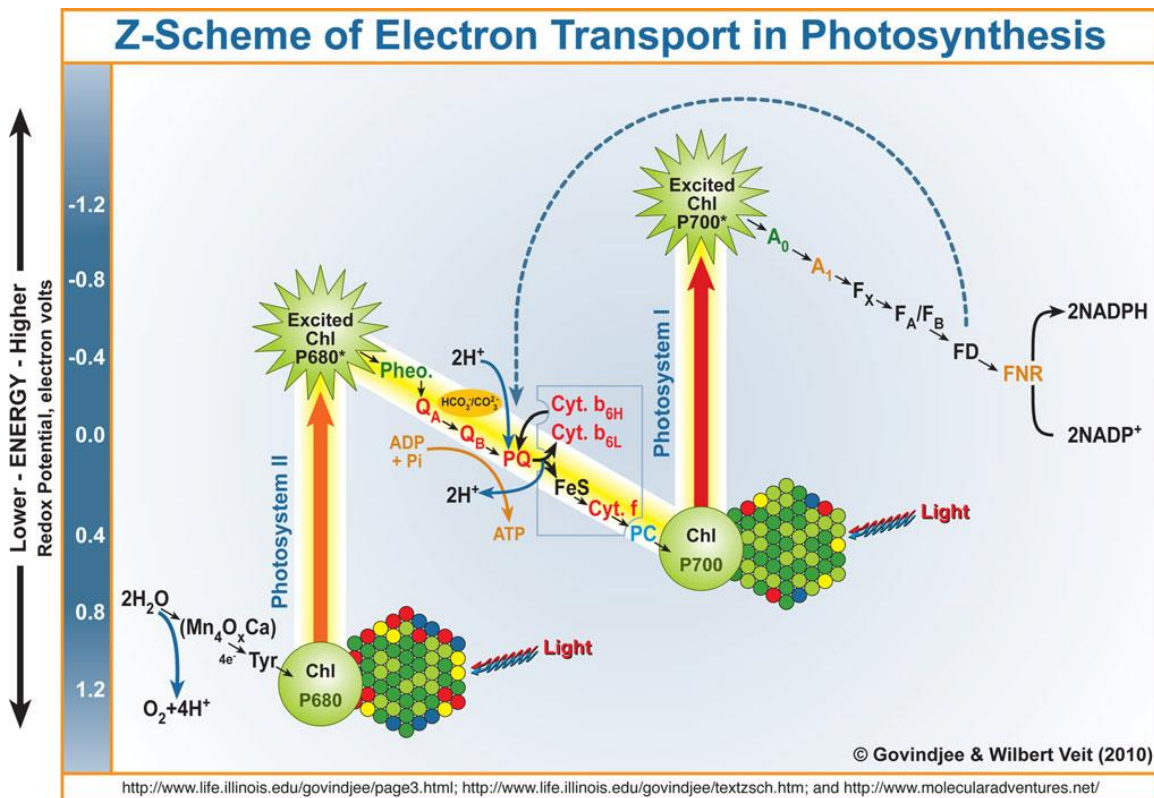
Figure 1.2: Z-scheme of electron transport in photosynthesis (Orr & Govindjee, 2010)

Details of electron transfer mechanisms within PS I are the crux of the research presented here and will therefore be discussed at length in upcoming sections and later chapters. The electron transport chain (ETC) described so far, from H$_2$O split by PS II through PS I to NADP$^+$, can be

visualized as the Z-scheme pictured in Figure 1.2. The electrochemical gradient generated by PS II, Cyt b_6f and PS I throughout these processes powers the rotation of ATP synthase by which ATP is produced (Velthuys, 1980). The flow of protons from the p-side to the n-side through ATP synthase's proton channel is coupled to the rotary motion of its asymmetric γ subunit resulting in the assembly of ADP and P_i by the surrounding β subunits.

1.2   Chlorophyll

Pigment	Abbreviation	R_3	R_7	R_8	R_{12}	$R_{13}^2\alpha$	$R_{13}^2\beta$	R_{17}^3	R_{20}	M	Rem.
Chlorophyll a	Chl a	C_2H_3	CH_3	C_2H_5	CH_3	$COOCH_3$	H	Phy	H	Mg	a)
Chlorophyll a'	Chl a'	C_2H_3	CH_3	C_2H_5	CH_3	H	$COOCH_3$	Phy	H	Mg	
[8-Vinyl]-chlorophyll a	[8-Vinyl]-Chl a	C_2H_3	CH_3	C_2H_3	CH_3	$COOCH_3$	H	Phy	H	Mg	b)
[8-Hydroxyethyl]-chlorophyll a_F	[8-Hydroxyethyl]-Chl a_F	C_2H_3	CH_3	C_2H_4OH	CH_3	$COOCH_3$	H	Farn	H	Mg	
Chlorophyll b	Chl b	C_2H_3	CHO	C_2H_5	CH_3	$COOCH_3$	H	Phy	H	Mg	
[8-Vinyl]-chlorophyll b	[8-Vinyl]-Chl b	C_2H_3	CHO	C_2H_3	CH_3	$COOCH_3$	H	Phy	H	Mg	b)
Chlorophyll d	Chl d	CHO	CH_3	C_2H_5	CH_3	$COOCH_3$	H	Phy	H	Mg	
Chlorophyll d'	Chl d'	CHO	CH_3	C_2H_5	CH_3	H	$COOCH_3$	Phy	H	Mg	
Pheophytin a	Phe a	C_2H_3	CH_3	C_2H_5	CH_3	$COOCH_3$	H	Phy	H	H_2	
Bacteriochlorophyll c	BChl c	$CHOH-CH_3$	CH_3	$CH_2CH_n(CH_3)_{3-n}$	CH_3/C_2H_5	H	H	Farn/others	CH_3	Mg	c)
Bacteriochlorophyll d	BChl d	$CHOH-CH_3$	CH_3	$CH_2CH_n(CH_3)_{3-n}$	CH_3/C_2H_5	H	H	Farn/others	H	Mg	c)
Bacteriochlorophyll e	BChl e	$CHOH-CH_3$	CHO	$CH_2CH_n(CH_3)_{3-n}$	CH_3/C_2H_5	H	H	Farn/others	CH_3	Mg	c)
Bacteriochlorophyll f	BChl f	$CHOH-CH_3$	CHO	$CH_2CH_n(CH_3)_{3-n}$	CH_3/C_2H_5	H	H	Farn/others	H	Mg	d)

Figure 1.3: Summary of different types of Chl and BChl (Scheer, 2006). The Q_y transition moment lies nearly along the axis connecting the nitrogen atoms of rings A and C (van Gurp et al., 1989).

Before discussing the structure and function of either photosystem, it is important to understand certain properties of chlorophyll (Chl), pigment ubiquitous in these complexes. A Chl molecule's basic structure is a chlorin ring surrounding a doubly ionized metal atom, usually magnesium (Mg^{2+}). Without this central Mg^{2+}, the pigment is known as pheophytin (Pheo), as found in the PS II RC. Some bacteria also possess their own brands of these pigments: bacteriochlorophyll (BChl) and bacteriopheophytin (BPheo). Chl's chlorin ring has a variety of possible side chains attached, each defining a corresponding type of Chl, as shown in the chart in Figure 1.3; these side chains determine the different Chls' absorption spectra (Scheer, 2006). Chl a,

for instance, is the dominant pigment in PS I and virtually the only Chl type found in this complex, the only exception being one Chl *a*' epimer in the RC (Chitnis, 2001). Like all other Chls, it has an absorption band in the ultraviolet (UV) – blue range—a Soret band—and one in the red – infrared (IR) range—a Q_y band. The Q_y band corresponds to transitions along the Q_y axis, oriented approximately along the line passing through the nitrogen atoms of rings A and C (van Gurp et al., 1989). These absorption bands may broaden or shift when Chls, which are hydrophobic, reside together in their natural protein environments.

1.3   Photosystems I & II

Each photosystem is a pigment-protein complex in which an antenna array containing many pigments surrounds an RC where charge separation (CS) takes place. Upon absorbing a photon, an antenna pigment becomes excited, and an outer electron is promoted to a higher-energy orbital. Thanks to the proximity of other nearby antenna pigments and to dipole-dipole interactions, this excitation is transferred from one pigment to another via Förster resonance energy transfer (FRET). Energy is thus funneled all the way to a strongly coupled pair of Chls *a*, called special pair, in the RC (Nelson & Junge, 2015). Upon excitation, the special pair initiates electron transfer (ET) over a series of cofactors until a terminal electron acceptor is reached. RCs are classified into two types according to their terminal electron acceptors: Fe-S-type or type I RCs use iron sulfur complexes [4Fe-4S], whereas Q-type or type II RCs use quinone-type electron acceptors. Both RC types and their corresponding photosystems are necessary for oxygenic photosynthesis, but green sulfur bacteria (GSB) and heliobacteria also possess type I RCs (Savikhin & Jankowiak, 2014). The research presented in this work pertains to PS I and type I RCs; hence, Section 1.4 provides a more detailed description of these.

1.4 Photosystem I and Type I Reaction Centers

1.4.1 Photosystem I Structure
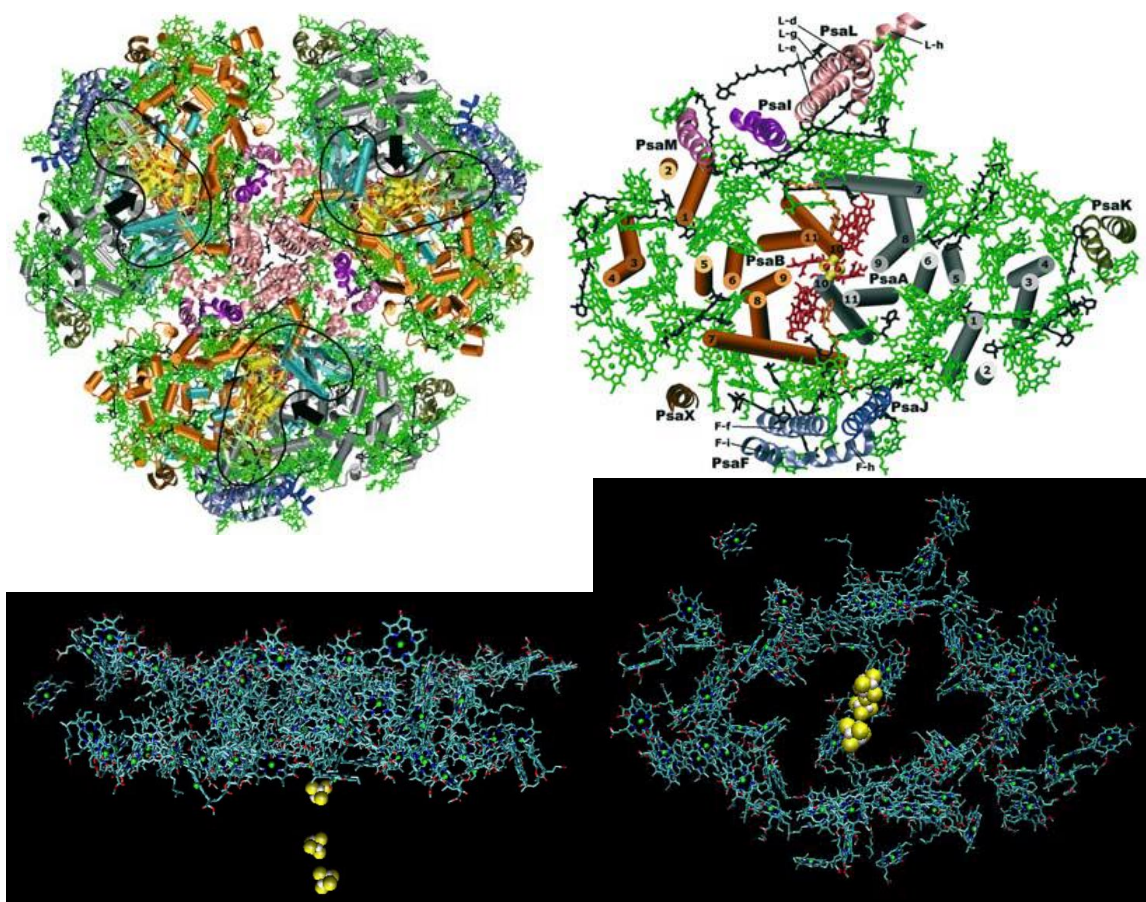
Figure 1.4 : A PS I trimer (top left) and one of its constituent monomers (top right) are shown from the *n*-side of the membrane (Grotjohann & Fromme, 2005). The protein subunits appear as collections of cylinders and helices, whereas Chls appear green. The arrangement of energy and electron transfer cofactors alone is shown in the bottom panels, from within the membrane (left) and from the *n*-side (right) (Jordan et al., 2001).

PS I, also known by its function as plastocyanin-ferredoxin oxidoreductase, is the twofold rotationally pseudosymmetric pigment-protein complex depicted in Figure 1.4, which uses light energy to reduce FD or flavodoxin (Golbeck & Bryant, 1991; Sétif, 2001). Its X-ray crystallographic structure has been determined for thermophilic cyanobacterium *Synechococcus elongatus* with 2.5 Å resolution (Grotjohann & Fromme, 2005; Jordan et al., 2001), and for plants, with up to 3.3 Å resolution (Amunts, Drory, & Nelson, 2007; Amunts, Toporik, et al., 2010). It comprises 12 protein subunits bound non-covalently to 127 cofactors. Among these are 96 Chls *a*

of which 90 belong to an antenna array which also includes 22 β-carotene molecules, organic pigments appearing red-to-yellow in hue. A large majority of antenna Chls are found along the membrane's inner and outer surfaces, with each Chl's three nearest neighbors within 15 Å of it, on average (Jordan et al., 2001; Savikhin, 2006). PS I additionally contains 2 phylloquinones (PhQ), 3 [4Fe-4S] complexes, 4 lipids and 201 water molecules as well as a Ca^{2+} ion. Unlike eukaryotic PS I, which tends to remain monomeric, cyanobacterial complexes typically form trimers within the membrane (Chitnis, 2001; Kouřil et al., 2005), also shown in Figure 1.4 (Grotjohann & Fromme, 2005). An absorbance spectrum of PS I trimers suspended in solution is shown in Figure 1.5.
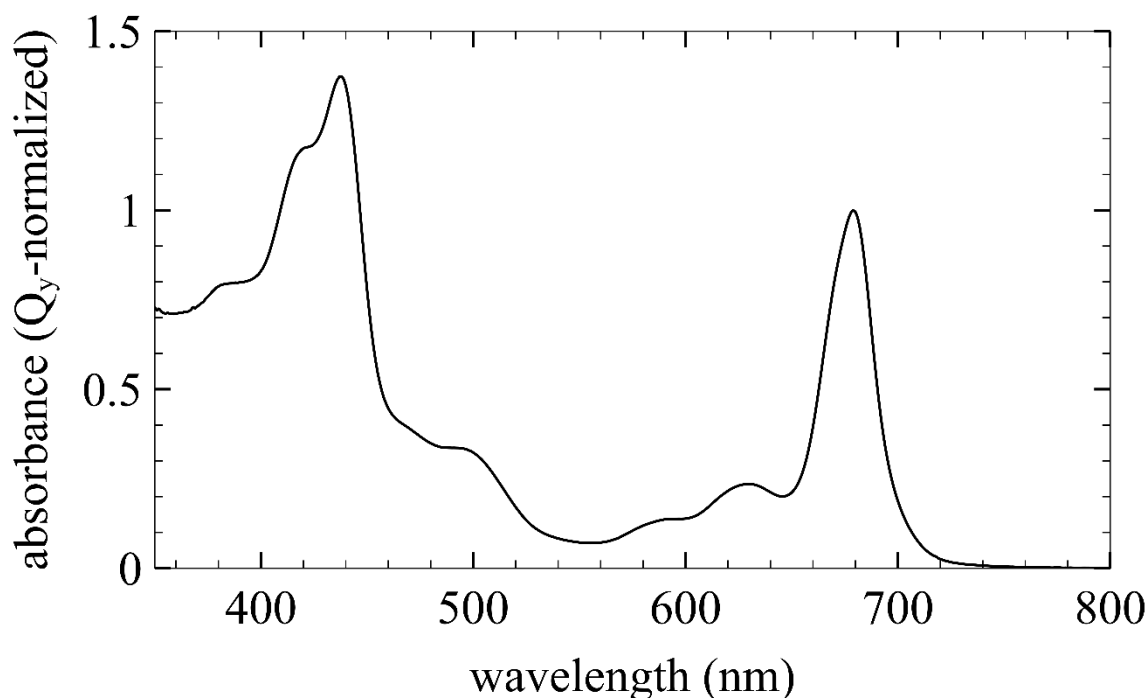
Figure 1.5: PS I steady-state absorbance normalized to unity in Q_y region. The absorption band centered around 679 nm, 27 nm FWHM, is due to 96 Chls *a* in both the antenna and the RC which, because they are not spectrally resolved, makes it challenging to study ET dynamics in the RC alone, which contains only 6 of these Chls *a*.

1.4.2 PS I Reaction Center Structure
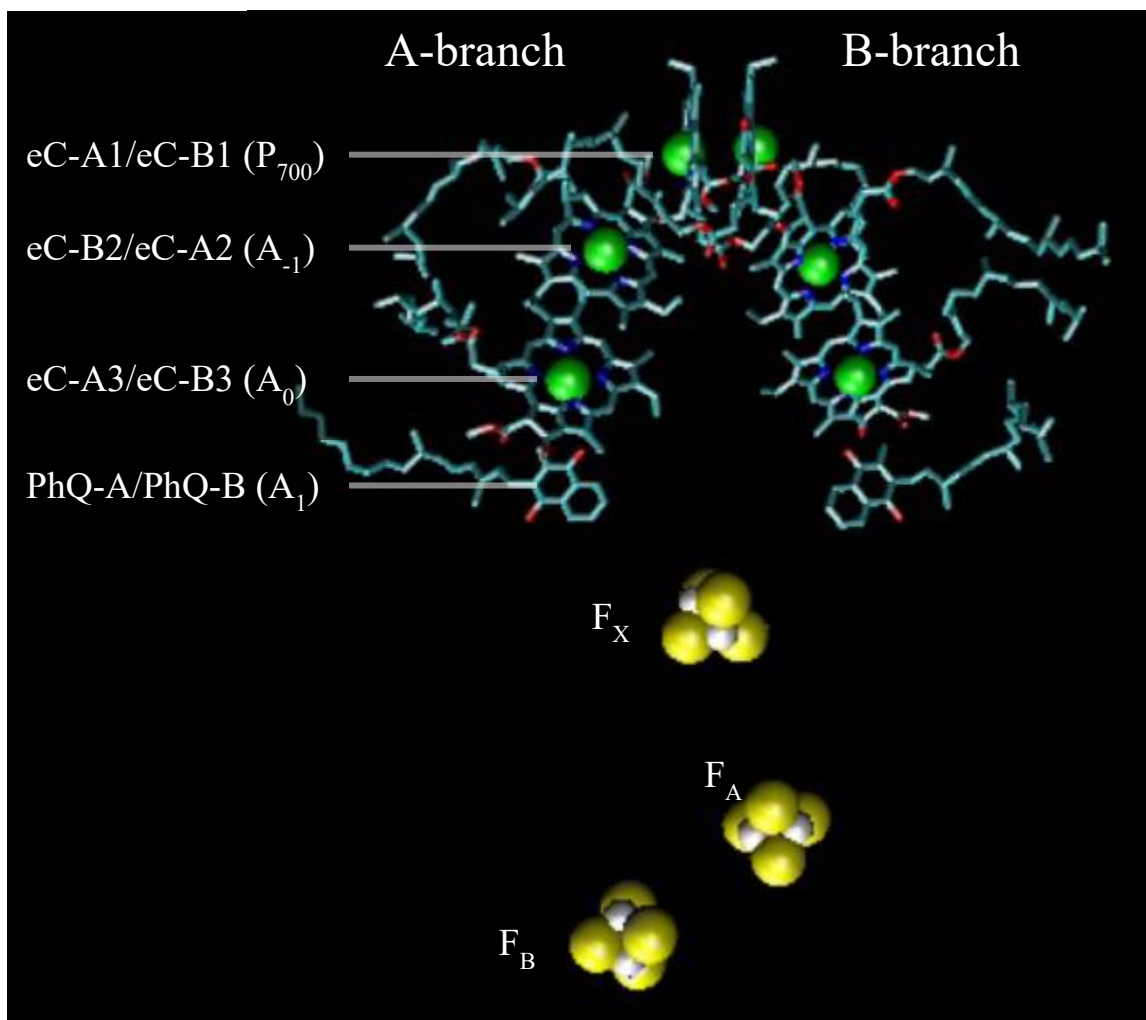
Figure 1.6: The Type I RC is depicted based on the structure by Jordan et al. (2001). With this diagram's orientation, electrons should flow downward.

At the center of PS I is the RC, which contains the remaining six Chls a including C-13^2 epimer Chl a', as well as both PhQs, and all three [4Fe-4S] complexes, arranged in two pseudo-C_2 symmetric branches, as shown in Figure 1.6 (Jordan et al., 2001). The two branches are labeled A and B in reference to PsaA and PsaB, respectively, the major subunits which bind most of these branches' cofactors. A Chl a'/Chl a heterodimer constitutes the special pair, from which the branches diverge. The special pair is denoted P_{700} for its absorption peak at 700 nm. This is, curiously, still farther blue than about 10 so-called "red" antenna Chls, whose purpose remains under investigation (Hayes et al., 2000; Jordan et al., 2001; Pålsson et al., 1998). The Chl a' and

Chl *a* of P_{700} are denoted eC-A1 and eC-B1, respectively, where A and B again refer to the binding protein subunits. The next two Chls are accessory pigments (A_{-1}) eC-B2 and eC-A2 (note the crossover of binding subunits), followed by primary electron acceptors (A_0) eC-A3 and eC-B3. PhQ-A and PhQ-B serve as secondary electron acceptors (A_1). Note that the customary designations "accessory" and "primary/secondary electron acceptor" are somewhat misleading for reasons exposed in Section 1.4.3, but the associated spectroscopic notation for the corresponding cofactors (A_{-1}, A_0, A_1) will still be used throughout this work. The branches converge back at the first [4Fe-4S] complex, F_X, which both PsaA and PsaB coordinate (Grotjohann & Fromme, 2005; Jordan et al., 2001). F_A and F_B, the next two [4Fe-4S] complexes, are coordinated by subunit PsaC and considered terminal electron acceptors (Brettel, 1997; Høj et al., 1987). Two so-called "connecting Chls"—antenna Chls aC-A40 and aC-B39, especially close (~10 Å) to PhQ-A and PhQ-B, respectively—are thought to help EET proceed from the antenna to the RC (Dashdorj, Xu, Martinsson, et al., 2004; Gibasiewicz, Ramesh, Lin, Redding, et al., 2003; Jordan et al., 2001).

1.4.3 Excitation Trapping & Electron Transfer in PS I

Experiments using various spectroscopic techniques have revealed a significant portion of what is known about excitation energy transfer (EET) and ET in PS I and its RC, as will be discussed in the remainder of this section. Ultrafast spectroscopy has shed light on ET rates in the primary CS events. Here, it is useful to distinguish between two types of rate constants. Effective rate constants, which such experiments can measure, are the rates at which redox states become populated as a result of all processes combined. Intrinsic rate constants, on the other hand, are the rates at which individual ET proceeds from one cofactor to another in the hypothetical absence of all other processes; hence, they are studied principally via modeling. The reciprocal of a rate constant is a time constant (Gatzen et al., 1996; Müller, Niklas, et al., 2003; Savikhin & Jankowiak, 2014).

In addition to the practical unfeasibility of isolating individual ET processes, experimental investigation of these in PS I presents the challenge of spectral congestion (Savikhin & Jankowiak, 2014). All 96 of PS I's Chls, in both the antenna and the RC, are Chl *a*. Together, they give PS I its broad (~30 nm) Q_y absorption band centered around ~680 nm, (see Figure 1.5). Spectroscopy experiments probing within this band see dynamics associated mostly with processes involving antenna Chls, which outnumber RC Chls fifteenfold, making the data difficult to untangle. To

worsen matters, the antenna excitation typically decays in tens of picoseconds, the same timescale on which CS occurs in the RC. Furthermore, preferential excitation of P_{700}, which might initiate CS, is impossible as an overwhelming majority of the absorption at 700 nm is due to antenna Chls. Unlike in PS II, the antenna and RC Chls in PS I are indissociable because most of them are bound by the same pair of protein subunits, PsaA and PsaB, which can therefore not be removed while keeping the RC intact. Harsh chemical treatments have been used to remove most antenna Chls, but these undermine the complex's integrity and function, influencing experimental results (Kumazaki, Ikegami, et al., 2001; Kumazaki, Iwaki, et al., 1994; Kumazaki, Kandori, et al., 1994). Low-temperature studies of type I RCs from GSB with much smaller immediate antennas and BChl a special pairs P_{840} have also been attempted (Chauvet, Jagannathan, et al., 2009).

Despite these obstacles, a significant amount has already been learned about excitation trapping and ET in PS I. Based on the proximity of antenna Chls to their nearest few neighbors, EET between consecutive pigments has been estimated to occur in ~200 fs (Du et al., 1993; Owens et al., 1987; Struve, 1995). Effective energy trapping by the antenna, in contrast, occurs on a much longer scale, 20 – 50 ps depending on the species and, in particular, on the antenna's red Chl content (see, for example, Gibasiewicz, Ramesh, Lin, Woodbury, et al. (2002), Gobets and van Grondelle (2001), Gobets et al. (2001), Hastings, Kleinherenbrink, et al. (1994), Melkozernov et al. (1997), Savikhin (2006), Savikhin, Xu, Chitnis, & Struve (2000)). Unlike in the PS II RC, CS in the PS I RC has been observed to take place along either branch, though the ratio of A-branch CS to B-branch CS varies across species, with the A-branch favored more strongly in prokaryotes than in eukaryotes (Bautista et al., 2005; Cardona et al., 2012; Cohen et al., 2004; Guergova-Kuras et al., 2001; Joliot & Joliot, 1999; Muhiuddin et al., 2001; Ramesh et al., 2004; Redding & van der Est, 2006; Santabarbara, Kuprov, et al., 2005; Xu et al., 2003). A recent study by Badshah et al. (2018) involving mutants of both algal and cyanobacterial PS I has observed ET proceeding independently along each branch. CS begins when excitation from a nearby antenna pigment reaches P_{700}, promoting one of its outer electrons to a higher-energy orbital. This additional energy, combined with the proximity among RC Chls, allows the excited electron to effectively be transferred from P_{700} to A_0, forming a $P_{700}^+A_0^-$ ion pair. Because the ~20 Å separation between P_{700} and A_0 is deemed too great to permit direct ET (Moser & Dutton, 2006; Santabarbara, Heathcote, & Evans, 2005), involvement of the intermediate A_{-1} is inferred, though its specific role remains under investigation. It may well be that A_{-1} is the actual first electron acceptor or

donor, making the true primary CS state either $P_{700}^+A_{-1}^-$ or $A_{-1}^+A_0^-$, respectively, followed by the aforementioned $P_{700}^+A_0^-$ state (Müller, Niklas, et al., 2003; Müller, Slavov, et al., 2010; Rappaport et al., 2006). A third possibility is that the true first electron acceptor is the dimer $A_{-1}A_0$ on either branch (Shelaev et al., 2010). However, none of these hypotheses has been conclusively confirmed by experiments. Excitation trapping and formation of $P_{700}^+A_0^-$ have been measured to take 20 – 30 ps, though the intrinsic time for this ET step is thought to be only ~0.1 – 3 ps (Brettel, 1997; Brettel & Leibl, 2001; Hastings, Kleinherenbrink, et al., 1994; Savikhin, 2006; Shelaev et al., 2010; White et al., 1996). Spectroscopic experiments probing in A_1's near-UV absorption band have monitored the $A_0^-A_1 \rightarrow A_0A_1^-$ step directly, finding intrinsic times anywhere within the 13 – 50 ps range (Brettel, 1997; Brettel & Leibl, 2001; Brettel & Vos, 1999; Hecks et al., 1994; Savikhin, 2006; Savikhin, Xu, Martinsson, et al., 2001). The ET step to F_X is the only one whose rate is observed to depend so sensitively on which RC branch is involved: PhQ-A$^- \rightarrow F_X$ takes ~200 ns, whereas PhQ-B$^- \rightarrow F_X$ takes only ~20 ns (Brettel, 1988; Joliot & Joliot, 1999; Mathis & Sétif, 1988; Sétif & Brettel, 1993). Tentative explanations for this discrepancy include that of Berthold et al. (2012), who suspect the involvement of a strong hydrogen bond (H-bond) on the A-side but not the B-side between A_1^- and the protein backbone. Despite this faster F_X reduction rate from PhQ-B, most ET proceeds along the A-branch (Savikhin & Jankowiak, 2014; Sétif & Brettel, 1993). Terminal acceptors F_A and F_B are each reduced within 500 ns (Brettel & Leibl, 2001; Diaz-Quintana et al., 1998; Sétif & Bottin, 1994).

1.4.4   Properties of Reaction Center Cofactors

Spectroscopic properties of RC cofactors have also been studied. In experiments in which P_{700} was oxidized or A_0 reduced, absorption spectra compared with those in which these pigments were in their neutral states have revealed P_{700}'s ~30 nm-wide absorption band centered around 700 nm as well as a narrower (~10 nm FWHM) band at 690 nm, ascribed to the neutral Chl monomer C690 of P_{700}^+, and a broad band from the Chl$^+$ centered around 800 nm. Absorbance at 684 – 687 nm has been attributed to A_0 based on a bleaching band observed in (A_0^- - A_0) spectra (Chauvet, Dashdorj, et al., 2012; Hastings, Kleinherenbrink, et al., 1994; Savikhin, Xu, Martinsson, et al., 2001). Chauvet, Dashdorj, et al. (2012) have found a Q_y absorption band at 682 nm for A_{-1}, though this remains to be confirmed. Byrdin, Jordan, et al. (2002) and Damjanović et al (2002) have also attempted to predict transition energies of these and all PS I antenna Chls via different

techniques using the PS I structure by Jordan et al. (2001), but this has produced still different results. The A_1 PhQ has an absorption feature near 380 nm, sometimes used to monitor its redox state, but later electron acceptors, the [4Fe-4S] complexes, do not absorb in the visible range (Brettel, 1988; Brettel & Vos, 1999; Savikhin, 2006).

Redox potentials of cofactors along the ETC including in PS I have been studied in a number of experiments and are also summarized in Figure 1.2 (Nelson & Yocum, 2006; Orr & Govindjee, 2010). The midpoint potential $E_m(P_{700}/P_{700}^+)$ of P_{700}, has been measured via spectroelectrochemistry to land in the range +398 – +470 mV with respect to the standard hydrogen electrode (SHE), depending on the species (Krabben et al., 2000; Mamedov et al., 1996; Nakamura et al., 2005, 2011; Witt et al., 2002). This value plunges to around -1320 mV for the excited P_{700} (P_{700}^*) (Fromme et al., 2001; Ptushenko et al., 2008). Delayed fluorescence and electroluminescence methods place $E_m(A_0/A_0^-)$ between -1290 mV and -1010 mV relative to SHE (Kleinherenbrink et al., 1994; Krabben et al., 2000; Ptushenko et al., 2008; Savikhin & Jankowiak, 2014; Shuvalov, 1976; Vos & van Gorkom, 1988). A difference between the two A_1 cofactors' redox potentials—-531 mV for PhQ-A and -686 mV for PhQ-B, as calculated by Ishikita and Knapp (2003)—may help to explain the much slower ET from the former to F_X (-705 – -660 mV), according to Santabarbara, Heathcote, and Evans (2005). Based on room-temperature redox titration and low-temperature EPR studies the redox potentials of F_A and F_B have been reported as -540 mV and -590 mV, respectively (Brettel, 1997). F_A's higher redox potential, despite F_B's greater proximity to FD, justifies the classification of both cofactors as terminal electron acceptors. Note that these redox potentials all depend intimately on their respective cofactors' environments, which mutations can significantly alter, as explored in the experiments presented in CHAPTER 4.

CHAPTER 2.   THEORY

This chapter lays out some theoretical framework useful for understanding the experiments and interpreting their results, all described in later chapters. Section 2.1 discusses properties of individual chromophores, namely in terms of their interactions with light. Section 2.2 outlines possible events which typically follow excitation, including energy transfer between pigments weakly coupled via dipole-dipole interactions, such as is common among PS I antenna Chls. Excitons resulting from strong dipole-dipole interactions are covered in Section 2.3, followed by electron transfer, in Section 2.4, as both concepts pertain to events in the PS I RC. Finally, principles of pump-probe spectroscopy whereby some of these processes can be monitored are covered in Section 2.5

2.1   Light-Matter Interactions

The following is based on van Amerongen et al. (2000), which also offers a more complete introduction to the exciton concept. A molecule—or more specifically, a pigment such as Chl, as is of interest in this work—in the absence of all external influences, has a set of excited states and corresponding excited state wave functions φ^i with energies E^i, where the superscript i denotes the ith excited state, with $i = 0$ being the ground state. This can be represented by a Hamiltonian H_0 satisfying

$$H_0\varphi = E\varphi \tag{2.1}$$

This Hamiltonian will be modified in the presence of light as an electromagnetic wave whose electric field $\boldsymbol{E}$ can be described by

$$\boldsymbol{E} = \boldsymbol{E}_0 \cos(\boldsymbol{k} \cdot \boldsymbol{r} - \omega t), \tag{2.2}$$

where $\boldsymbol{E}_0$ specifies both the wave's amplitude and polarization, $\boldsymbol{k}$ is the wave vector, $\boldsymbol{r}$ denotes position, ω is the angular frequency, and t is time. The full Hamiltonian is

$$H = H_0 + H_1, \tag{2.3}$$

where H_1 accounts for the light's interaction with the pigment by virtue of its electric charge distribution. For an electrically neutral pigment with dipole moment $\boldsymbol{\mu}$, the dominant term in this interaction is $-\boldsymbol{E} \cdot \boldsymbol{\mu}$, justifying the approximation

$$H_1 = -\boldsymbol{E} \cdot \boldsymbol{\mu}. \tag{2.4}$$

Considering only the pigment's ground state and first excited state, and applying Fermi's golden rule under the assumption that the light's wavelength far exceeds the pigment's size, the rate of light absorption W_{01} is approximated

$$W_{01} \sim E_0^2 \left| \widehat{\boldsymbol{E}} \cdot \langle \varphi^1 | \boldsymbol{\mu} | \varphi^0 \rangle \right|^2 = |\boldsymbol{E}_0|^2 |\boldsymbol{\mu}_{01}|^2 \cos^2\left(\widehat{\boldsymbol{E}} \cdot \widehat{\boldsymbol{\mu}} \right), \tag{2.5}$$

where $\widehat{\boldsymbol{E}}$ and $\widehat{\boldsymbol{\mu}}$ denote the unit vectors in the respective directions of $\boldsymbol{E}$ and $\boldsymbol{\mu}$, and $\boldsymbol{\mu}_{01}$ is the electric transition dipole moment. Assuming no preferred direction, the expectation value of the last factor is

$$\langle \cos^2\left(\widehat{\boldsymbol{E}} \cdot \widehat{\boldsymbol{\mu}} \right) \rangle = \frac{1}{3}. \tag{2.6}$$

The transition dipole strength D_{01}, which indicates absorption band intensity, can be inferred experimentally by

$$D_{01} = |\boldsymbol{\mu}_{01}|^2 = 9.180 \cdot 10^{-3} \int \frac{\varepsilon(\omega)}{\omega} \, d\omega \, \mathrm{D}^2, \tag{2.7}$$

where $\varepsilon(\omega)$, the empirically determined molar extinction coefficient, is in units of $\mathrm{M}^{-1} \cdot \mathrm{cm}^{-1}$, the integral is evaluated over a range of frequencies corresponding to the absorption band of interest, and D denotes the CGS unit *debye* ($1\,\mathrm{D} = 10^{-18} \cdot \mathrm{cm}^{5/2} \cdot \mathrm{g}^{1/2} \cdot \mathrm{s}^{-1}$). Each state, ground or excited, is described by a time-dependent wave function whose square gives a time-independent electron distribution. However, when two states are superimposed, this distribution does oscillate at a frequency dictated by the difference ΔE between the states' energies. The Beer-Lambert law relates a sample's absorbance $A(\omega)$ to the light intensities $\mathcal{I}_0$ and $\mathcal{I}$ incident upon and transmitted through it, respectively, as well as the molar concentration C of pigments, the pathlength ℓ through the sample, and $\varepsilon(\omega)$:

$$A(\omega) = \log \frac{\mathcal{I}_0}{\mathcal{I}} = C \varepsilon(\omega) \ell. \tag{2.8}$$

The function "log" here denotes the common (base 10) logarithm.

2.2 Evolution from Excited States
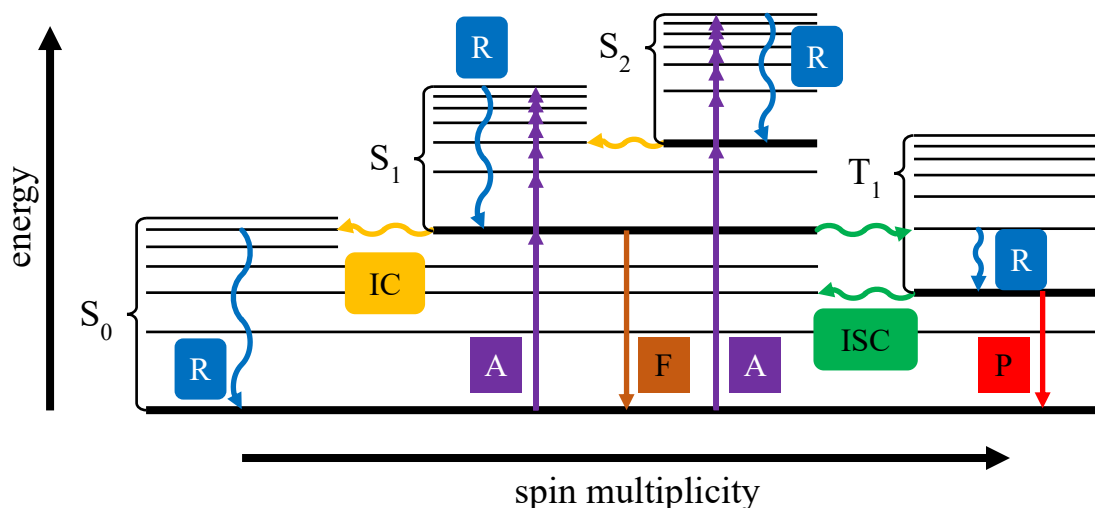
Figure 2.1: This Perrin-Jabłoński diagram summarizes several possible transitions pigments can undergo between states. Singlet electronic states are denoted S_n, and triplet states, T_n, where the subscript denotes the nth excited state of that spin multiplicity, $n = 0$ being the ground state. A thicker line represents the ground vibrational level of each electronic state, with higher vibrational levels aligned vertically above it. As is customary, radiative transitions—absorption (A), fluorescence (F) and phosphorescence—are depicted as straight arrows and nonradiative transitions—vibrational relaxation (R), internal conversion (IC) and intersystem crossing (ISC)— as wavy arrows. The overlapping absorption arrows indicate that given a photon of the appropriate wavelength, a pigment can be promoted to any vibrational level within the same multiplicity—not that these absorption events are sequential.

Whereas Section 2.1 explains how a pigment becomes excited as a result of interaction with light, this section discusses what happens to pigments excited by this or other means and how they might return to their ground states. Some of these processes are intramolecular, involving only the excited pigment. Among them are vibrational relaxation, internal conversion, and intersystem crossing, which are nonradiative, as well as fluorescence and phosphorescence, which are radiative, (i.e., emitting photons). Note that this list is by no means exhaustive. To illustrate a summary of these processes, Perrin-Jabłoński diagrams are useful, and one appears in Figure 2.1, depicting ground and excited electronic states along with vibrational levels for each one. S_n and T_n denote the nth singlet and triplet states, respectively. The fastest process after absorption ($\sim 10^{-15}$ s), is vibrational relaxation ($10^{-12} - 10^{-10}$ s), which occurs when an excited electron loses energy to vibrational modes, decaying to lower vibrational levels within a same electronic state. Internal conversion ($10^{-11} - 10^{-9}$ s) is a transition to a higher vibrational level of a lower electronic

state, which usually sets up the electron for further vibrational relaxation. Intersystem crossing (10^{-10} – 10^{-8} s) also typically precedes vibrational relaxation, but this transition is to a state with same energy and different spin multiplicity, such as $S_1 \rightarrow T_1$. The radiative transitions, fluorescence (10^{-10} – 10^{-7} s) and phosphorescence (10^6 – 10 s), are both photon emissions resulting in decay to lower electronic states, with the distinction that phosphorescence also involves a change in multiplicity (Lewis & Kasha, 1944). These two processes take place almost exclusively from the first excited state's ground vibrational level, for each multiplicity, regardless of wavelength of the initially absorbed light (Kasha, 1950). Note that spin-orbit coupling is what permits the otherwise-forbidden intersystem crossing and phosphorescence, whose change in multiplicity would normally violate spin angular momentum conservation. Section 2.2.1 discusses rates of radiative emission. Alternatively, excited pigments can lose their excess energy intermolecularly such as via EET or Dexter electron exchange, introduced in Section 2.2.2.

2.2.1 Radiative Emission

Excited (1) pigments can spontaneously emit photons of frequency ω and return to their ground state (0), a process whose rate is

$$W_{10}^S = A_{10} N_1, \tag{2.9}$$

where A_{10} is the Einstein A coefficient given by

$$A_{10} = \frac{\omega^3 |\boldsymbol{\mu}|^2}{3\pi\varepsilon_0 \hbar c^3}. \tag{2.10}$$

In Equations (2.9) – (2.10), N_1 is the number of pigments in the excited state, $\boldsymbol{\mu}$ is the electric dipole moment, ε_o is the vacuum permittivity, $\hbar$ is the reduced Planck constant, and c is the speed of light in a vacuum (Hilborn, 1982; van Amerongen et al., 2000). Because the pigments of interest reside in a protein environment with relative permittivity ε_r and refractive index $n = \sqrt{\varepsilon_r}$ the effective Einstein A coefficient can be expressed as a function of n:

$$A_{10}(n) = nf^2 A_{10}(1). \tag{2.11}$$

Here, $A_{10}(1)$ is the expression from Equation (2.10), and f is a correction factor given by

$$f = \frac{3\varepsilon_r}{2\varepsilon_r + 1} \tag{2.12}$$

to account for the small region which, occupied by the pigment, is not characterized by ε_r (van Amerongen et al., 2000). Returning to the ground state by this process alone may take PS I Chls nanoseconds; however, other pathways are available to these pigments, which are sufficiently tightly packed to exchange energy, as discussed next in Section 2.2.2.

2.2.2 Energy Transfer

The photons emitted by one pigment as described in Section 2.2.1—or, in fact, from any other source—may subsequently be absorbed by another pigment at a rate

$$W_{01}^i = B_{01}\rho(\omega)N_0. \tag{2.13}$$

In this case, $\rho(\omega)$ is the light field's energy density as a function of angular frequency, and the Einstein B coefficient B_{01} proportional to the stimulated absorption rate is used:

$$B_{01} = \frac{\pi|\boldsymbol{\mu}|^2}{3\varepsilon_0\hbar^2} = \frac{\pi^2 c^3}{\hbar\omega^3}A_{10}. \tag{2.14}$$
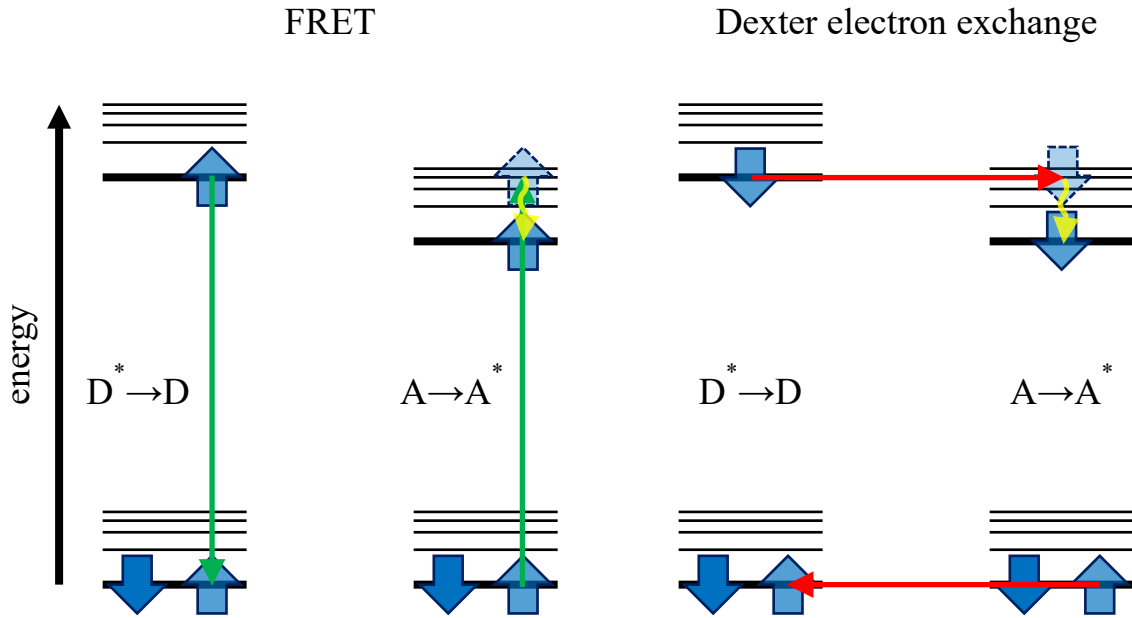
Figure 2.2 FRET (left) and Dexter electron exchange (right) mechanisms are depicted here. Violating the convention, wavy arrows here are reserved strictly for vibrational relaxation, despite all transitions here being nonradiative. Each wide, blue arrow indicates an electron's orbital and spin state. Higher vibrational levels to which transitions may occur are short-lived, as indicated by the lighter, dashed-bordered arrows in the acceptors' excited states. Swapping of spin multiplicities may occur as shown for Dexter electron exchange, though each electron's spin is conserved.

However, PS I antenna Chls commonly pass one another energy by nonradiative means such as FRET or Dexter electron exchange mechanism (Dexter, 1953), both portrayed in Figure 2.2. These types of energy transfer require two pigments: a donor (D) and an acceptor (A), whose excited states will be denoted by the superscript [*]. In the weak coupling limit—that is, when the donor's and acceptor's charge distributions coincide negligibly—FRET is the dominant of the two mechanisms and will therefore be briefly discussed next. For the strong coupling limit, see Section 2.3: Exciton Concept.

If the two pigments have interaction V_{DA}, the donor has fluorescence spectrum $F_D(\omega)$, and the acceptor has absorption spectrum $\varepsilon_A(\omega)$, the rate k_{FRET} of energy transfer $D^*A \rightarrow DA^*$ from the donor to the acceptor via FRET is given by (Förster, 1960; van Amerongen et al., 2000)

$$
\begin{aligned}
k_{\text{FRET}} &= 8\pi^3 \frac{V_{\text{DA}}^2}{\hbar^2} \frac{\int F_D(\omega)\varepsilon_A(\omega)\omega^{-4}\mathrm{d}\omega}{\int F_D(\omega)\omega^{-3}\mathrm{d}\omega \cdot \int \varepsilon_A(\omega)\omega^{-1}\mathrm{d}\omega} \\
&= \frac{9 \cdot 10^3 \ln(10)\,\kappa^2}{16\pi^3 n^4 N_A \tau_D^0 R^6} \int_0^\infty \frac{F_D(\omega)\varepsilon_A(\omega)}{\omega^4}\mathrm{d}\omega.
\end{aligned}
\tag{2.15}
$$

In the last expression, n is the environment's refractive index, N_A is Avogadro's number, τ_D^0 is the radiative lifetime of the donor in the absence of interactions, R is the distance between pigments, and κ^2 is the orientation factor defined by (Struve, 1995):

$$
\kappa^2 = \left(\hat{\boldsymbol{\mu}}_D \cdot \hat{\boldsymbol{\mu}}_A - 3\left(\hat{\boldsymbol{\mu}}_D \cdot \hat{\boldsymbol{R}}\right)\left(\hat{\boldsymbol{\mu}}_A \cdot \hat{\boldsymbol{R}}\right) \right)^2.
\tag{2.16}
$$

Note that the explicit form of κ appears in Equation (2.22), in calculating dipole-dipole interactions, the principal type of interaction between pigments of interest. In general, $0 \leq \kappa^2 \leq 4$, and for pigments randomly oriented, $\langle \kappa^2 \rangle = \frac{2}{3}$. The integral in Equation (2.15) indicates that there must be significant overlap of the donor's fluorescence with the acceptor's absorption for FRET to proceed. Furthermore, it is favorable for the donor's excited state energy to be higher than that of the acceptor, as the donor will have decayed to its lowest vibrational level before the energy transfer, whereas the acceptor may initially access any vibrational level of its excited state before itself undergoing vibrational relaxation. This agrees with the observation that only very few Chls in PS I absorb farther red than does P_{700}. The rate k_{FRET} can be expressed more compactly by defining two new variables τ_D and R_0:

$$
\tau_D \equiv \eta_D^0 \tau_D^0
\tag{2.17}
$$

$$R_0^6 \equiv \frac{9 \cdot 10^3 \ln(10)\, \kappa^2 \eta_D^0}{16\pi^3 n^4 N_A} \int_0^\infty \frac{F_D(\omega)\varepsilon_A(\omega)}{\omega^4}\, d\omega. \tag{2.18}$$

The physical meaning of τ_D is the lifetime of the donor in the presence of relevant interactions, proportional to the transfer-free quantum yield η_D^0 of the donor's fluorescence. R_0 is called the *Förster radius* and corresponds to the inter-pigment distance for which the donor is equally likely to undergo FRET with the acceptor as to fluoresce. The concise form of Equation (2.15) is

$$k_{\text{FRET}} = \frac{1}{\tau_D}\left(\frac{R_0}{R}\right)^6. \tag{2.19}$$

2.3 Exciton Concept

2.3.1 Electrostatic Origin of Photosynthetic Excitons

An exciton is an excitation delocalized over several pigments. The concept is useful in research on PS I, which comprises a large array of interacting pigments. These pigments interact chiefly electrostatically via their charge distributions $\rho_i(r)$, as can be expressed for any pair of pigments by

$$V_e = \frac{1}{4\pi\varepsilon} \iint \frac{\rho_1(r)\rho_2(r')}{|r - r'|}\, dr dr', \tag{2.20}$$

where ε is the dielectric constant in the medium—the protein environment, in this case. If the distance between pigments is significantly larger than their sizes, the interaction V_e can be usefully expanded in terms of their multipole moments: total charge, dipole moment, quadrupole tensor and any number of higher-order terms. As pigments are usually electrically neutral, dipole-dipole interactions dominate V_e: Charge-charge and charge-dipole interactions vanish, whereas higher-order terms are increasingly small. The dipole moment of pigment i centered at position r_i is

$$\boldsymbol{\mu}_i = \int \rho_i(r)(r - r_i)\, dr \tag{2.21}$$

and the dipole-dipole interaction between pigments i and j is

$$V_{dd} = \frac{1}{4\pi\varepsilon} \frac{\boldsymbol{\mu}_i \cdot \boldsymbol{\mu}_j - 3(\boldsymbol{\mu}_i \cdot \widehat{\boldsymbol{R}})(\boldsymbol{\mu}_j \cdot \widehat{\boldsymbol{R}})}{R^3} \cong V_{ij}, \tag{2.22}$$

where $\boldsymbol{R} \equiv r_j - r_i$ with corresponding unit vector $\widehat{\boldsymbol{R}}$ and magnitude R. Unfortunately for modeling, certain pairs of coupled pigments in the PS I RC are separated by no more than a few of their own lengths. The P_{700} Chls, for instance, sit 6 Å apart, which is only about four times the diameter of a

Chl's chlorin ring (Jordan et al., 2001; Millqvist-Fureby et al., 2014). The approximation $V_{dd} \cong V_{ij}$ from Equation (2.22) may be inaccurate in such cases (Damjanović et al., 2002).

2.3.2 General Case of *n* Excitonically Coupled Two-Level Pigments

Consider a system of *n* coupled pigments, each having only two states: ground and excited. Higher excited states of individual pigments are short-lived and will therefore be neglected here. The excitonic complex's Hamiltonian *H* can be written (Savikhin, Buck, & Struve, 1999)

$$H = \sum_{p=1}^{n} \hat{H}_p + \sum_{p=1,n-1} \sum_{q=p+1}^{n} V_{pq}, \tag{2.23}$$

where $\hat{H}_p$ is the electronic Hamiltonian for pigment *p*, and V_{pq} is the interaction energy between pigments *p* and *q*, possibly of the form of Equation (2.22). The summation indices are chosen specifically to prevent double counting of interactions between pairs of coupled pigments. The ground state of the system, in which no pigment is excited, can be expressed

$$\left| \chi_i^{(0)} \right\rangle = |\varphi_1 \cdots \varphi_i \cdots \varphi_n\rangle, \tag{2.24}$$

where φ_i is the ground-state wave function of the ith pigment. Similarly, there are *n* singly excited delocalized excitonic states $\psi_i^{(1)}$, which can be expanded in the basis of *n* localized states $\chi_i^{(1)}$ in which the excitation is localized on the ith pigment:

$$\left| \chi_i^{(1)} \right\rangle = |\varphi_1 \cdots \varphi_i^* \cdots \varphi_n\rangle, i = 1, \dots, n \tag{2.25}$$

where the superscript * denotes excitation of the ith pigment. Note that in Equations (2.24) and (2.25), the superscript in parentheses indicates the number of excitations. A sum of all *n* excited basis elements $|\chi_i^{(1)}\rangle$ with corresponding coefficients c_j^i can express an excited state $|\psi_i^{(1)}\rangle$ of the excitonic complex (Savikhin, Buck, & Struve, 1999):

$$\left| \psi_i^{(1)} \right\rangle = \sum_{j=1}^{n} c_j^i \left| \chi_j^{(1)} \right\rangle. \tag{2.26}$$

The delocalized excitonic stationary states of the complex described by the Hamiltonian in Equation (2.23) can be found by solving the Schrödinger equation:

$$H \left| \psi_k^{(1)} \right\rangle = E_k \left| \psi_k^{(1)} \right\rangle = \sum_{i=1}^{n} c_i^k \left| \chi_i^{(1)} \right\rangle. \tag{2.27}$$

Inserting the original Hamiltonian in matrix representation into Equation (2.27), one can find its elements. Diagonal elements H_i are the energies of the localized states, and off-diagonal elements V_{ij} are the interaction energies (Savikhin, Buck, & Struve, 1999):

$$H_{ii} = \left\langle \chi_i^{(1)} \middle| \hat{H} \middle| \chi_i^{(1)} \right\rangle \equiv H_i \tag{2.28}$$

$$H_{ij} = \left\langle \chi_i^{(1)} \middle| \hat{V}_{ij} \middle| \chi_i^{(1)} \right\rangle \equiv V_{ij} \tag{2.29}$$

This way, finding excitonic transitions is equivalent to diagonalizing the matrix $H = H_i + V_{ij}$. The n eigenvalues correspond to the energies E_i of excitonic levels, and their respective eigenvectors c_j^i represent expansion coefficients of the excited excitonic wave function $\psi_i^{(1)}$, (see Equation (2.26)). The squares of the coefficients, $|c_j^i|^2$, represent the yield of pigment j in the excitonic transition at energy E_i. That is, these coefficients characterize the delocalization of the excitation over the n pigments.

As stated in Section 2.3.1, the inter-pigment interactions giving rise to excitons are predominantly electrostatic, depending on the charge distribution of each pigment. If the transition dipole moments of individual pigments are $\boldsymbol{\mu}_j$, the singly excited excitonic transition dipoles $\boldsymbol{\eta}_i^{(1)}$ can be expressed as a superposition of these:

$$\boldsymbol{\eta}_i^{(1)} = \sum_{j=1}^{n} c_j^i \boldsymbol{\mu}_j, \tag{2.30}$$

where the oscillator strength, proportional to band intensity, is given by $|\boldsymbol{\eta}_i^{(1)}|^2$.

2.3.3   Excitonically Coupled Homodimer

As the simpler case of just two identical excitonically coupled pigments, each a two-state system, is instructive and can then be generalized to any number of pigments, it will be discussed in somewhat more detail here, following van Amerongen et al. (2000). Each pigment (numbered 1 or 2) individually has a Hamiltonian H_j and two states, ground φ^0 and excited φ^1, with respective energies ε^0 and ε^1, such that for pigment j ($j = 1, 2$),

$$H_j \varphi_j^i = \varepsilon^i \varphi_j^i. \tag{2.31}$$

Conveniently assigning the value $\varepsilon^0 = 0$ will simplify further calculations. When the two pigments interact, the system's total Hamiltonian becomes the sum of the individual Hamiltonians plus an interaction term V:

$$H = H_1 + H_2 + V. \tag{2.32}$$

The ground state of the system is now the product of the two individual ground states:

$$\psi^0 = \varphi_1^0 \varphi_2^0. \tag{2.33}$$

This makes the new ground state energy (van Amerongen et al., 2000)

$$E^0 = \langle \varphi_1^0 \varphi_2^0 | (H_1 + H_2 + V) | \varphi_1^0 \varphi_2^0 \rangle = \langle \varphi_1^0 \varphi_2^0 | V | \varphi_1^0 \varphi_2^0 \rangle = V_{00}. \tag{2.34}$$

V_{00} is thus the shift in the coupled system's ground state energy, equal to E^0 itself as ε^0 was set to 0. The excited states are linear combinations

$$\psi^f = c_1^f \varphi_1^1 \varphi_2^0 + c_2^f \varphi_1^0 \varphi_2^1 \tag{2.35}$$

where coefficients $c_1{}^f$ and $c_2{}^f$ are orthonormal. These must be solutions to the Schrödinger equation

$$(H_1 + H_2 + V)\psi^f = E^f \psi^f, \tag{2.36}$$

which leads to the following system of equations upon taking the inner product with by $\varphi_1{}^1\varphi_2{}^0$ or $\varphi_1{}^0\varphi_2{}^1$:

$$c_1^f (\varepsilon^1 + \langle \varphi_1^1 \varphi_2^0 | V | \varphi_1^1 \varphi_2^0 \rangle) + c_2^f \langle \varphi_1^1 \varphi_2^0 | V | \varphi_1^0 \varphi_2^1 \rangle = c_1^f E^f \tag{2.37}$$

$$c_1^f \langle \varphi_1^0 \varphi_2^1 | V | \varphi_1^1 \varphi_2^0 \rangle + c_2^f (\varepsilon^1 + \langle \varphi_1^0 \varphi_2^1 | V | \varphi_1^0 \varphi_2^1 \rangle) = c_2^f E^f. \tag{2.38}$$

Four of the terms here can conveniently be abbreviated according to the following definitions:

$$V_{11} \equiv \langle \varphi_1^1 \varphi_2^0 | V | \varphi_1^1 \varphi_2^0 \rangle (= V_{22} \equiv \langle \varphi_1^0 \varphi_2^1 | V | \varphi_1^0 \varphi_2^1 \rangle) \tag{2.39}$$

$$V_{12} \equiv \langle \varphi_1^1 \varphi_2^0 | V | \varphi_1^0 \varphi_2^1 \rangle (= V_{21} \equiv \langle \varphi_1^0 \varphi_2^1 | V | \varphi_1^1 \varphi_2^0 \rangle). \tag{2.40}$$

The two eigenenergies E^1 and E^2 are then found to be

$$E^1 = \varepsilon^1 + V_{11} + V_{12} \tag{2.41}$$

$$E^2 = \varepsilon^1 + V_{11} - V_{12} \tag{2.42}$$

and the corresponding eigenstates (ψ^f from Equation (2.35)),

$$\psi^1 = \frac{1}{\sqrt{2}} \varphi_1^1 \varphi_2^0 + \frac{1}{\sqrt{2}} \varphi_1^0 \varphi_2^1 \tag{2.43}$$

$$\psi^2 = \frac{1}{\sqrt{2}} \varphi_1^1 \varphi_2^0 - \frac{1}{\sqrt{2}} \varphi_1^0 \varphi_2^1. \tag{2.44}$$

Displacement energy denotes the mean difference $\mathbb{D} = V_{11} - V_{00}$ between the excited-state energy of the coupled system and that of a single pigment. The difference $E^1 - E^2 = 2\,V_{12}$ between the two excited eigenenergies in Equations (2.41) – (2.42) is called *exciton splitting*.

Despite Chls in PS I being nearly all chemically identical, each lives in its own local environment, influencing its set of energy levels. The first step in generalizing the model above is to account for the minor differences in excited-state energies between two excitonically coupled pigments. If the difference between the two pigments' transition energies is δ, and 0 is now set as the mean of the excited-state energies, two excited-state *site energies* $\pm\delta/2$ can be defined, one for each pigment. Analogous to Equations (2.37) – (2.38), the new system to solve is

$$c_1^f\left(\delta/2 - E^f\right) + c_2^f V_{12} = 0 \tag{2.45}$$

$$c_1^f V_{12} + c_2^f\left(-\delta/2 - E^f\right) = 0 \tag{2.46}$$

satisfied by the new energies E^1 and E^2

$$E^1 = \sqrt{V_{12}^2 + \delta^2/4} \tag{2.47}$$

$$E^2 = -\sqrt{V_{12}^2 + \delta^2/4} \tag{2.48}$$

Defining the shorthand $\Delta \equiv \dfrac{\delta}{2V_{12}}$, the four coefficients are

$$c_1^1 = \frac{1}{\sqrt{1 + \left(-\Delta + \sqrt{1 + \Delta^2}\right)^2}} \tag{2.49}$$

$$c_2^1 = c_1^2\left(-\Delta + \sqrt{1 + \Delta^2}\right) \tag{2.50}$$

$$c_1^2 = \frac{1}{\sqrt{1 + \left(-\Delta - \sqrt{1 + \Delta^2}\right)^2}} \tag{2.51}$$

$$c_2^2 = c_1^2\left(-\Delta - \sqrt{1 + \Delta^2}\right) \tag{2.52}$$

The next step in generalizing this model is to account for the rest of the arbitrarily many (n) interacting pigments a system such as PS I may comprise. The n singly excited excitonic states, each a linear combination of states in which one pigment is excited, is

$$\psi^f = \sum_{p=1}^{n} c_p^f \varphi_p^f \prod_{p \neq q} \varphi_q^0. \tag{2.53}$$

Finding these and their eigenenergies is the standard problem of diagonalizing the Hamiltonian H_{ij}. At this point, the general case considered in Section 2.3.2 is recovered.

2.4   Electron Transfer (ET)
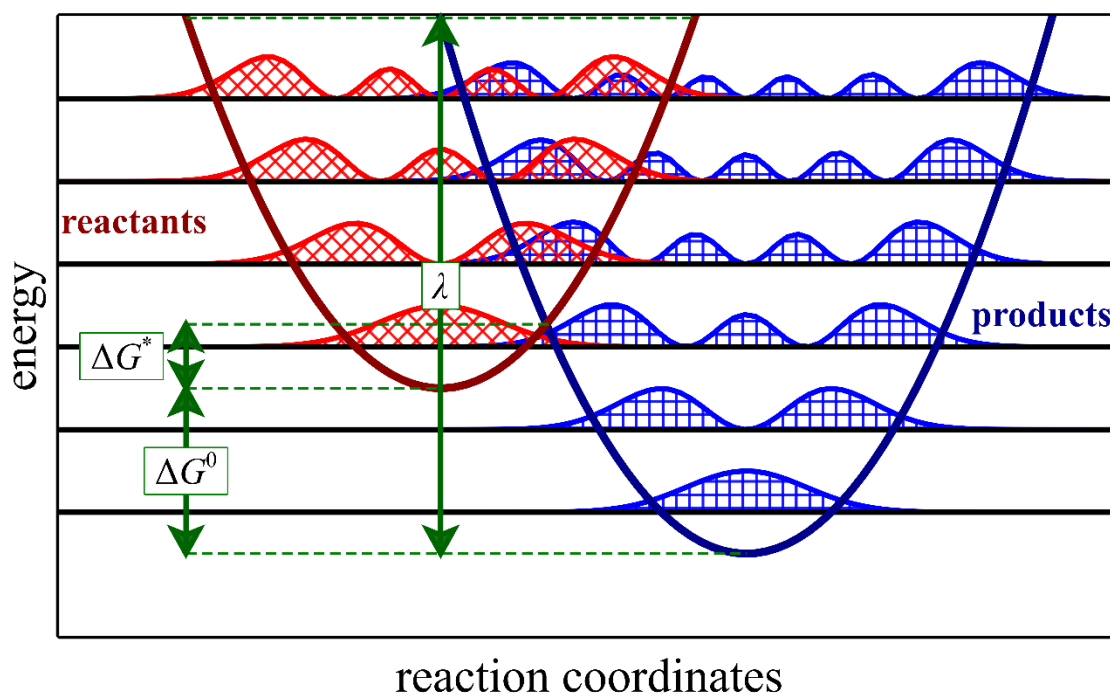
Figure 2.3: ET concepts are illustrated here. The two parabolas represent Gibbs free energy profiles for the reactants (dark red) and products (dark blue) in reaction coordinates, approximated as harmonic oscillator potentials (Warshel & Parson, 2001). Horizontal lines coincide with the lowest several energy levels. Superimposed on each of these is the corresponding probability density, not properly normalized but scaled for visual clarity. Quantities from Equation (2.57) are indicated.

The concept of donors and acceptors used to describe EET in Section 2.2.2 also applies to ET, where instead of excitation energy traveling to ever-redder pigments, electrons are transferred to cofactors of increasing redox potentials (Hopfield, 1974). The additional concepts of reactants (R) and products (P), corresponding to the pigments before (D A) and after (D$^+$ A$^-$) the ET reaction, respectively, also become useful. R and P can each be modeled with quadratic Gibbs free energies as functions of reaction coordinates (analogous to harmonic oscillator potentials) with the corresponding, equally spaced energy levels. By the Franck-Condon principle, electronic transitions occur on a much shorter timescale than nuclear motion and thus involve no change in

42

nuclear configuration (Marcus, 1956). Each energy level of R is aligned with a higher level of P, whose ground state energy is ΔG^0 below that of R, making ΔG^0 the Gibbs free energy change of the reaction (see Figure 2.3). Fermi's golden rule can be applied again, this time, to approximate the ET rate to first order (Moser & Dutton, 1992; Moser, Keske, et al., 1992):

$$k_{\text{ET}} = \frac{2\pi}{\hbar} V_R^2 FCWD, \tag{2.54}$$

where $V_R{}^2$ is the quantum mechanical matrix element which couples the electronic wave functions of R and P, and *FCWD* is the Franck-Condon weighted density of states, which indicates the overlap of the nuclear wave functions of R and P. These are given by (Moser & Dutton, 1992; Moser, Keske, et al., 1992; Sutin, 1991)

$$V_R^2 = V_0^2 e^{-\beta R} \tag{2.55}$$

$$FCWD = \frac{e^{-(\Delta G^0 - \lambda)^2 / 4\lambda k_B T}}{\sqrt{4\pi \lambda k_B T}}. \tag{2.56}$$

In Equation (2.55), R denotes the shortest distance between centers of a donor's atom and an acceptor's atom, the parameter β quantifies the electronic coupling's decay within the medium surrounding the redox centers, and $V_0{}^2$ is the strongest-possible electronic coupling in the limit as R goes to zero. In Equation (2.56), k_B is the Boltzmann constant, T is the absolute temperature, and λ is the reorganization energy—the energy it would take to distort the P state's equilibrium configuration to that of the R state with ET suppressed. The activation energy ΔG^*—the energy barrier that must be overcome for the reaction to occur—relates λ to ΔG^0 in the following way (Bolton & Archer, 1991; Marcus & Sutin, 1985; Sutin, 1991):

$$\Delta G^* = \frac{(\lambda + \Delta G^0)^2}{4\lambda}. \tag{2.57}$$

Figure 2.3 illustrates these quantities in context with R and P energies. For ET within proteins, as is of interest in this work, a semiempirical approximation for Equation (2.54) has been concocted (Moser & Dutton, 2006; Moser & Dutton, 1992; Moser, Keske, et al., 1992; Moser, Page, & Dutton, 2006):

$$\log k_{\text{ET}} = 13 - \frac{\beta}{2.303}(R - 3.6) - \gamma \frac{(\Delta G^0 + \lambda)^2}{\lambda}. \tag{2.58}$$

Note that for this common equation to give the ET rate in hertz, distances must be expressed in ångströms and energies in electron volts. The coefficient $^\beta/_{2.303}$, in the term showing exponential

43

dependence of k_{ET} on R, was found to be ~0.6 for protein environments such as PS I. In the case of interest for this work, R specifically denotes the shortest distance between π-orbitals of the donor and acceptor Chls. Classically, the coefficient γ should be equal to $(4\ k_B\ T \ln 10)^{-1} = 4.23$ [eV], though accounting for quantum mechanical tunneling, which increases k_{ET}, yields $\gamma = 3.1$ [eV]. λ here is estimated at 0.7 [eV] (Moser, Page, & Dutton, 2006). Equation (2.58) then becomes

$$\log k_{ET}^{ex} = 13 - 0.6(R - 3.6) - 3.1\frac{(\Delta G^0 + \lambda)^2}{\lambda}. \tag{2.59}$$

The coefficients were determined based on data from experiments in which exergonic ET was observed (i.e., ET was energetically favorable, or $\Delta G^0 < 0$); therefore, this equation applies exclusively to exergonic ET rates, as indicated by the superscript "ex". Because the endergonic ($\Delta G^0 > 0$) ET rate is virtually impossible to measure, given the process's much lower probability, Crofts and Rose (2007) turned to the second law of thermodynamics to obtain it. This law predicts a Boltzmann distribution for the ratio K of R to P, or in other words,

$$K = \frac{[D^+A^-]}{[DA]} = e^{-\frac{\Delta G^0}{k_B T}} = \frac{k_{ET}^{ex}}{k_{ET}^{end}}, \tag{2.60}$$

where superscript "end" indicates the endergonic rate (Page et al., 1999). Solving for $\log(k_{ET}^{end})$ gives

$$\log k_{ET}^{end} = 13 - 0.6(R - 3.6) - 3.1\frac{(\Delta G^0 + \lambda)^2}{\lambda} - \frac{\Delta G^0}{0.06}. \tag{2.61}$$

In both Equation (2.62) and Equation (2.64), note that the energy barrier vanishes for $-\Delta G^0 = \lambda$, corresponding to the P parabola crossing the R parabola's minimum in Figure 2.3.

2.5   Pump-Probe Transient Absorption Difference Spectroscopy

Experiments on EET and ET dynamics are conducted, in part, using pump-probe absorption difference spectroscopy (Figure 2.4), which works by the following principle. A short laser pulse, the pump pulse, is focused into a small volume of a sample, exciting a portion of the molecules and thus altering their absorption spectrum. A second, probe pulse, is passed through the same spot in the sample at different time delays, and its intensity is recorded using a photodetector. To minimize the impact of random pulse-to-pulse light intensity fluctuations in the probe beam, a reference beam is split off from it prior to the sample using a beam splitter, and the reference pulses pass through a different spot in the sample not overlapping with the excitation

area. The probe beam intensity is normalized to the reference beam intensity to obtain absorption changes associated with sample excitation. In addition, the pump and probe intensities are recorded intermittently with the pump pulse on and off, further enhancing the signal-to-noise performance of the setup. The measured signal, ΔA, is the difference in the sample's absorbance A in the presence of a pump pulse versus in its absence, or in other words (Berera et al., 2009),

$$\Delta A = A_{\text{on}} - A_{\text{off}}, \tag{2.62}$$

where the subscripts $_{\text{on}}$ and $_{\text{off}}$ refer to whether a pump pulse immediately preceded the probe pulse or not, respectively.
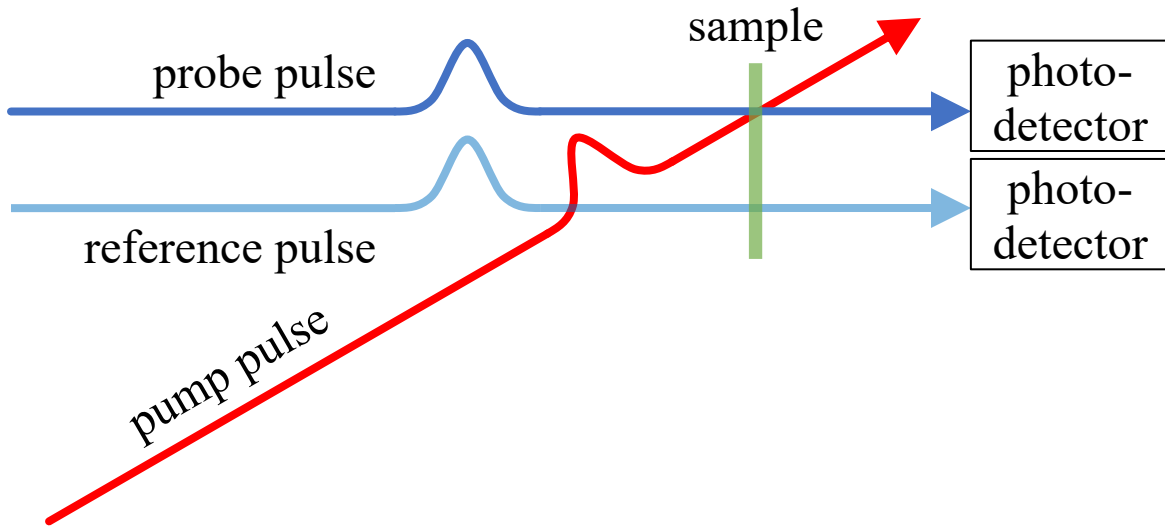
Figure 2.4: In this basic pump-probe spectroscopy scheme, the sample (green) is excited by a pump pulse (red) shortly before being probed (dark blue). A reference pulse (light blue), previously split off from the beam providing probe pulses (not shown), passes through a different portion of the sample to reduce noise from intensity fluctuations in the probe light.

Because the measured quantities are the probe and reference beam intensities, here denoted respectively as p and r, from which A and ΔA can then be calculated using Equation (2.8), Equation (2.62) can be expressed in terms of these as

$$\Delta A = -\frac{1}{\ln 10}\left(\ln\left(\frac{p_{\text{on}}}{r_{\text{on}}}\right) - \ln\left(\frac{p_{\text{off}}}{r_{\text{off}}}\right)\right) = \log\left(\frac{p_{\text{off}}r_{\text{on}}}{p_{\text{on}}r_{\text{off}}}\right). \tag{2.63}$$

The wavelengths of the pump and probe beams can be varied, as can the time delay of the latter relative to the former, to obtain a time-resolved ΔA spectrum over a range of both parameters, revealing processes such as described in Sections 2.2 and 2.4. The absorption changes associated with sample excitation arise from three major superimposed effects: photobleaching (PB),

stimulated emission (SE) and excited state absorption (ESA) (Berera et al., 2009). Each corresponds to a change in a pigment's absorption of light and is described in one of the next three sections, their respective measured signals illustrated in Figure 2.8. In these sections, each pigment will be assumed, for simplicity, to have only two levels: ground (0) and excited (1).

2.5.1 Photobleaching (PB)

PB, the first and fastest (< 100 fs) process observed, occurs when, as a result of the pump pulse, a portion of the pigments in the sample leave the ground state. Clearly, the excited pigments can no longer undergo transitions from the ground state and, therefore, cannot absorb photons corresponding to such transitions (see Figure 2.5). The sample will absorb fewer of the subsequent probe pulse photons at such frequencies, resulting in a negative PB signal ΔA_{PB}. Because each pigment has only a finite probability $P_{0 \to 1}$ of absorbing a pump photon promoting it to the excited state, only a corresponding fraction of ground-state pigments will become excited. The PB signal is then

$$\Delta A_{\mathrm{PB}} = A_0 P_{0 \to 1} - A P_{0 \to 1} = (A_0 - A) P_{0 \to 1}, \tag{2.64}$$

where A is the sample's total absorbance, and A_0 is the collective absorbance of all pigments which remain in the ground state when the pump pulse is applied. It is clear from the Beer-Lambert law (Equation(2.8)) that A is proportional to the total number N of pigments, the same reasoning applying to A_0 and the number N_0 of pigments remaining in the ground state. Defining N_1 as the number of pigments excited by the pump pulse and A_1 as the collective absorbance in the ground state of N_1 pigments, one can also write

$$N_0 + N_1 = N \tag{2.65}$$
$$A_0 + A_1 = A \tag{2.66}$$

which, combined with Equation (2.64), gives

$$\Delta A_{\mathrm{PB}} = -A_1 P_{0 \to 1} \tag{2.67}$$

confirming that ΔA_{PB} must, indeed, be negative. However, note that its spectral shape will otherwise match that of the sample's ground-state absorption spectrum. In the case of a multichromophore complex with weak interaction, ΔA_{PB} is entirely due to the pigment(s) currently excited. As the excitation energy is transferred from pigment to pigment, the ΔA_{PB} spectrum will

dynamically change in the case where D and A molecules have different absorption spectra. In the case of an excitonic complex, the whole excitonic spectrum is bleached as it is considered as one "supermolecule" with one common ground state and a number of excitonic excited states. The dynamics of ΔA changes due to energy transfer between excitonic levels will then stem from ESA and SE components that depend on properties of a particular excitonic state.
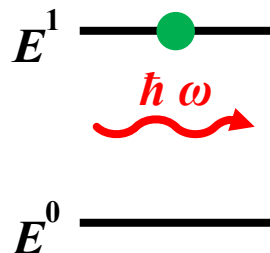
Figure 2.5: Photobleaching: The pump pulse having promoted a fraction of the sample's pigments from the ground state, the excited pigments (such as that represented as a green disk) cannot absorb probe photons (wavy red arrow) corresponding to the now-impossible transitions from the ground state. More probe light passes straight through the sample to be detected, resulting in a negative ΔA signal.

2.5.2 Stimulated Emission (SE)

A pigment's decay from the excited state and the corresponding photon emission can be induced by an identical incoming photon—a principle exploited in lasers—as shown in Figure 2.6. The incident probe photon and the pigment's emitted photon are then both detected after the sample, ensuring $p_{on} > p_{off}$ in Equation (2.63), resulting in a negative signal. ΔA_{SE} must be proportional to the number of excited pigments as well as the probability $P_{1 \to 0}$ of transition back to the ground state on exposure to the pump pulse, so that

$$\Delta A_{SE} = -A_1 P_{1 \to 0}. \tag{2.68}$$

In a true two-state system, where the probabilities $P_{0 \to 1}$ and $P_{1 \to 0}$ are equal, signals ΔA_{PB} and ΔA_{SE} are also equally large; however, the ΔA_{SE} signal will be Stokes (red-) shifted relative to ΔA_{PB}, as vibrational relaxation occurs. In the case of a weakly coupled system, the SE spectral dynamic shape will reflect energy transfer processes as an excitation hops between spectrally different pigments. In the case of strongly coupled systems, SE will also change reflecting energy transfer among different energy levels.
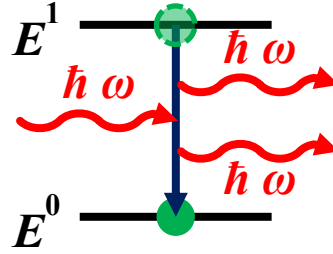
Figure 2.6: Stimulated emission: An excited pigment encounters a probe photon of energy E^1 - E^0, prompting it to decay back its ground state while emitting an identical photon in the same direction. The original probe photon and its new identical twin are both detected, resulting in a negative ΔA signal.

2.5.3 Excited-State Absorption (ESA)

A pigment excited by a pump photon can become further excited by absorbing a second, probe photon, in the process of ESA. In the case of a weakly coupled system of pigments, ESA is usually a very broad band that primarily raises the background of the total ΔA signal with minimal effect on the fine features of ΔA. To account for ESA, one should include higher excited states (like those involved in Soret bands of Chls). Denoting the ground state S_0, the first excited state S_1 and a higher excited state S_2, ESA will be due to transitions $S_1{\rightarrow}S_2$, while SE is due to $S_1{\rightarrow}S_0$, and PB is due to missing transitions $S_0{\rightarrow}S_1$. Note that transitions $S_0{\rightarrow}S_2$ can also occur, but spectrally, they are far off the $S_0{\rightarrow}S_1$ absorption and do not overlap with the signal typically measured in pump-probe experiments, whereas $S_1{\rightarrow}S_2$ transitions do.

In the case of an excitonic system, ESA is considered in the context of an entire excitonic complex which is already in one of its singly excited excitonic states, as discussed in Section 2.3.2, and can be promoted to its *doubly* excited state. This doubly excited state arises when the complex absorbs *two photons*, and it occurs even in the approximation of two-level pigments.

Following the form of the singly excited excitonic state basis for an n-pigment complex (Equation (2.25)), a doubly excited state basis is needed to discuss ESA and can be written as follows (Savikhin, Buck, & Struve, 1999):

$$\left|\chi_{ij}^{(2)}\right\rangle = \left|\varphi_1 \cdots \varphi_i^* \cdots \varphi_j^* \cdots \varphi_n\right\rangle, i = 1, \ldots, n-1; j = i+1, \ldots, n. \qquad (2.69)$$

The enumeration of indices ensures that each of the $\frac{n(n-1)}{2}$ combinations of two excited pigments is listed exactly once. The doubly excited state can be reached only from a singly excited state in

which one of the two pigments is already excited, meaning that transitions can occur only from a singly excited state $|\chi_i^{(1)}\rangle$ to doubly excited state $|\chi_{ij}^{(2)}\rangle$. For a second incident photon with electric field $\boldsymbol{E}$, the transition dipole moment $\boldsymbol{\mu}_{i\to ij}^{(1\to 2)}$ can be found in the following way (Savikhin, Buck, & Struve, 1999):

$$\boldsymbol{\mu}_{i\to ij}^{(1\to 2)} = \langle\varphi_1\cdots\varphi_i^*\cdots\varphi_j^*\cdots\varphi_n|\widehat{\boldsymbol{E}}|\varphi_1\cdots\varphi_i^*\cdots\varphi_j\cdots\varphi_n\rangle \tag{2.70}$$

$$\boldsymbol{\mu}_{i\to ij}^{(1\to 2)} = \mu_i\langle\varphi_1\varphi_1\rangle\cdots\langle\varphi_i^*\varphi_i^*\rangle\cdots\langle\varphi_j^*|\widehat{\boldsymbol{E}}|\varphi_j\rangle \tag{2.71}$$

$$\boldsymbol{\mu}_{i\to ij}^{(1\to 2)} = \boldsymbol{\mu}_j \tag{2.72}$$

The transition dipole moment from the singly excited state to the doubly excited one is thus equal to the additionally excited pigment's dipole moment. The Hamiltonian describing the doubly excited excitonic states is

$$\langle\chi_{ij}^{(2)}|\widehat{H}|\chi_{ij}^{(2)}\rangle = H_i + H_j \tag{2.73}$$

$$\langle\chi_{ij}^{(2)}|\widehat{H}|\chi_{ik}^{(2)}\rangle = \langle\chi_{ji}^{(2)}|\widehat{H}|\chi_{ki}^{(2)}\rangle = V_{jk}; j \neq k \tag{2.74}$$

Equation (2.73) defines the diagonal elements, and Equation (2.74), all non-zero off-diagonal elements. Note from the repeated index i in the latter case that the only significant interactions are between doubly excited states in which one of the two excited pigments is the same for both states. Furthermore, these interactions are equal to those between the other two pigments. This new, doubly excited Hamiltonian can therefore be expressed entirely in terms of elements of the singly excited Hamiltonian (Equations (2.28) – (2.29)), and likewise, its eigenvalues $E_i^{(2)}$ and a set of corresponding eigenvectors d_{ij}^k can be found by diagonalization, (upper index k indicating the coefficient for the kth term of the eigenvector for the case in which pigments i and j are excited). These eigenvectors are linear combinations in the basis $\chi_{ij}^{(2)}$ defined in Equation (2.69). Using index ℓ to list singly excited states, one can express the transition dipole moment $\boldsymbol{\eta}_{\ell\to k}^{(2)}$ between these and doubly excited states in the following way:

$$\boldsymbol{\eta}_{\ell\to k}^{(2)} = \sum_{i<j,m} d_{ij}^k c_m^\ell(\boldsymbol{\mu}_j\delta_{im} + \boldsymbol{\mu}_i\delta_{jm}) = \sum_i f_{\ell k i}\boldsymbol{\mu}_i, \tag{2.75}$$

using the definition

$$f_{\ell k i} \equiv \sum_m d_{mi}^k c_m^\ell. \tag{2.76}$$

Extending the analogy to the singly excited state case, the oscillator strengths for the doubly excited states are given by $|\boldsymbol{\eta}_{\ell\to k}^{(2)}|^2$.
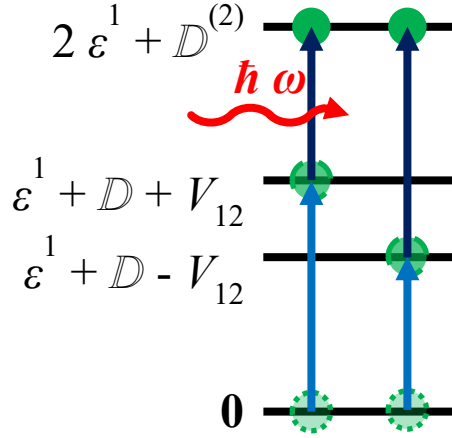
Figure 2.7 Excited-state absorption: In this schematic representation, each green disk represents an excitonic homodimer rather than a single pigment. A pump photon has promoted a complex to one of two possible singly excited exciton states, this transitions represented by a light blue arrow. A probe photon can now excite the complex further (dark blue arrow), to a doubly excited exciton state. This probe photon is absorbed, resulting in a positive ΔA signal.

ESA can be considered in the simplified context of an excitonically coupled homodimer like that explored in Section 2.3.3, conserving the same notation. Then, the doubly excited state $\psi_{12}^{(2)}$ and corresponding energy $E_{12}^{(2)}$ are given by (van Amerongen et al., 2000)

$$\psi_{12}^{(2)} = \varphi_1^1 \varphi_2^1 \tag{2.77}$$

$$E_{12}^{(2)} = \langle \varphi_1^1 \varphi_2^1 | (H_1 + H_2 + V) | \varphi_1^1 \varphi_2^1 \rangle = 2\varepsilon^1 + \langle \varphi_1^1 \varphi_2^1 | V | \varphi_1^1 \varphi_2^1 \rangle \tag{2.78}$$

If the displacement energy $\mathbb{D}^{(2)}$ for the doubly excited state is simply twice that for the singly excited state ($\mathbb{D}^{(2)} = 2\,\mathbb{D}$), and the ground state energy $E^0 = V_{00}$ is again set to zero, the two singly excited state energies are $\varepsilon^1 + \mathbb{D} \pm V_{12}$, as shown in Section 2.3.3, and the doubly excited state energy is

$$E^{(2)} = 2\varepsilon^1 + \mathbb{D}^{(2)}, \tag{2.79}$$

equal to the sum of the two singly excited states' energies. The two associated ESA transitions then have energies $\varepsilon^1 + \mathbb{D} \mp V_{12}$ (van Amerongen et al., 2000). Figure 2.7 schematizes ESA for an excitonically coupled dimer.

Because PB, SE and ESA can all occur concurrently in an experiment, the total measured signal can be expressed

$$\Delta A = \Delta A_{\mathrm{PB}} + \Delta A_{\mathrm{SE}} + \Delta A_{\mathrm{ESA}} \qquad (2.80)$$

Figure 2.8 shows a possible ΔA spectrum and its three components as just discussed.
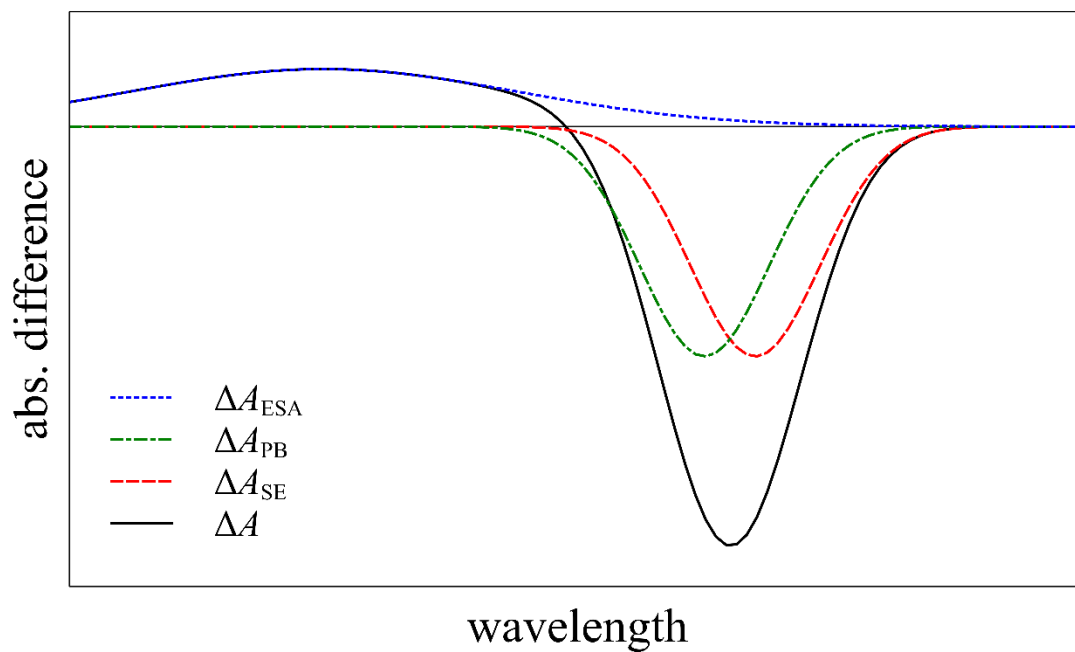
Figure 2.8: This fictitious measured ΔA signal (solid black) is decomposed into its PB (dash-dotted green), SE (dashed red) and ESA (dotted blue) components.

CHAPTER 3.   APPARATUS

3.1   Introduction

This chapter describes the methods used in the experiments of CHAPTER 4. First, the basic principle of the common technique of pump-probe transient absorption difference spectroscopy is introduced, followed by a description of our home-built apparatus for this purpose. This first section will conclude with a description of and manual for our home-built "shaker," versatile device used for keeping objects such as sample cuvettes in uninterrupted motion for various ends such as preventing excessive consecutive excitations of a given volume of a sample. The second section lays out the method used for obtaining steady-state (P_{700}^+ - P_{700}) spectra via a modification to a commercial spectrophotometer.

3.2   Femtosecond Absorption Spectrometer
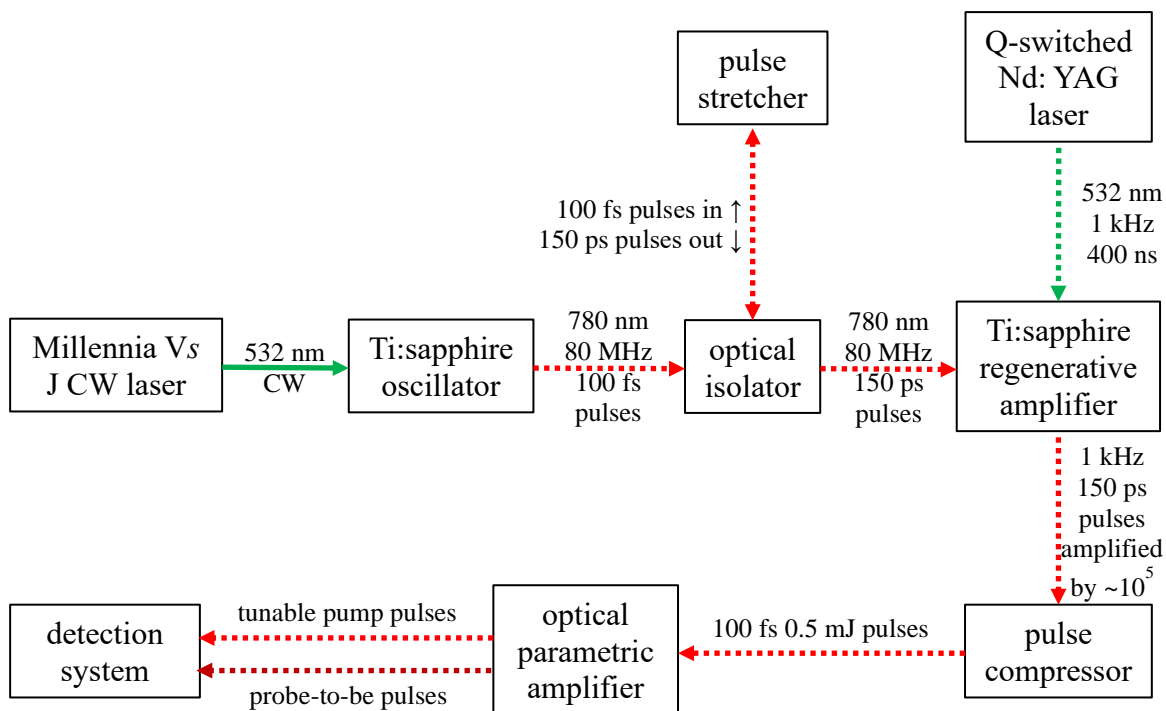
Figure 3.1: simplified block diagram of the femtosecond laser system used in transient absorption spectroscopy

The kilohertz femtosecond absorption spectrometer, or simply fs pump-probe spectrometer, consists of the following principal components: a Ti:sapphire oscillator, an optical isolator, a pulse stretcher, a Ti:sapphire regenerative amplifier, a pulse compressor, an optical parametric amplifier (OPA) and a pump-probe detection system, as shown in Figure 3.1.

The home-built Ti:sapphire oscillator, pumped by a Spectra-Physics Millennia V*s* J laser emitting 3.5 W continuous wave (CW) at wavelength 532 nm, produces ~60 fs pulses of wavelength ~780 nm at a repetition rate of ~80 MHz. A minor portion of its output is directed onto a detector and used as the basis for timing of the regenerative amplifier. The optical isolator directs pulses from the oscillator to the stretcher, where a system of diffraction gratings reversibly stretches them to ~150 ps duration by introducing group velocity dispersion (GVD), reducing pulse peak power by ~3 orders of magnitude to avoid damage to optical components downstream once this pulse gets amplified by ~5 – 6 orders of magnitude. Stretched pulses return to the isolator along the original path having acquired a $^\pi/_2$ polarization rotation from a round trip through a Faraday rotator, and the isolator now directs them toward the regenerative amplifier, blocking the return path to the oscillator. The regenerative amplifier amplifies every 80 000th pulse by a factor of ~10^5. It is essentially another Ti:sapphire laser, pumped by a Clark-MXR ORC-1000 Nd:YAG laser outputting 400 ns duration, 532 nm pulses at 1 kHz repetition rate. A weak, stretched seed-pulse from the oscillator is first captured into the amplifier's laser cavity using a fast electro-optical polarization rotator and kept inside the cavity for ~20 passes resulting in a ~10^5-fold increase in its energy; then the same rotator is used to direct the amplified pulse out of the cavity. Note that only one out of 80 000 pulses is amplified, bringing the amplified pulse repetition rate to 1 kHz to match the pump pulse repetition rate of the amplifier's pump laser. Amplified pulses proceed to the compressor, where gratings compress them back to ~100 fs. The OPA, modeled on the layout by Hasson (1997), is used to transform fixed-wavelength amplified pulses into tunable pulses within the range of the visible optical spectrum. A nonlinear optical β-BaB$_2$O$_4$ (BBO) crystal within the OPA splits the incoming 780 nm photons into two photons of different frequencies, signal and idler, summing to that of the original photon by conservation of energy. Sending the signal frequency pulses through a frequency doubler results in pulses that can be tuned continuously in the 600 – 720 nm range by tilting the BBO crystal. The detection system receives these wavelength-tuned pulses from the OPA as well as a portion of the fundamental, 780 nm beam. The former is tuned to the desired wavelength and used as pump pulses for experiments

such as described in CHAPTER 4. A mechanical chopper blocks every other pump pulse, resulting in a 500 Hz repetition rate. The fundamental pulses are delayed relative to the pump pulses by a computer-controlled mechanical delay line at the entrance of the detection system. They are then focused into a sapphire plate to create broadband continuum pulses, subsequently split along parallel paths and used as probe and reference pulses. An off-axis parabolic mirror focuses pump, probe and reference beams into the sample, after which the probe and reference are directed into an Oriel MS257 imaging monochromator used to select probe wavelengths. At the monochromator's output, a pair of Hamamatsu S3071 Si PIN photodiodes measure the probe and reference pulse energies. These signals are digitized and sent to a computer for processing. Spectra-Solve software (Ames Photonics, Ames, IA) is used to run data collection as well as manipulate and fit spectra.

3.2.1 Modifications to fs Pump-Probe Spectrometer for "Open - Closed" Experiments
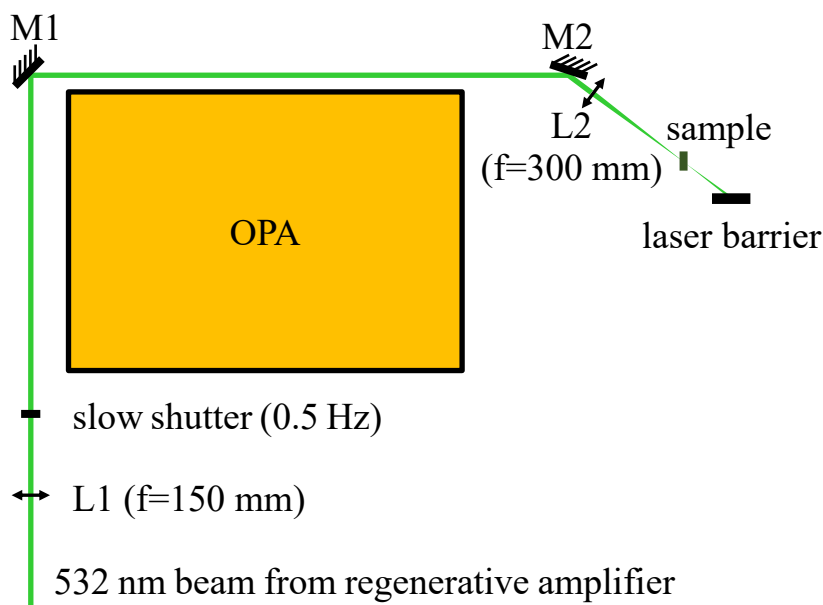
Figure 3.2: The path of the 50 mW 532 nm CW beam recovered from the regenerative amplifier circumvents the OPA on its way to the sample, directed by flat mirrors M1 and M2. Lens L1 collimates the beam, and L2 focuses it to a ~1 mm diameter in the sample, shortly beyond which a laser barrier blocks it. The slow shutter, operated at 0.5 Hz in this work, intermittently blocks the beam so that two sets of data can be collected in parallel, with and without illuminating the sample.

Experiments described in Section 4.7 require intermittent illumination of PS I samples to close their RCs. For that, we use the ~400 ns long pulses from the regenerative amplifier pump laser which, after pumping the Ti:sapphire crystal, escape the cavity through a dichroic end mirror. These pulses precede our pump and probe pulses, have a sufficient energy of ~50 μJ, and thus can be used to "pre-excite" the sample, initiating electron transfer and promoting all PS I complexes to a closed state where the special pair is oxidized, forming P_{700}^+ and thus can no longer initiate charge transfer.

The 532 nm pulses are directed to the sample and focused inside it to a spot of diameter ~1 mm using the simple configuration of flat mirrors and lenses diagrammed in Figure 3.2. Lens L1 (f=150 mm) collimates the beam from the regenerative amplifier, flat mirrors M1 and M2 direct it into the sample, and L2 focuses it to the area where the pump and probe beams coincide. A home-built electromagnetic shutter is inserted between L1 and M1, permitting alternating measurements of ΔA in the sample illuminated or not by the green light when the shutter is open or closed, respectively. The data collection script in Spectra-Solve is modified such that the shutter alternates between open and closed states after each data point recorded. For kinetic curve collection, a data point corresponding to the first probe pulse delay is written into a blank spectrum after 1 s accumulation time with the shutter open. The shutter then closes, and another point at the same delay is measured in similar fashion and written into the next spectrum. The delay line advances to its next position, and the cycle repeats until two curves are completely recorded, each corresponding to one state of the shutter (i.e., corresponding to closed and open RCs). A similar principle applies to wavelength scans at constant probe delay times. Alternating between the open and closed states between consecutive points rather than entire curves of either type is important as it guards against fluctuations that may occur on the timescale of recording each curve.

3.3   Shaker

One challenge laser spectroscopy is avoiding exciting the same volume of sample too many consecutive times. In the experiments described in CHAPTER 4, it is important to let PS I complexes return to their ground state before exciting them anew. This is achieved in part by keeping the pump pulse energies low—thereby minimizing the probability of exciting a single complex multiple times with a single pulse—and in part by keeping the sample in uninterrupted motion, so that each pump-probe shot surveys a partially fresh volume of the sample. Devices such

as spinning cells have traditionally been used for this purpose (Savikhin, Xu, Martinsson, et al., 2001), but these were found to introduce extra noise in experiments with low repetition rate pulses and are generally harder to align and use. To simplify alignment and decrease noise, I have built an alternative device, christened "shaker," shown in Figure 3.3.
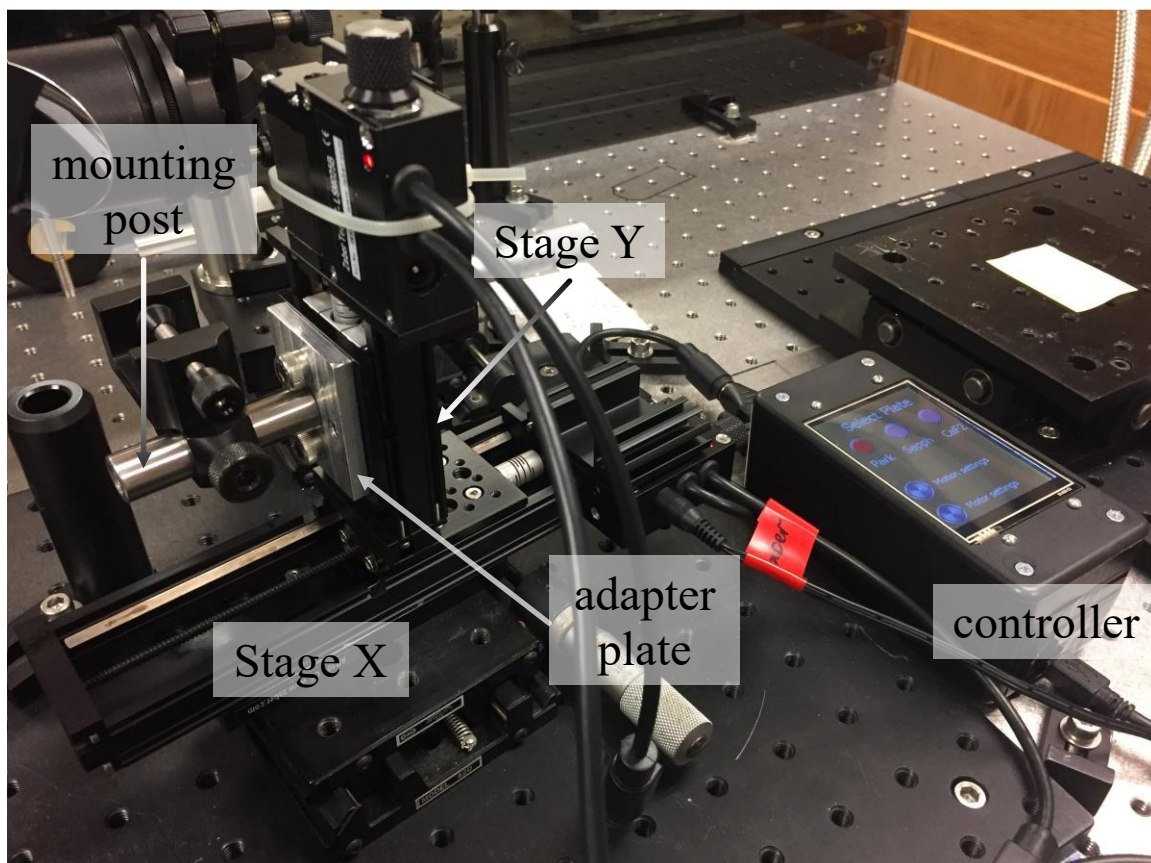
Figure 3.3: shaker in its natural habitat

3.3.1 Benefits

Convenience

The shaker presents several advantages over the common spinning cell alternative. It can hold a variety of sample cells including the typical rectangular cuvettes best suited for use in a UV-visible spectrophotometer, which is otherwise subject to dubious adjustments to reconcile it with the spinning cell's awkward geometry. More permanent modifications to the spectrophotometer would be inconvenient as it is not used primarily with spinning cells. The ability to use a standard cuvette in experiments that require a moving sample is therefore significant, and

more so because many experiments require frequent switching between steady-state and ultrafast spectroscopy. Spinning cells also require assembly and disassembly as well as cleaning of their multiple components with each new sample, costing precious time in studies such as presented in CHAPTER 4, which demand consecutive measurements of ten different samples in a the fs pump-probe spectrometer (see Section 3.2).

A spinning cell may precess, causing the sample to sweep a range of planes only one of which contains the crossing point of the pump and probe beams. No such issue exists for a cuvette in the shaker, whose oscillatory plane is defined by the two stages' translation. At worst, the cuvette may not be aligned with this plane, but this is comparatively easy to correct.

Versatility

The shaker can hold not just sample cells but virtually any small optical element requiring continuous motion. It was originally designed to hold a calcium fluoride (CaF_2) plate for white light continuum generation, in place of the sapphire plate of the kHz detection system (see Section 3.2). CaF_2 makes for a white light spectrum extending farther into the UV range, which is useful for certain experiments, but is much more prone to damage than sapphire from the high intensity focused pulses needed for broadband continuum generation. Atoms in the CaF_2 crystal may become shifted by a lattice position, leaving a defect—a hole, which looks as an opaque spot, absorbs light increasingly and gets further burned out. CaF_2 may still be used if it remains in uninterrupted motion so that each spot in the crystal receives only a limited amount of energy that can be dissipated once this spot has exited the beam path. Thus, lattice defects do not form, and the CaF_2 plate can be used indefinitely. Many transparent media can be used in place of sapphire or CaF_2 (Brodeur & Chin, 1999; Penzkofer et al., 1993; Yang & Shen, 1984), some of them birefringent, but the shaker circumvents this issue by keeping all motion exclusively translational. This way, the laser beam's polarization remains at a constant angle to any preferred axis in the crystal. Lastly, its 100 mm horizontal travel range allows the user to mount two different objects to the shaker and alternate easily between inserting one or the other—or neither—into the beam path.

3.3.2 Manual

Components & Assembly

The shaker's essential components are two perpendicularly coupled, motorized translation stages (Figure 3.3). The horizontal and vertical stages, henceforth given the respective names Stage X and Stage Y, are Zaber models T-LSM100B and T-LSM025B, with travel ranges of 100 mm and 25 mm, respectively. Stage Y's PREVIOUS cable inserted into Stage X's NEXT cable. Automation parameters are set using a touchscreen controller with a DE-9 serial port and USB Mini-b receptacle. The controller communicates with the stages via a T-DC06 data cable with DIN connectors and a DIN serial adapter. This is connected to Stage X's PREVIOUS cable. Two power supplies are required: 15 V for the stages and 5 V for the controller, powered via its USB port. Onto Stage Y is bolted a homemade aluminum adapter plate in the center of which are three ¼"-20 threaded holes aligned horizontally, ½" apart, where posts can be attached horizontally. The post may support any further attachments such as sample holders. One heat sink is strapped to each stage's stepping motor by a zip tie.

Octagonal Motion

The shaker is programmed to describe octagons of varying radius. This motion pattern was selected as it is among the simplest to ensure uninterrupted motion, as whenever one translation stage is at rest, the other must be moving. Figure 3.4 illustrates the motion pattern (left) and the cycle of conditional commands producing it (right). Four horizontal and four vertical coordinates—x_1, x_2, x_3, x_4, and y_1, y_2, y_3, y_4, numbered from left to right and top to bottom, respectively—are defined. The controller is continually surveying the position of each stage. At the top of the path, Stage X is traveling rightward toward x_4 when it passes x_3. The controller is informed of this and sends Stage Y, currently waiting at position y_1, a command to move down to y_4. As it does so, Stage X reaches its x_4 destination and waits. Stage Y passes y_3, triggering the command to return Stage X to x_1, and the pattern continues thus, completing the cycle repeatedly until the program is interrupted. Note that the controller is specifically programmed to send each stage commands as a function of the other's position. This is key to preventing even momentary complete stops as each stage must resume motion before the other arrives at its destination, as defined in the program. Note, also, that each command instructs a stage to proceed to a set position

rather than travel a set distance. The latter option is bound to result in a gradual positional drift if the steps of the stages' stepping motors are not counted perfectly for each trip back and forth. Figure 3.5 shows an actual pattern traced out by the shaker and makes it clear that for smaller radii of motion, the ideal octagon shape evolves into a square with decreasingly rounded corners. This is because the stages take time to accelerate between rest and cruising speed. In experiments, oscillation radii are typically kept sufficiently large, slightly less than the size of the 10 mm-wide cuvettes. Evidently, "shaker" is a misnomer for this device, which lacks the abrupt, jerky motion associated with shaking, but "oscillator" already—and more appropriately—designates a key portion of the fs pump-probe spectrometer (Section 3.2).
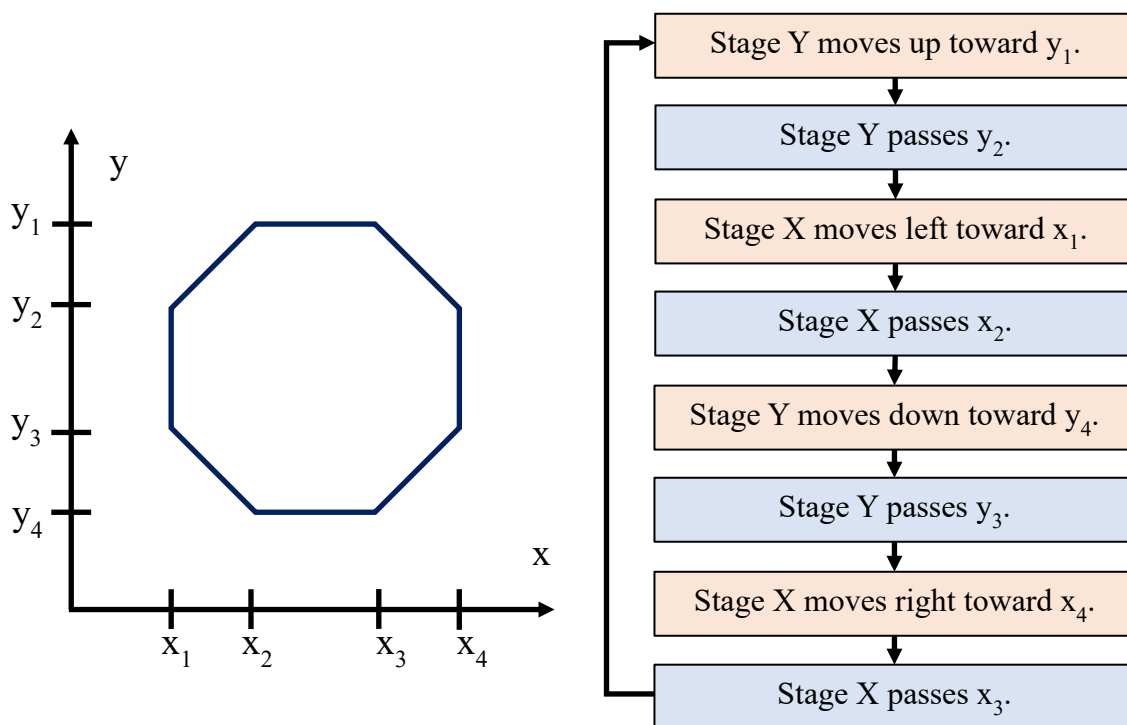
Figure 3.4: Motion pattern of shaker (left) and controller commands producing this octagonal path (right). The controller continually monitors the shaker's position and, after sending each command (pink boxes), waits for the following condition (blue boxes) to be met before sending the next command. Stage X receives commands to begin and end its motion while stage Y is moving and vice versa, so that at least one stage is in motion at any given time.

The shaker controller is built around a 4" touch screen minicomputer, (4D Systems microLCD PICASO Intelligent Display). The controller's program is permanently loaded into its memory and provides touch-screen menus to control details of motion pattern and speed. The menu presents a selection of three predetermined patterns with their own motion parameters for different

applications. While all patterns are concentric octagons, users can choose the overall size of the octagons and motion speed as well as define continuously changing pattern sizes to prolong the time between shots hitting the same spot. More technical details on the shaker appear in an extension to this user manual—see *Controls* and *Care & Maintenance* in APPENDIX A.

Figure 3.5: This real motion pattern was traced out on a notecard by the shaker with a marker attached. Settings were as follows: D1 = 1 mm, D2 = 13 mm, dD = 10 = 2 mm, Cruise speed = 16 mm/s, Acceleration = 200 mm/s^2, and Current = 100%. This path differs from the ideal octagons dictated by the controller program because the stages take time to accelerate between rest and cruising speeds, a problem accentuated as the radius of motion becomes small, when octagons devolve into decreasingly rounded squares. In experiments, the shaker was set to describe large enough shapes to avoid momentary complete stops.

3.4   Modifications to UV-Vis Spectrophotometer for Steady-State "Open - Closed" Experiments

The pump-probe dynamics of the PS I complex with an open RC are a superposition of signals arising from the electronic energy transfer within the excited antenna toward the RC, and subsequent CS and ET along cofactors of the RC. As these processes occur concurrently within the same time window, isolating signals due to ET from those due to energy transfer is ambiguous. However, it has been shown (Savikhin, Xu, Chitnis, & Struve, 2000; Savikhin, Xu, Martinsson, Chitnis, & Struve, 2001; White, et al., 1996) that both open and closed RCs act as excitation traps, and energy transfer kinetics within the PS I antenna are not significantly affected by the state of the RC. In the case of a closed RC, however, ET is completely blocked, and the absorption difference kinetics signal is due entirely to energy transfer processes, while in the case of an open RC, the signal is a superposition of both energy transfer and ET signals. This allows isolation of the ET signal by subtracting signals measured in complexes with closed RCs from ones measured

with open RCs—that is, (open‑closed) absorption differences—providing the most direct information on the ET kinetics decoupled from energy transfer.

The PS I RC can be promoted into its closed state using illumination of the sample for several seconds (Savikhin, Xu, Chitnis, & Struve, 2000; Savikhin, Xu, Martinsson, et al., 2001). A long-living P_{700}^+ radical arises due to a finite probability that the electron on the terminal electron acceptor, instead of recombining with the special pair, can be scavenged from the terminal acceptor, creating a long-living P_{700}^+ state. Under prolonged illumination, complexes are excited multiple times, eventually promoting most of the complexes into a "closed" state. An external electron donor such as sodium L-ascorbate dissolved in solution with PS I can be used to slowly reduce P_{700}^+, returning the sample to its pre-illumination state. This permits many consecutive measurements of the same PS I sample with alternating open and closed RCs, details of which are described next.

Steady-state spectra presented in this work (see Section 4.3) were all measured using a Varian Cary 300 Bio UV-Vis Spectrophotometer, henceforth known simply as the spectrophotometer. Experiments such as described in Section 4.4 require intermittent illumination of samples inside the spectrophotometer's chamber, motivating the following modifications inspired by Savikhin, Xu, Chitnis, and Struve (2000). To this end, a 20 mW blue LED is mounted on a post, immediately over a sample cell, as shown in Figure 3.6. The data collection program is modified such that the LED can be switched on and off at specific delays with respect to each data point measurement. The control program starts by waiting for time τ_{dark} defined by the user, giving the sample time to relax from any state induced by ambient or stray light to which it may have been exposed prior to the spectrophotometer's chamber being closed. The absorbance is measured at the first wavelength and recorded into a first spectrum, after which the LED is switched on for time τ_{LED} and off for time τ_{cool} before the second absorbance measurement, written into a second spectrum. These absorbance measurements are averages over a period τ_{avg} starting after the τ_{cool} delay. τ_{dark}, τ_{LED}, τ_{cool} and τ_{avg} can all be defined in the program and are usually on the order of a minute for the first and a few seconds for the latter three. Once absorption is measured at one wavelength, the spectrophotometer moves to the next wavelength, and the cycle repeats until two spectra are completely recorded, corresponding to absorbance of the unilluminated and illuminated sample, or, in the case of PS I, to the spectra of PS I with closed (P_{700}^+) and with open RC (P_{700}). Concurrently, the former is subtracted from the latter, producing a difference spectrum,

(P_{700}^+ - P_{700}), stored in memory. The same setup can also be used in kinetic mode, when the absorbance is recorded every 0.5 s and plotted with respect to time. In this case, the LED is turned on and off manually as desired, using a switch. In either case, further spectral processing can be performed using Spectra-Solve, as with the fs pump-probe spectrometer (see Section 3.2).
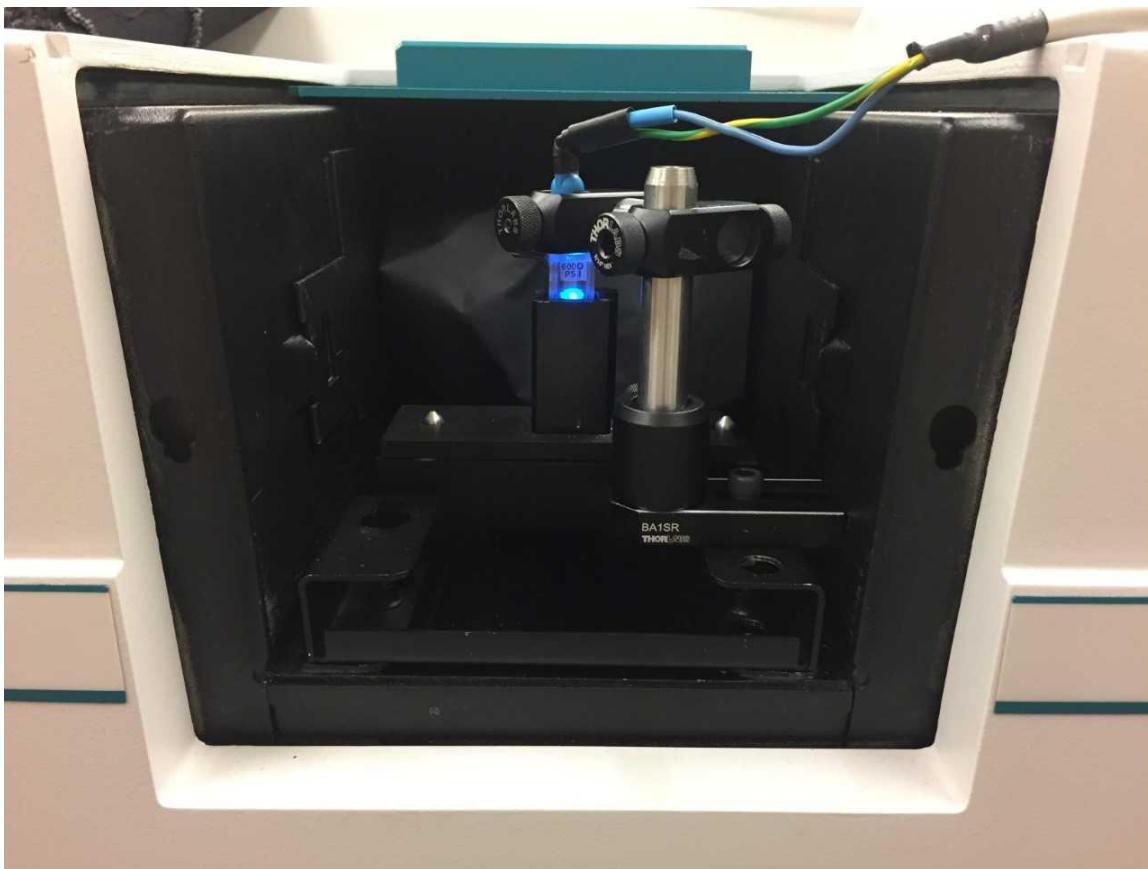
Figure 3.6: This open-chamber view of the spectrophotometer shows the modification permitting (P_{700}^+ - P_{700}) spectrum measurements. A 20 mW blue LED mounted immediately above the sample can illuminate it intermittently, causing temporary oxidation of P_{700} dimers.

CHAPTER 4.   SPECTROSCOPY ON MUTANT *SYNECHOCYSTIS* SP. PCC 6803 PS I WITH PERTURBATIONS NEAR A_{-1} AND A_0

4.1   Introduction

This chapter describes a comparative study of three families of three PS I mutants from freshwater cyanobacterium *Synechocystis* sp. PCC 6803 (*S.* sp. PCC 6803). Each family comprised two single mutants, each with an equivalent mutation targeting the RC's A- or B-branch, as well as the corresponding double mutant. To date, such double mutant studies have been rare in the literature despite their potential value for observing whether and how ET proceeds along a necessarily affected RC branch. The mutations targeted the axial ligands to A_{-1} and A_0 as well as a peripheral H-bond to A_0. The goal was to investigate the role of A_{-1} in CS and the effects of the disrupted bonds on CS and in determining properties of the targeted cofactors. In the first mutant series, A_{-1}'s axial ligand, a water molecule which also forms an H-bond with nearby asparagine (Asn, N) amino acid residue PsaB-N582 or PsaA-N600, is lost when Asn is replaced with methionine (Met, M). In the second set of mutants, it is A_0's axial ligand, PsaA-M684 or PsaB-M659, which was studied via replacement with histidine (His, H). The new His residue may not only raise the unusually low redox potential of A_0 but also form an H-bond with A_1 of the same branch, possibly influencing ET from A_0^- to A_1, as observed in other studies (McConnell et al., 2015; Ramesh et al., 2007; Sun et al., 2014). The third mutant family was also characterized by an alteration of the A_0 environment, this time, by replacing tyrosine (Tyr, Y) residue PsaA-Y692 or PsaB-Y667, which forms a peripheral H-bond with A_0, with phenylalanine (Phe, F), which forms no such bond. The idea was to learn whether and to what extent the H-bond contributes to A_0's spectral properties or to the ET step toward A_1. The focus of this chapter is the A_{-1} mutant family, as accessory Chls have less often been the targets of mutations, as evidenced by the current scarcity of literature concerning these cofactors. A single recent A_{-1} mutant study by Badshah et al. (2018) currently serves as the best comparison and complement to that presented in this chapter. By contrast, many studies have already been published on PS I mutants with the four aforementioned residues altered near A_0 (Byrdin, Santabarbara, et al., 2006; Cohen et al., 2004; Dashdorj, Xu, Cohen, et al., 2005; Fairclough et al., 2003; Giera et al., 2009; Li, et al., 2006; Müller, Slavov, et al., 2010; Ramesh et al., 2004, 2007; Rappaport et al., 2006).

First and most importantly, the results of the A_{-1} mutant experiments suggest that A_{-1} is the true first electron acceptor, a conclusion also consistent with the A_0 Met→His mutant results. The deduced effects of these two sets of axial ligand mutations are to raise the redox potential of the targeted A_{-1} or lower that of the targeted A_0. In both cases, much of the ET was redirected along the intact branch in single mutants. Double mutant studies confirmed that ET along an affected branch to the terminal acceptors was mostly precluded, as electrons recombined with P_{700}^+. A_0 peripheral H-bond mutations (Tyr→Phe) did not result in similar detriment to ET, nor did they discernibly affect the absorption spectrum of A_0. Steady-state absorption of all ten samples points to a slight Chl deficiency in the antennas of most mutants, a conclusion most notably reinforced by ultrafast dynamics of the Tyr→Phe mutants.

Generation of all *S*. sp. PCC 6803 mutants described in more detail below, as well as isolation of WT and mutant PS I trimers, were performed by Lujun Luo and Prof. Wu Xu of the Department of Chemistry at the University of Louisiana at Lafayette. All major experiments were performed at room temperature on PS I trimers purified from these ten strains, suspended in 3-(N-morpholino)propanesulfonic acid (MOPS) buffer. All samples were strained for 1 min through 0.2 μm centrifugal filters to remove potential impurities prior to ultrafast experiments.

4.2   Descriptions of Mutants

4.2.1   PsaB-N582M & PsaA-N600M

Between the A_{-1} Chl and its nearby Asn amino acid residue (PsaB-N582 or PsaA-N600 for the A- or B-branch, respectively), which is hydrophilic, lies a water molecule axially ligated to the Chl's Mg^{2+} ion as well as H-bonded to the oxygen atom of the Asn residue (Rappaport et al., 2006), with all four bond lengths in the ~2 – 3 Å range. When Asn is replaced with nonpolar, hydrophobic Met, the water axial ligand is lost, as shown in Figure 4.1. This perturbation provides a means to investigate the role of A_{-1} in primary CS and the impact of the amino acid environment on the properties of A_{-1}. Single mutants in which Asn was replaced with glutamine (Gln, Q), His or leucine (Leu, L) were also generated, but as the Asn→Met single mutants produced the smallest signals in (P_{700}^+ - P_{700}) spectroscopy (see Section 4.4), only these and their corresponding double mutant were used for further experiments. (P_{700}^+ - P_{700}) spectra for all A_{-1} mutants appear in APPENDIX B.
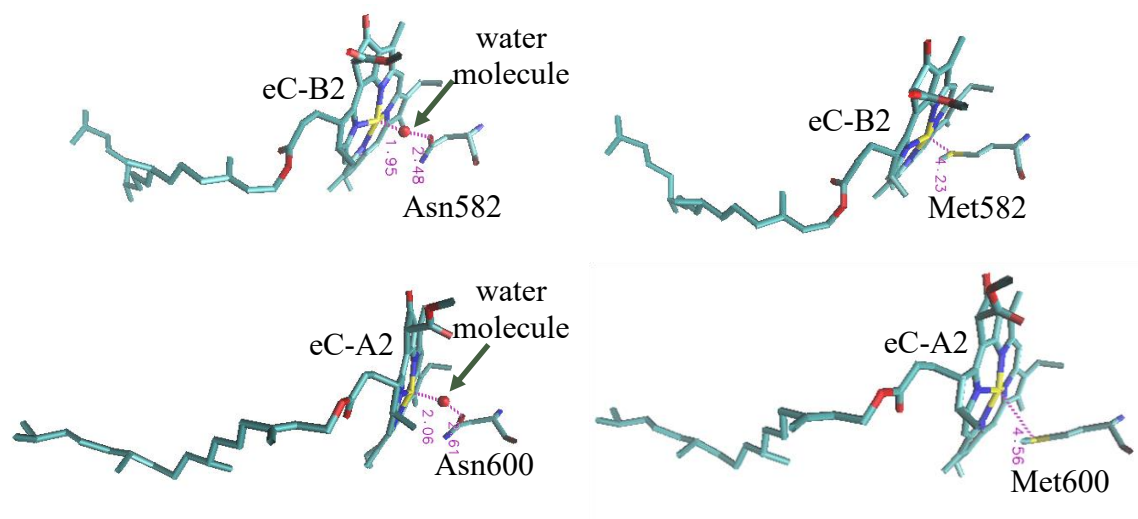
Figure 4.1: PsaB-N582M (top) and PsaA-N600M (bottom) mutations were modeled by Lujun Luo using the programs VMD and Modeler, based on 1JB0 structure (Jordan et al., 2001). WT appears on the left and mutants on the right. Only the A_{-1} Chls, Asn or Met residue, and intermediate water molecule (red sphere) are shown. Distances between key components of the structures are indicated in violet, in ångströms.

4.2.2   PsaA-M684H & PsaB-M659H

The A_0 Chl has the sulfur atom of Met residue PsaA-M684 or PsaB-M659 as its axial ligand (Cohen et al., 2004; Dashdorj, Xu, Cohen, et al., 2005). According to Sun et al. (2014), this Chl's bond with sulfur is thought to be much weaker than the bonds with nitrogen or oxygen, more common in PS I and II, yet it appears ubiquitous across species. It was suggested that this contributes to the A_0's low redox potential, a necessity for this electron acceptor. The authors state that in the same position, a different residue would likely raise the A_0 redox potential, thereby hindering ET along the altered branch. Molecular dynamics simulations from the same study have shown that a His residue, which lacks sulfur, would still coordinate A_0 and, being hydrophilic, may additionally form an H-bond with A_1 as shown in Figure 4.2. Some of the work presented in this chapter therefore used PsaA-M684H, PsaB-M659H, and the corresponding double mutant PS I. Comparing the effects of these mutations targeting A_0 to those of mutations targeting A_{-1} via a set of analogous experiments can shed light on the structural motifs that shape the necessary primary electron donor properties and the mechanism of primary CS. These first two mutant families will subsequently be collectively called the axial ligand mutants.
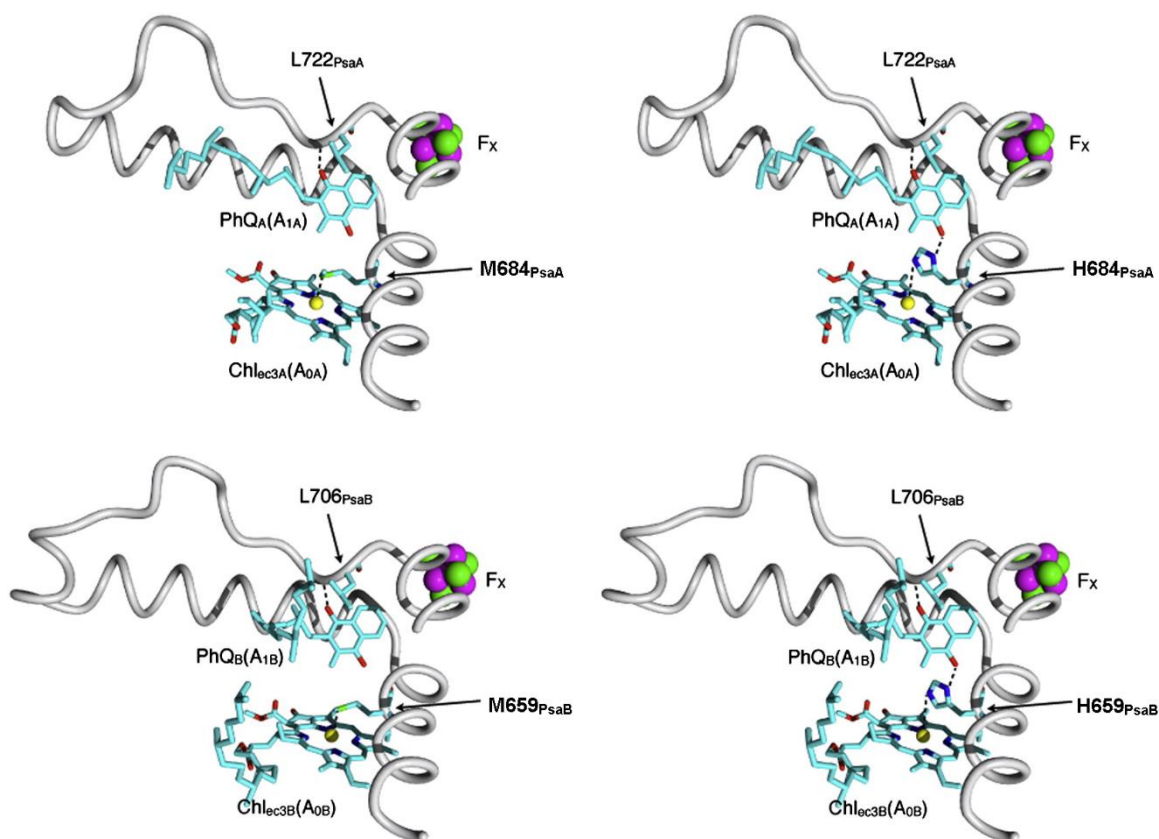
Figure 4.2: PsaA-M684H (top) and PsaB-M659H (bottom) mutations are depicted as by Sun et al. (2014), showing only a minimum of PS I secondary structure, A_1, and F_X. WT is on the left and mutants on the right. Dotted lines represent possible H-bonds. Oxygen appears red, Mg^{2+} is yellow, sulfur is green, nitrogen is blue, and iron is violet. Note that the WT's Met residue can form only one bond, with the A_0 Chl's Mg^{2+}, whereas the mutant's His residue has a possible additional bond with an oxygen atom of A_1.

4.2.3 PsaA-Y692F & PsaB-Y667F

An H-bond exists between the ring V keto oxygen of the A_0 Chl and the hydroxyl oxygen of Tyr residue PsaA-Y692 or PsaB-Y667 (Figure 4.3). To study the role of this peripheral H-bond in ET, mutants were generated by replacing Tyr with Phe. This amino acid is identical to Tyr save that it lacks the hydroxyl group, rendering it hydrophobic and thus unable to form H-bonds. PS I mutants PsaA-Y692F, PsaB-Y667F, and the corresponding double mutant were studied, with special emphasis on the possible alterations of the A_0 absorption spectrum.
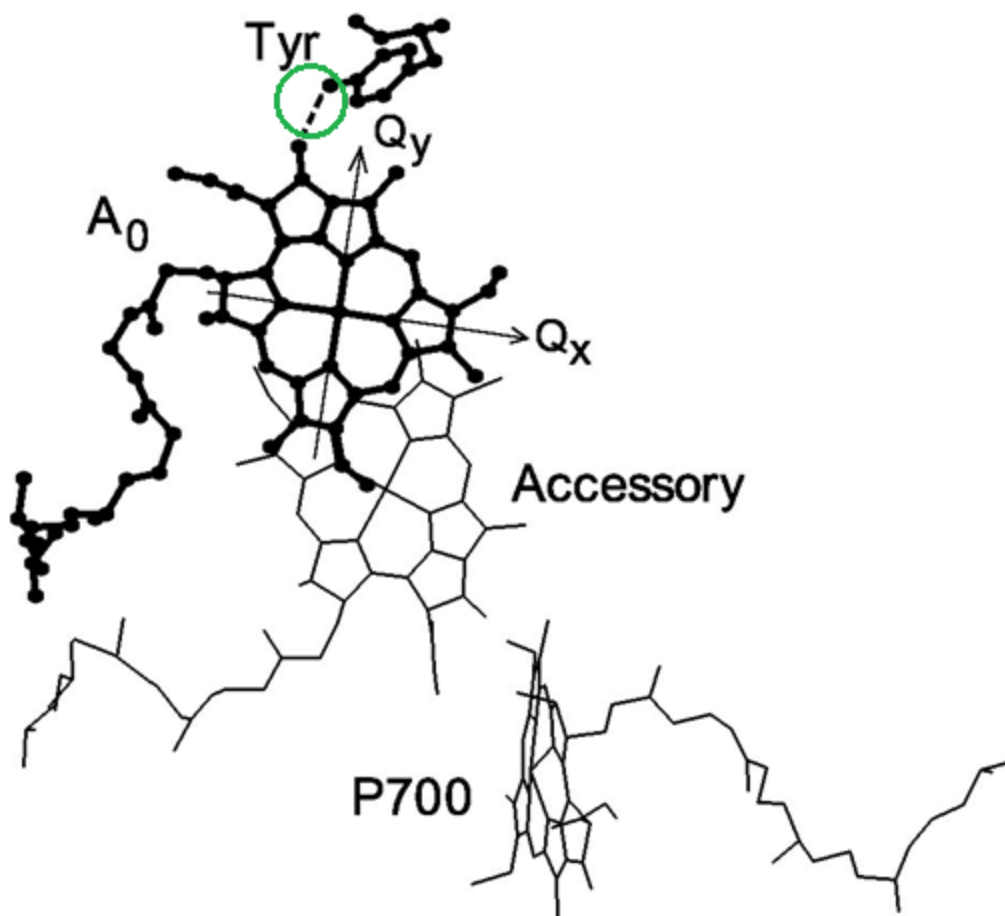
Figure 4.3: Chls of the B-branch of the PS I RC are shown with the Tyr residue that forms an H-bond (dotted line circled in green) with A_0 (Xu et al., unpublished). Bold lines emphasize the A_0 Chl and Tyr structures. Tyr's hydroxyl group and the H-bond it forms with A_0's ring V keto oxygen, circled in green, are missing from the Tyr→Phe mutants.

4.3   Steady-State Absorption Spectroscopy

4.3.1   Method

Steady-state absorption spectra of WT and all mutant PS I trimers were measured using the spectrophotometer specified in Section 3.4. Such spectra were recorded for all sample preparations before and after each experiment reported in the subsequent sections of this chapter to ensure that no degradation had occurred during said experiment. In each case, absorbance was measured over the 300 – 900 nm range in 1 nm steps. The spectra presented in this section are those of the samples used in the experiments of Section 4.6, in which all ten samples were measured consecutively in the fs pump-probe spectrometer (Section 3.2). The pre- and post-experiment steady-state spectra

of each sample, which were virtually identical, were averaged. A constant background was then subtracted, as the solution and cuvette without PS I were featureless in the visible range (see Figure 4.4), and all spectra were normalized to maximum absorbance in the Q_y region (640 – 720 nm). Actual Q_y absorbance maxima were all in the range of 0.68 ± 0.04 in a 1 mm thick optical cell.

4.3.2   Results
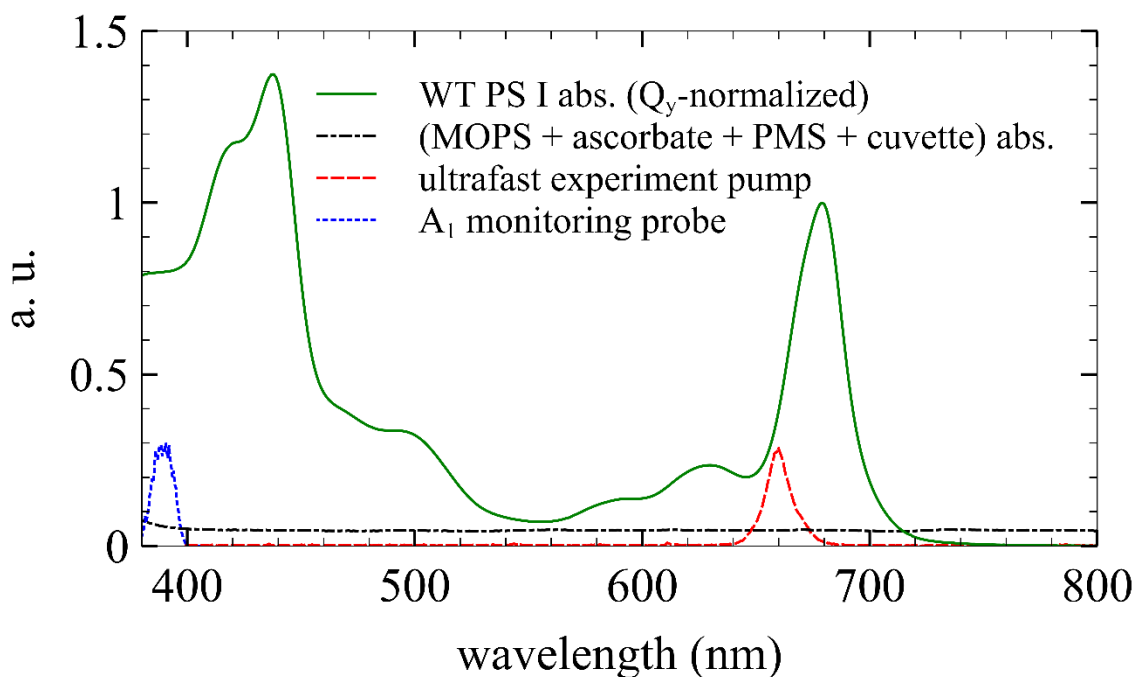
Figure 4.4: Here are compared the steady-state absorption spectra of WT PS I (solid green) and the solution in which PS I was dissolved plus the cuvette housing the entire sample (dash-dotted black), in arbitrary absorbance units. This shows that of the two, only PS I has any discernible features in the visible spectrum. The slightly greater absorbance on the blue end of the black curve is thought to belong to the quartz cuvette, which exhibits this feature even when empty. Superimposed onto PS I absorbance are the measured intensity profiles of the pump pulses (dashed red) used in ultrafast experiments (see Sections 4.5 – 4.7) as well as the probe pulses (dotted blue) used to monitor the A_1 redox state in the experiment of Section 4.6, both also scaled for visual clarity. A constant background has been subtracted from the former. Note that pump pulses were tuned to excite the blue edge of PS I's Q_y absorption band.

The WT PS I's steady-state absorption spectrum, shown in Figure 4.4, contains the familiar features, with Soret and Q_y peaks centered around 438 nm and 679 nm, respectively (Chauvet, Dashdorj, et al., 2012).

The Q_y bands of many mutant PS Is were blue-shifted by up to 2 nm relative to that of the WT. Based on the extent of the spectral changes, it was inferred that the point mutations introduced near the RC could not cause such large spectral shifts of the entire PS I complex. The only plausible explanation is that the mutant complexes displaying this effect lacked several "red" pigments—pigments absorbing on the red side of the cumulative PS I Q_y absorption band. To estimate the number of missing Chls, each normalized mutant's absorbance was rescaled by a factor <1 to be no greater than that of the WT anywhere within the Q_y region. An alternate scaling method, whereby all spectra are normalized according to the carotenoid-dependent Soret peak, was also attempted and yielded comparable results. The scaled spectra are shown in Figure 4.5 – Figure 4.7. Their insets highlight the absorbance difference between WT and mutant PS I, interpreted as the missing pigments' spectra. Multiplying each scaling factor by 96—the number of Chls per WT PS I complex—gives a crude approximation of the number of pigments remaining in each mutant PS I. Similar estimates were obtained by comparing absorbance integrals in the 600 – 800 nm range, a perhaps more accurate approach. The Q_y peak positions, scaling factors, integrals and estimated numbers of missing pigments are summarized in Table 4.1. Note that the spectra of the missing Chls indicate that these do not include A_{-1} or A_0, as their absorption in WT species has been reported to be around 682 nm and 684 – 687 nm, respectively (Chauvet, Dashdorj, et al., 2012; Hastings, Kleinherenbrink, et al., 1994; Savikhin, Xu, Martinsson, et al., 2001).

The greatest Chl deficiency was found in the A_{-1} mutants (Figure 4.5). The double mutant lacks 9 Chls, more than any of the other eight mutants studied. Its Q_y band is correspondingly the farthest blue-shifted relative to that of the WT. The mutation targeting the A-branch, along which most CS occurs in prokaryotes like *S.* sp. PCC 6803 (Cohen et al., 2004; Xu, et al., 2003), resulted in more missing pigments than that of its B-branch counterpart. The missing pigments in all three variants have their main absorption bands at 683 – 685 nm with ~20 nm FWHM, with a possible weak shoulder near 700 nm. The variants containing the A-branch mutation show a ~30 nm FWHM band at 640 nm, ~10% of the full amplitude.
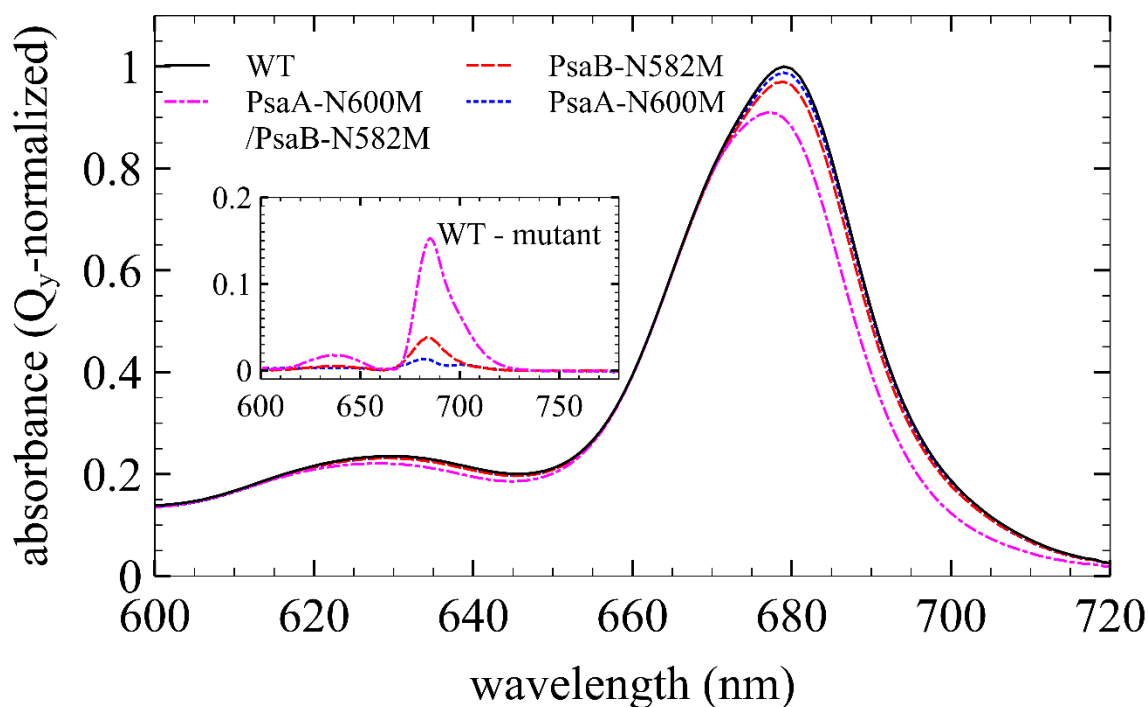
Figure 4.5: Q_y-region steady-state absorption spectra for WT and three A_{-1} mutants are shown, normalized by peak Q_y absorbance. Mutant absorbance has been scaled by a factor <1 to be just below that of WT within this range, and the difference is plotted in the inset. These difference spectra are interpreted as those of Chls missing from mutant PS I. The same procedure produced Figure 4.6 and Figure 4.7. The double mutant's Q_y maximum is blue-shifted by 2 nm. The main feature of the missing Chl spectra here, most pronounced in that of the double mutant, is the ~20 nm-wide peak centered around 685 nm.

In the Met→His family, (Figure 4.6) the double mutant lacked $6-7$ Chls, whose absorption spectrum exhibited a maximum at 684 nm (FWHM ~10 nm) with a clear shoulder of similar width near 695 nm. A ~30 nm FWHM component also appeared at 640 nm, as for the A_{-1} double mutant, but larger: ~15% of the maximum absorbance. The PsaA-M684H variant having absorbance nearly superimposable upon that of WT PS I—note the nearly flat spectrum ascribed to missing pigments—it is presumed to possess a full set of Chls. The situation is similar for PsaB-M659H, whose nominal missing pigments spectrum resembles that for PsaA-M684H. This suggests that that the minute differences between the WT and these two single mutants could be due to slight local changes in a few pigments around the point mutations rather than to minor Chl deficiencies as calculated.
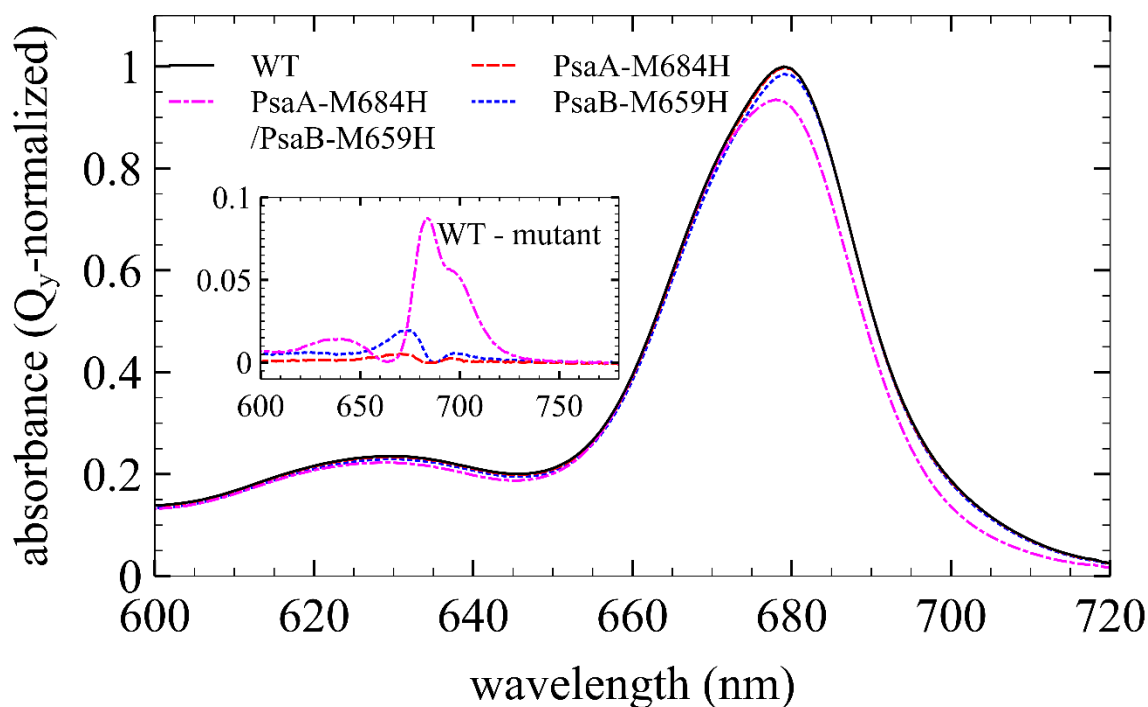
Figure 4.6: Refer to Figure 4.5 caption for data processing. The Met→His double mutation caused a 1 nm blue-shift in the Q_y absorbance peak. The (WT - mutant) absorbance difference spectrum of the double mutant (inset), exhibits a 684 nm peak with a shoulder near 695 nm, corresponding to an estimated 6 – 7 missing Chls. The single mutants' absorption spectra are nearly identical to that of the WT, suggesting that the minute differences may stem not from any Chl deficiency but from minor local differences in a few pigments surrounding the mutations.

The Tyr→Phe family was the only one of the three in which even the double mutant's Q_y absorbance maximum lay within (679 ± 0.5) nm (Figure 4.7), as was the case for WT and all four of the other single mutants. The double and single mutants each lacked 3 – 4 Chls, and all three variants' missing Chl absorbance spectra are strikingly similar. Two clearly defined bands are centered around 681 nm and 700 nm, with respective FWHM bandwidths ~10 nm and ~20 nm. The 700 nm band is only 70 – 80% as intense as the 681 nm one in the variants containing the PsaA mutation, whereas they are equal for PsaB-Y667F. The bimodal spectra may indicate excitonically coupled pigments (see Section 2.3).
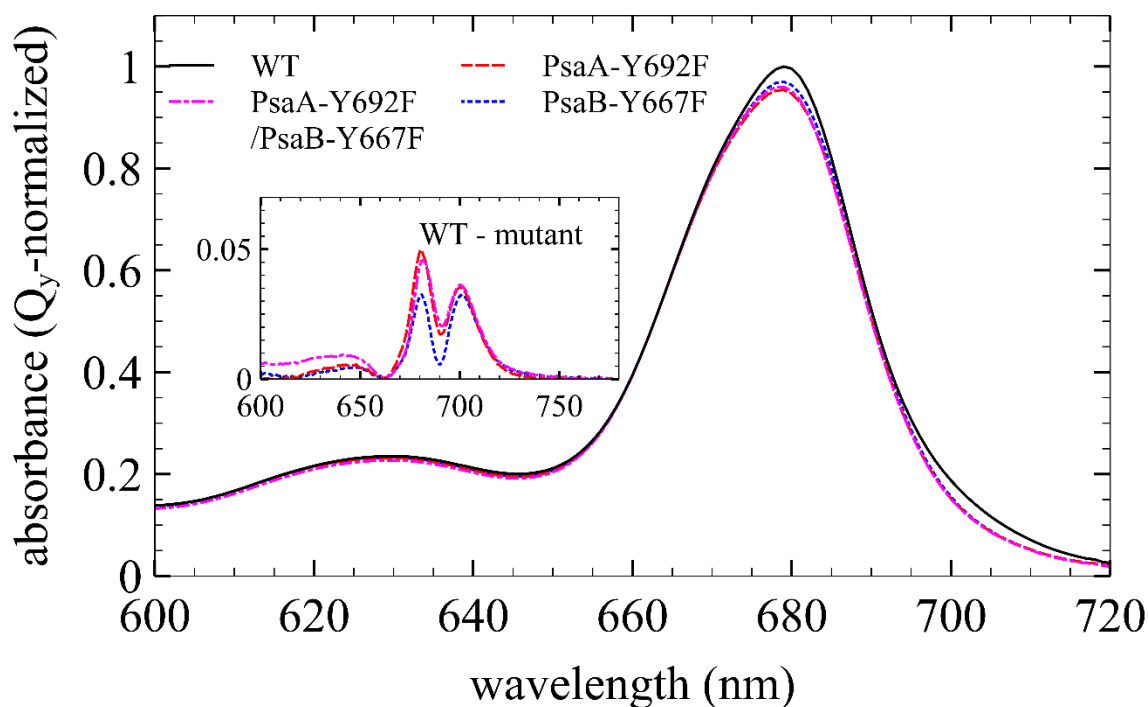
Figure 4.7: Refer to Figure 4.5 caption for data processing. The Tyr→Phe mutants' Q_y absorbance maxima are blue-shifted by less than 1 nm relative to that of the WT; however, the relative dip around 701 nm is obvious even before downscaling of the normalized mutant spectra. This feature, not observed in the Asn→Met or Met→His mutants, is highlighted in the missing Chl spectra (inset), which contain two distinct, similarly intense bands at 681 nm and 700 nm (FWHM ~10 nm and 20 nm, respectively). The bimodal spectrum suggests missing pigments which may be excitonically coupled.

Note that all mutant samples are very photo-stable, suggesting that the overall structure of the PS I was not affected much by these mutations. We can thus exclude the possibility that interruption in the ETC due to mutations leads to degradation of some Chls in the complex due to a higher rate of Chl triplet state formation and generation of singlet oxygen that is known to oxidize Chl-like molecules (Fromme & Grotjohann, 2006; Grotjohann & Fromme, 2005; Krieger-Liszkay & Trebst, 2006). It is therefore inferred that these mutants assemble PS I complexes initially with a smaller number of Chls. It is proposed that this occurs due to lower efficiency of mutant PS I complexes which, through complex feedback, affect synthesis of Chl *a* molecules. It is known that in cases where PS I is completely impaired, no Chl *a* is synthesized, and it is possible that in the case of partially impaired PS I in these mutants, the amount of synthesized Chl *a* in insufficient to fill in all the Chl *a* pockets in the PS I protein.

Table 4.1: The number of pigment missing from each variant of PS I was calculated based on both the scaling factor applied to its absorbance spectrum and the ratio of the absorbance integral of the mutant over the 600 – 800 nm range to that of the WT PS I. In both cases, calculations assume that a WT PS I complex contains 96 Chls. For the Asn→Met and Met→His variants, double mutations had a significantly larger impact on Chl content than either single mutation alone, with double mutants lacking at least thrice as many pigments as even the worse of the two corresponding single mutants. By contrast, in the Tyr→Phe variants, the additional mutation had little influence. Only the double Asn→Met and Met→His mutants showed measurable blue shifts in their Q_y maxima, with 1 nm resolution.

strain	Q_y center (nm)	scaling factor	missing pigments abs. integral	missing pigments (scaling)	missing pigments (integral)
WT	679	1	0	0	0
PsaA-N600M /PsaB-N582M	677	0.91	0.10	9	9
PsaB-N582M	679	0.97	0.02	3	2
PsaA-N600M	679	0.988	0.01	1	1
PsaA-M684H /PsaB-M659H	678	0.935	0.07	6	7
PsaA-M684H	679	0.998	0.00	0	0
PsaB-M659H	679	0.985	0.02	1	2
PsaA-Y692F /PsaB-Y667F	679	0.96	0.04	4	4
PsaA-Y692F	679	0.954	0.04	4	3
PsaB-Y667F	679	0.97	0.03	3	3

4.4 (P_{700}^+ - P_{700}) Absorption Difference Spectra

4.4.1 Method

PS I sample exposure to LED flashes temporarily oxidizes P_{700} dimers reversibly, with no need for chemicals. This means that the same sample preparations can be used to measure both normal steady-state absorbance and (P_{700}^+ - P_{700}) spectra, so the former can easily be used to normalize the latter (Savikhin, Xu, Chitnis, & Struve, 2000). The RC is said to be closed when its special pair is oxidized (P_{700}^+) and open otherwise. Normally, charge recombination from reduced terminal acceptors $[F_A/F_B]^-$ should take place in <100 ms. However, dissolved molecular oxygen scavenges a small portion of electrons from $[F_A/F_B]^-$, resulting in a long-lived P_{700}^+ state which can

last for hours in the absence of electron donors (Vassiliev et al., 1997). However, the several-second continuous LED flashes result in a sample in which nearly all RCs are closed. In this experiment, sodium L-ascorbate (ascorbate) was used as a slow electron donor which reduced the P_{700}^+ at a rate proportional to its concentration (Savikhin, Xu, Martinsson, et al., 2001). Closing the RC results in a PB signal at 700 nm, where the unoxidized P_{700} otherwise has an absorbance maximum.

PS I sample volumes for this experiment were typically 600 μL, housed in a 10 mm pathlength disposable cuvette sealed with Parafilm M. Ascorbate was added to a final concentration of 100 mM, reducing virtually all P_{700}^+ within a minute, and peak Q_y-band absorbance was within 0.9 ± 0.2. The modified spectrophotometer used is described in Section 3.4. Times τ_{dark}, τ_{LED} and τ_{cool} (defined in Section 3.4) were set to 60 s, 4 s and 2 s, respectively. These values were determined by a series of experiments using the spectrophotometer in kinetic mode, where P_{700}^+ reduction kinetics were recorded and fitted with monoexponential decay functions of the form $\Delta A(t) = \Delta A_0 \, e^{-t/\tau}$ (see Figure 4.8). In 100 mM ascorbate, virtually all P_{700}^+ became reduced after being kept in darkness for τ_{dark}=60 s, >4 times longer than the longest determined P_{700}^+ reduction lifetime. A series of tests showed that sample illumination beyond 4 s had no further effect on signal strength, hence τ_{LED}=4 s was saturating and promoted all PS I complexes into the closed state. Waiting τ_{cool}=2 s from the instant the LED was switched off was necessary as stray light from the illuminating source caused a brief period of detector saturation during which measuring was impossible.

4.4.2   Results

$(P_{700}^+ - P_{700})$ spectra are shown in Figure 4.9 – Figure 4.11, each normalized to a minimum value of ΔA=-1 in the Q_y region to facilitate spectral shape comparison. Actual signal amplitudes (normalized by maximum Q_y absorbance), reflecting the amount of P_{700}^+ formed, are visible in the insets and listed in Table 4.2. Because absorption was measured with delay τ_{cool} after the end of each LED flash (here, defined as time t=0), and because this measurement was an average over a period τ_{avg}=4 s, the raw values ΔA_{avg} recorded underestimated the total number of special pairs in the oxidized state at t=0. The tabulated values were extrapolated using the P_{700}^+ reduction time τ for each sample's slow kinetics to reflect the true signal ΔA_0 at t=0:

$$\Delta A_0 = \frac{\Delta A_{avg}\tau_{avg}}{\int_{\tau_{cool}}^{\tau_{cool}+\tau_{avg}} e^{-t/\tau}dt} = \frac{\Delta A_{avg}\tau_{avg}\, e^{\tau_{avg}+\tau_{cool}/\tau}}{\left(e^{\tau_{avg}/\tau}-1\right)\tau}. \tag{4.1}$$

This is shown graphically in Figure 4.8. Root mean square (RMS) noise in the ΔA kinetics was better than 2×10^{-4}, ~3% of the amplitude of the WT signal at 700 nm.
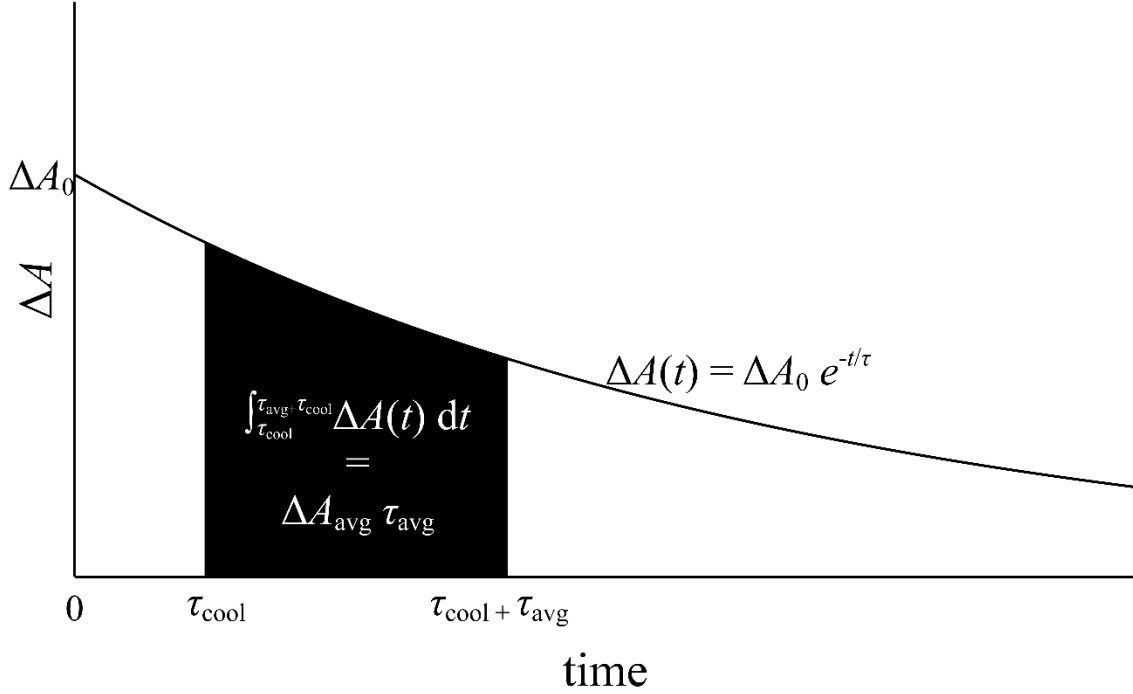
Figure 4.8: The principal components of Equation (4.1) are visualized here. The raw signal measured in the experiment corresponds to the shaded area, from which the value ΔA_0 was computed.

The WT's (P_{700}^+ - P_{700}) spectrum, comparable to that measured by Chauvet, Dashdorj, et al. (2012), is characterized by the P_{700} PB band (FWHM = 23 nm, centered at 701 nm) accompanied by an absorption features on either side. One is ~10 nm wide, centered around 689 nm, and has been previously ascribed to C690, the monomeric Chl of P_{700}^+ which is neutral while the other is oxidized (Savikhin, Xu, Chitnis, & Struve, 2000; Schaffernicht & Junge, 1981). The Chl^+ of the pair is attributed the other, broad absorption band near 800 nm. These features of the spectrum can be explained largely in terms of two phenomena. The electron missing from eC-A1, eC-B1 or a combination of both in P_{700}^+ (Breton et al., 1999) alters the excitonic absorption band structure of the six electronically interacting Chls of the RC. Additionally, the local electric field due to the displaced charge causes an electrochromic shift in the absorption of RC pigments

near P_{700}^+, the closest candidates being A_{-1} Chls (Dashdorj, Xu, Martinsson, et al., 2004). Similar features as in WT PS I can also be identified in most of the mutants' spectra, though they are usually weaker and sometimes blue-shifted by a small amount not exceeding a few nanometers.

Table 4.2: Actual signals measured in the conditions described, normalized by peak Q_y absorbance, and corrected using Equation (4.1), are listed under $\Delta A_{\text{closed - open}}/A_{\text{max}}$. The strength of this signal for each mutant is compared to that for WT in the last column.

strain	$\Delta A_{\text{closed - open}}/A_{\text{max}}$ $(\times\ 10^{-3})$	(mutant/WT) 700 nm signal (%)
WT	-8.3	100
PsaA-N600M /PsaB-N582M	-3.7	45
PsaB-N582M	-5.3	63
PsaA-N600M	-6.4	77
PsaA-M684H /PsaB-M659H	-0.81	10
PsaA-M684H	-4.3	51
PsaB-M659H	-7.9	95
PsaA-Y692F /PsaB-Y667F	-8.6	104
PsaA-Y692F	-8.8	106
PsaB-Y667F	-8.9	107

All three A_{-1} mutants (Figure 4.9) saw much less P_{700}^+ production than did WT PS I upon LED illumination, with double mutant, PsaB-N582M and PsaA-N600M signals 45%, 63% and 77% as intense as that of WT PS I at 700 nm. These results are in line with the idea that most ET proceeds along the A-branch in cyanobacterial PS I. These ratios do not strictly reflect forward ET efficiency in the mutants compared to WT: The long-lived 700 nm signals result from a series of consecutive excitations by continuous illumination and depend on the rate of back-transfer from $[F_A/F_B]^-$ to P_{700}^+ as well as the mechanism of reduction by ascorbate of P_{700}^+, which is not yet well understood and may therefore vary depending on mutations. Similar caution should be applied when considering other mutants' steady-state (P_{700}^+ - P_{700}) spectra. A close look at the bleaching band reveals a ~3 nm blue shift for the double mutant and lesser shifts in the single mutants compared to the WT. This most likely results from direct alteration of spectral properties of the A_{-1} Chls by the mutations and, because these are excitonically coupled to the other RC Chls

including those constituting P_{700}, the P_{700}^+ absorption spectrum is also altered. The B-branch mutant's normalized (P_{700}^+ - P_{700}) spectrum can be nearly superimposed onto that of the WT, with only a small difference in the C690 band, which is proportionally weaker than in the WT spectrum. The same C690 band, however, is almost absent from both variants containing the PsaB mutation; in these, there are no zero-crossings around 689 nm. This spectral difference is therefore attributed to a mutation-induced change in the A-branch A_{-1} Chl's electronic transition energy, and the remaining unpaired electron of P_{700}^+ is thought to spend most of its time near eC-B1. Given that the (P_{700}^+ - P_{700}) spectrum's total integral in the Q_y range is comparable to the absorbance of a single Chl a, the difference between the mutants' and WT's spectra are minor. (P_{700}^+ - P_{700}) spectra for mutants in which Asn was replaced with Gln, His or Leu are plotted in APPENDIX B
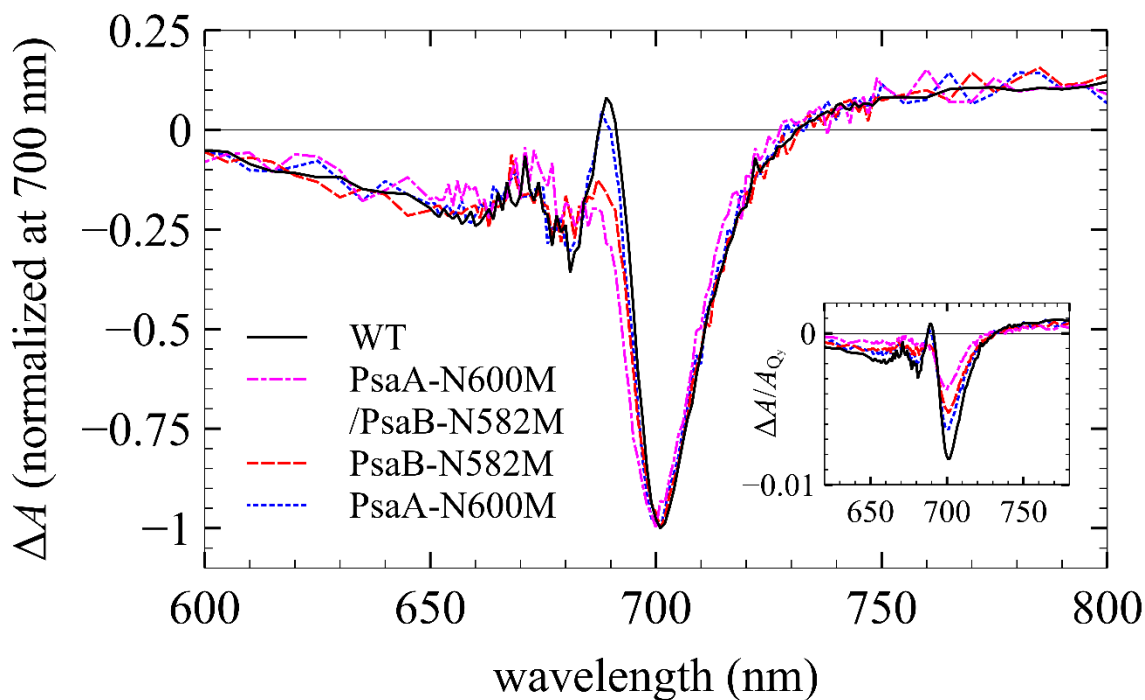
Figure 4.9: ~700 nm-normalized (P_{700}^+ - P_{700}) spectra are shown for WT and A_{-1} mutants. The single B-branch mutant's spectrum (dotted blue) is nearly superimposable onto that of the WT after normalization, whereas the double (dotted-dashed magenta) and A-branch (dashed red) mutants have significantly weaker 690 nm absorption bands, possibly indicating that the P_{700}^+ radical's excess positive charge is situated mainly on eC-A1. The mutants' 700 nm bleaching bands are blue-shifted by up to 3 nm relative to that of the WT. The inset, which reflects true signal amplitudes, shows that the Asn→Met mutation decreases long-living P_{700}^+ formation in all three cases, most affecting the double and A-branch mutants (see Table 4.2). This is not surprising given that more ET proceeds along the A-branch in cyanobacterial PS I RCs.

The Met→His set's mutants (Figure 4.10) also experienced a significant decrease in their ability to form P_{700}^+, with bleaching band amplitudes for the double, A-branch and B-branch mutants at 10%, 51% and 95% that of the WT, respectively. This band was blue-shifted by ~2 nm for both variants containing the PsaA-M684H mutation. Note that the effects of individual mutations on either branch were far from additive: Damage to the A-branch alone decreased P_{700}^+ yield by half, and damage to the B-branch alone has little influence at all, but complexes containing both mutations struggled to form any long-living P_{700}^+. This result also agrees with the commonly accepted idea that in cyanobacterial PS I, the A-branch dominates ET. Additionally, it suggests that very little ET can proceed along the mutated branch or that back-transfer along this path is efficient, but if only one branch is damaged, more ET will take place along the intact one.
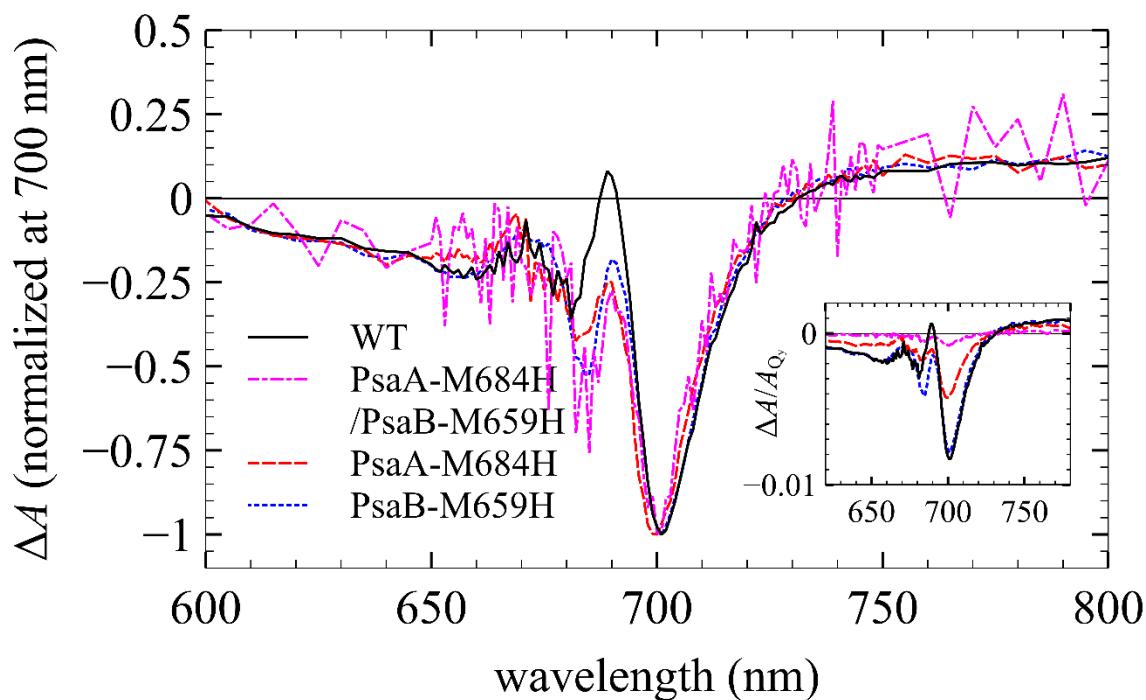
Figure 4.10: ~700 nm-normalized (P_{700}^+ - P_{700}) spectra are shown for WT and Met→His variants of PS I. All three mutants' C690 absorption bands are greatly diminished, leaving only the broad absorption feature around 800 nm, attributed to the Chl^+ within P_{700}^+, and the bleaching bands at 700 nm and 682 – 684 nm. The nominal 700 nm bleaching bands are blue-shifted by ~2 nm in both variants containing an A-branch mutation. The double mutant signal at 700 nm is much weaker than those of the other variants, as seen in the inset, which reflects the true signal amplitudes.

The Tyr→Phe family (Figure 4.11) was the least affected; its ability to form long-lasting P_{700}^+ was close to that of the WT. The P_{700}^+ bleaching bands for the double, A-branch and B-branch

mutants had respective amplitudes measured at 104%, 106% and 107% that of the WT—comparable, given the measurements' precision. These bands, however, were blue-shifted relative to that of the WT, by 2 nm for the double mutant and 1 nm for the single mutants, reminiscent of the blue shifts observed in the six axial ligand mutants. The 690 nm absorption bands are also both weaker and 1 nm blue-shifted compared to that of the WT, though this effect is stronger in the mutant whose B-branch is targeted, contrasting with the results from the A_{-1} mutants.
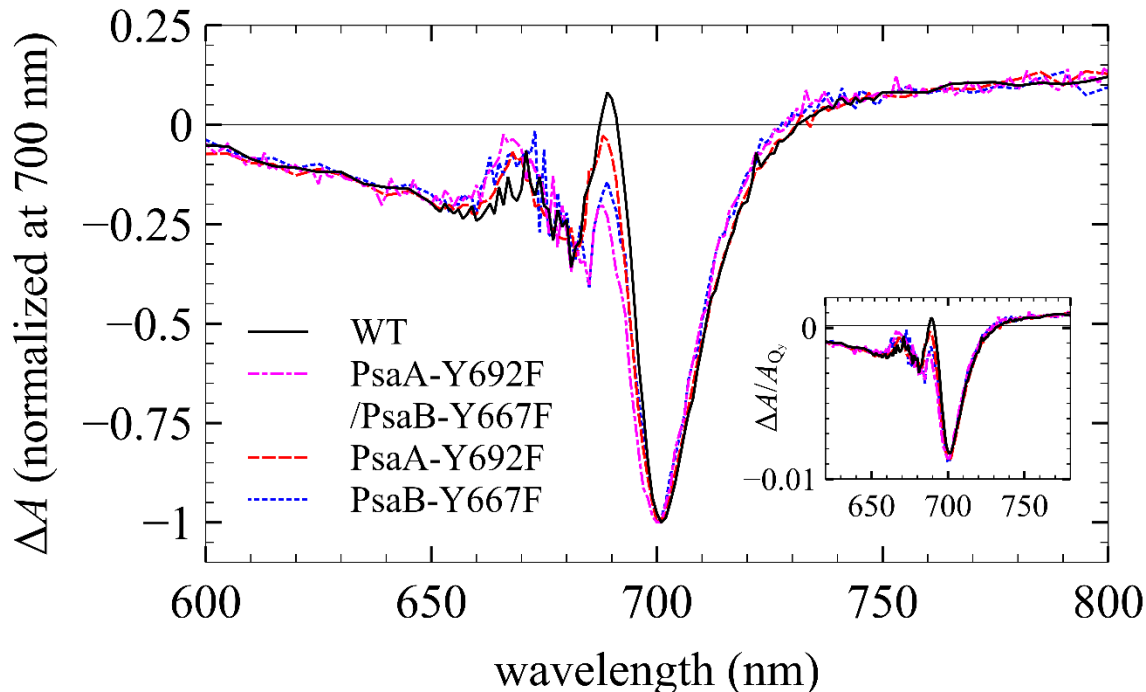
Figure 4.11: ~700 nm-normalized (P_{700}^+ - P_{700}) spectra are shown for WT and Tyr→Phe variants of PS I. The principal effect observed of the Tyr→Phe mutation is a weakening of the 690 nm absorption band relative to bleaching at 700 nm. In both strains containing the A-branch mutation, this band is also blue-shifted by ~1 nm. The actual signal amplitudes shown in the inset show that long-lived P_{700}^+ yield was not significantly affected by these mutations.

4.5   Decay-Associated Difference Spectra (DADS)

4.5.1   Method

These experiments were performed using the fs pump-probe spectrometer described in Section 3.2. WT and all six axial ligand mutant PS I samples were prepared similarly to those used in Section 4.4, save that the final ascorbate concentration was only 80 mM, and fast electron donor N-Methylphenazonium methyl sulfate (PMS) was added to a final concentration of 80 μM. Steady-

state Q_y band amplitudes were kept in the approximate 0.6 ± 0.1 range. Each sample was housed in a 1 mm pathlength quartz cuvette kept in continuous motion by the shaker described in Section 3.3, at linear speed ≥ 16 mm/s. The octagons described by the shaker were kept large enough (D1 $\geq$ 5 mm) to ensure that the sample's speed never dropped below the specified setting. For a typical round Gaussian pump beam focused to a spot of radius of ~200 μm in the sample, an average portion of sample traversed by it saw ~10 consecutive pulses at 500 Hz before moving out of the beam path. The two reducing agents' concentrations, as well as the shaker's speed, were determined in a series of experiments in which each concentration, in turn, was increased incrementally, in steps of 20 mM for ascorbate and 20 μM for PMS. This was repeated until "long time" (hundreds of picoseconds) signals of the WT sample reached a maximum value beyond which further addition of reducing agents made no noticeable difference in the signals measured, indicative of full P_{700}^+ recovery to a neutral state between consecutive pump pulses. The shaker speed setting was determined in a similar way, varied incrementally for each combination of reducing agent concentrations and observing long-time signal amplitudes.

Samples were pumped at 660 nm, exciting the blue edge of the Q_y absorption band (see Figure 4.4), and probed in the range sweeping wavelengths 665 – 705 nm in 2.5 nm increments as well as 705 – 720 nm in 5 nm increments, with the monochromator operated at $\lesssim 3$ nm bandpass. The choice of pump wavelength allowed some of the higher-energy Chls to be excited, permitting some monitoring of EET within the antenna. At each wavelength, one ΔA kinetic curve was measured over the range -40 – 600 ps (probe delay relative to pump), after which the monochromator moved to the next wavelength. Typical RMS noise in ΔA for 1 s accumulation time was of the order of 10^{-5}, so the full set of wavelengths was scanned several times in this manner, averaging to obtain better signal-to-noise ratio. Signals at negative delays served as a baseline subtracted from the entire corresponding curve as there are no absorption differences due to a pump pulse prior to its arrival, $\Delta A(t<0) = 0$. The pump and probe beam polarizations were separated by the magic angle, 54.7°, to avoid anisotropy effects from energy transfer at very short (few-picosecond) times. Annihilation, caused by overexciting samples such that a single PS I complex contains more than one excitation at any given time and leading to the appearance of faster antenna excitation decay, was identified and avoided by performing a series of quick time scans probing at 700 nm, in which pump power was incrementally reduced until the ratio of short-time (~10 ps) to long-time (~600 ps) signals became constant with pump power variations.

4.5.2 Results
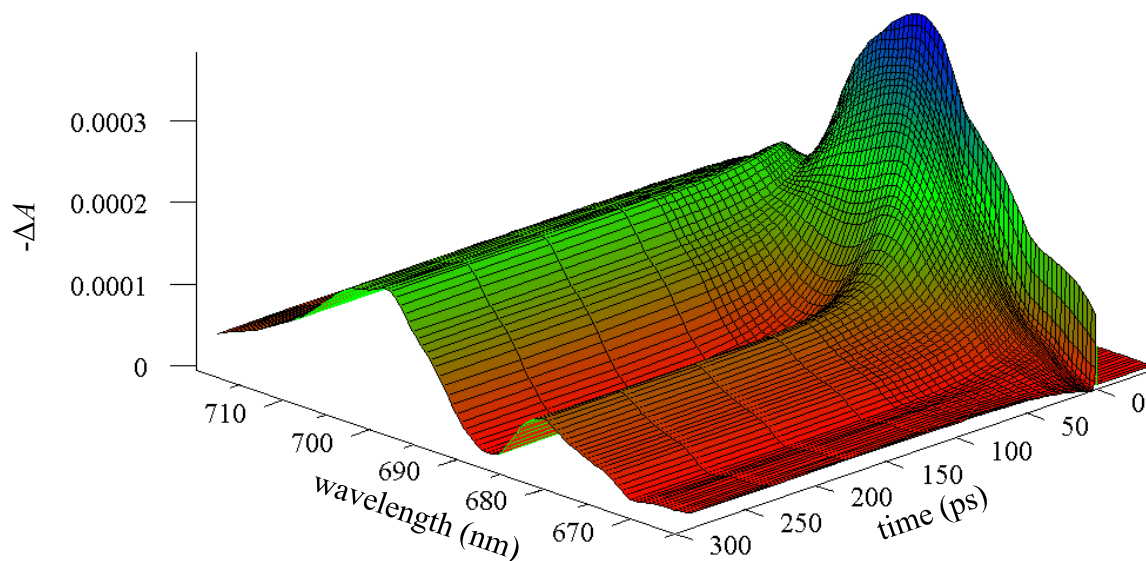
Figure 4.12: ΔA kinetics were measured around the Chl a Q_y region to 600 ps after a 660 nm pump pulse. The surface shown here represents a 4-lifetime global fit to the data. Note that the ΔA axis direction is inverted (negative direction up) to facilitate visual interpretation.

For each PS I variant, the kinetics were globally fitted as a function of time t and probe wavelength λ according to

$$\Delta A(t, \lambda) = \sum_{i=1}^{N} \alpha_i(\lambda) e^{-t/\tau_i}, \tag{4.2}$$

where each of the N terms is a component of amplitude α_i corresponding to lifetime τ_i. A set of lifetimes τ_i was found to fit all kinetic curves for each variant, and the set of amplitudes α_i was allowed to vary for each probe wavelength. This global fitting procedure resulted in N decay-associated difference spectra (DADS) plotted against probe wavelength. Each DADS, was ascribed to a specific process occurring in PS I on the basis of its spectral shape and characteristic lifetime τ_i. Global data from each sample in this experiment could be fitted with N=4 component DADS. Fits for the WT kinetics have been joined into a representative surface plotted in Figure 4.12. The DADS for WT is compared with those of the Asn→Met and Met→His mutants in Figure 4.13 and Figure 4.15, respectively.

Global data for WT PS I were fitted with the following four lifetimes: 0.57 ps, 2.0 ps, 26 ps, and a long lifetime far exceeding the experiment's 600 ps scope. The two shortest components, are characteristic of fast energy transfer from higher- to lower-energy pigments, as evidenced by the

bimodal ΔA signals, which are negative at shorter wavelengths and positive at longer wavelengths (Hastings, Reed, et al., 1995; Holzwarth et al., 2006; Müller, Niklas, et al., 2003; Savikhin & Jankowiak, 2014; Savikhin, Xu, Chitnis, & Struve, 2000; Savikhin, Xu, Soukoulis, et al., 1999). The shorter lifetime is ascribed to bulk antenna Chls' rapid spectral equilibration, whereas the longer lifetime corresponds specifically to slower EET to the red-most-absorbing antenna Chls. The 26 ps component is ascribed to the antenna decay process, this lifetime corresponding to the effective time of excitation trapping by the RC (Gatzen et al., 1996; Müller, Niklas, et al., 2003). Comparable antenna excitation lifetimes (23 – 28 ps) have been reported in similar experiments (Hastings, Hoshina, et al., 1995; Hastings, Reed, et al., 1995; Melkozernov et al., 1997; Savikhin, Xu, Chitnis, & Struve, 2000). The so-called "long" component DADS reflects all processes with lifetimes much longer than the 600 ps range explored. Its shape is characteristic of the P_{700}^+ state which lives for milliseconds, resembling that of the (P_{700}^+ - P_{700}) spectrum measured in Section 4.4 (see Figure 4.9 – Figure 4.10). It contains the same 700 nm PB band combined with the 690 nm absorption feature, as compared in Figure 4.14 and Figure 4.16. This result agrees well with previous studies (Hastings, Hoshina, et al., 1995; Melkozernov et al., 1997; Savikhin, Xu, Chitnis, & Struve, 2000). The only difference in the RC between these two measurements is that at 600 ps, A_1 is still reduced, as ET to F_X takes at least tens of nanoseconds, whereas A_1 is back to neutral when the steady-state spectrum is recorded (Brettel, 1988; Joliot & Joliot, 1999; Mathis & Sétif, 1988; Sétif & Brettel, 1993). Despite the A_1 PhQ lacking absorption features in the Q_y region of Chl a, the local electric field resulting from its reduction can cause an electrochromic shift in nearby Chls a, such as A_0, which does affect the long DADS to a small extent (Dashdorj, Xu, Martinsson, et al., 2004). The data shown here, unfortunately, lack the precision to show such minor effects.
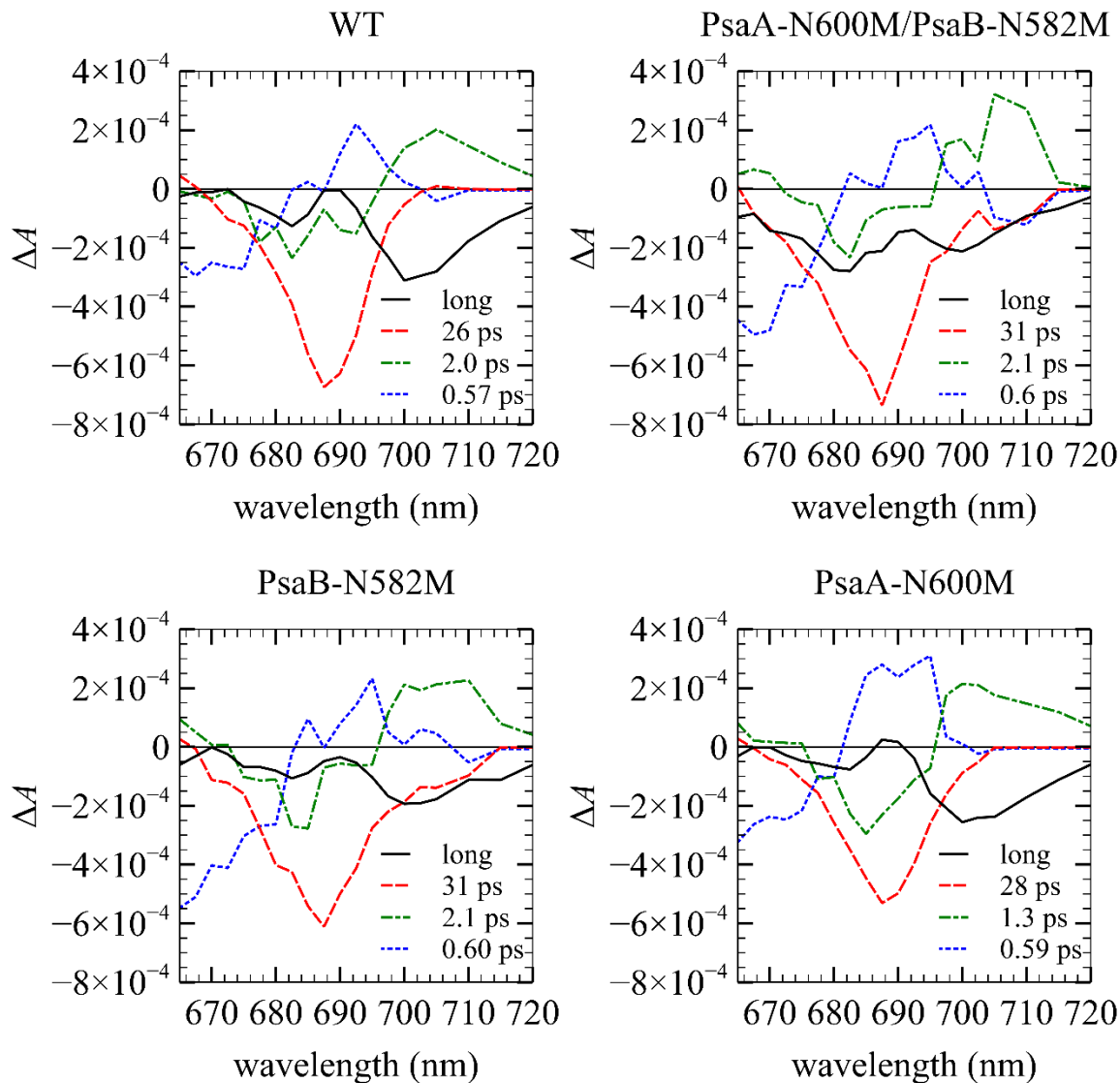
Figure 4.13: DADS for WT and Asn→Met PS I are shown, all signals as measured under the specified experimental conditions, not scaled. The two shortest components (<3 ps, dotted blue and dashed-dotted green curves) correspond to energy transfer from higher-energy to lower-energy antenna Chls. The 26 – 31 ps component (dashed red curve) corresponds to the antenna decay process and effective RC excitation trapping time. The long component DADS (solid black curve)—the sum of signals not decaying appreciably within the experiment's 600 ps range—is characteristic of the long-living P_{700}^+ state and comparable to the (P_{700}^+ - P_{700}) spectra shown in Section 4.4, except in the case of the double mutant. This DADS is somewhat weaker in the A-branch mutant, indicating lower efficiency in forming P_{700}^+. The long component of the double mutant is thought to result from $^T P_{700}^*$ formation.
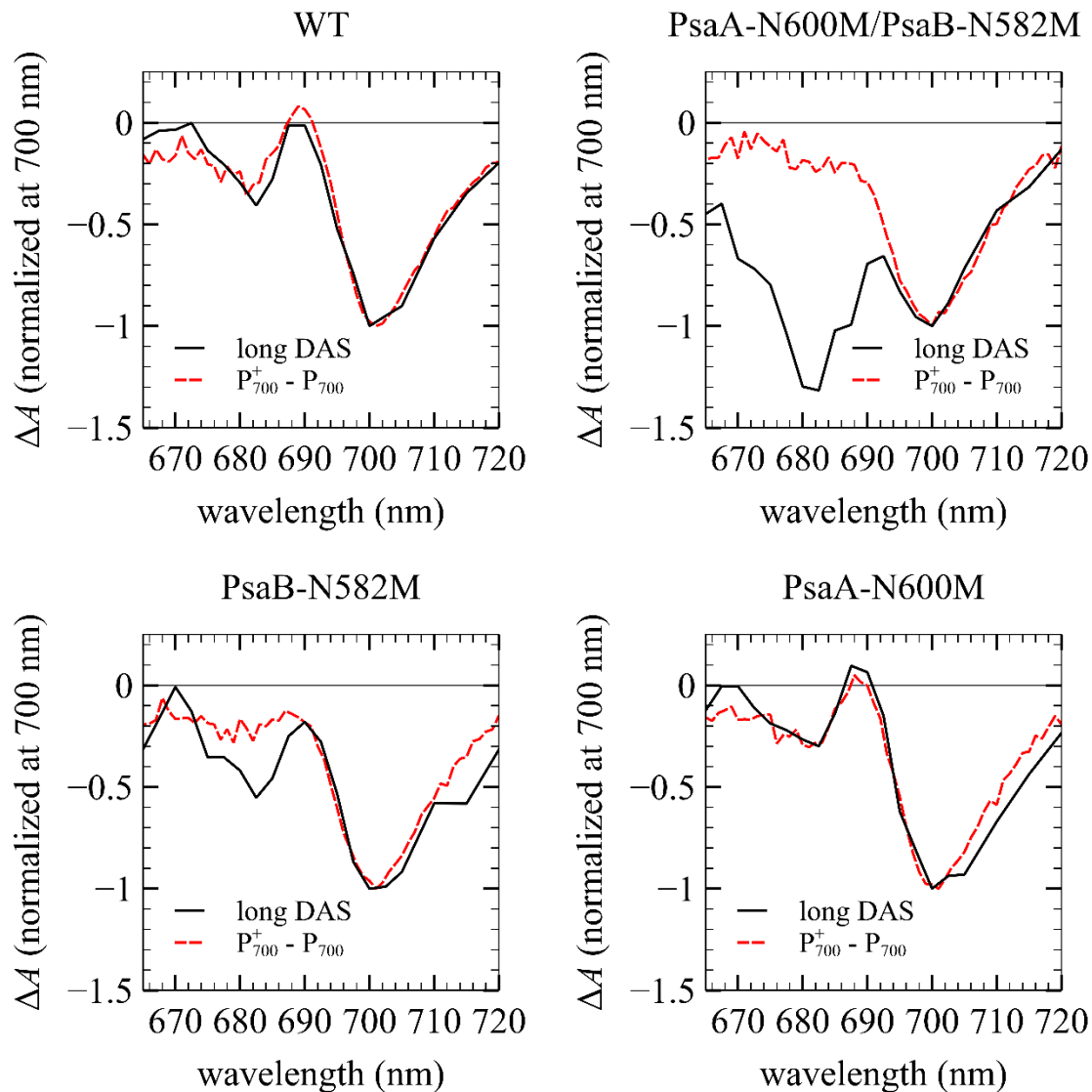
Figure 4.14: Long component DADS and (P_{700}^+ - P_{700}) spectra are compared for WT and Asn→Met mutants by normalization around 700 nm. The long DADS of the WT and B-branch mutant agree well with their respective (P_{700}^+ - P_{700}) spectra. Discrepancies exist for the double and A-branch mutants, the former showing a PB band at 680 nm only in the long DADS, suggesting $^TP_{700}^*$ formation by 600 ps.
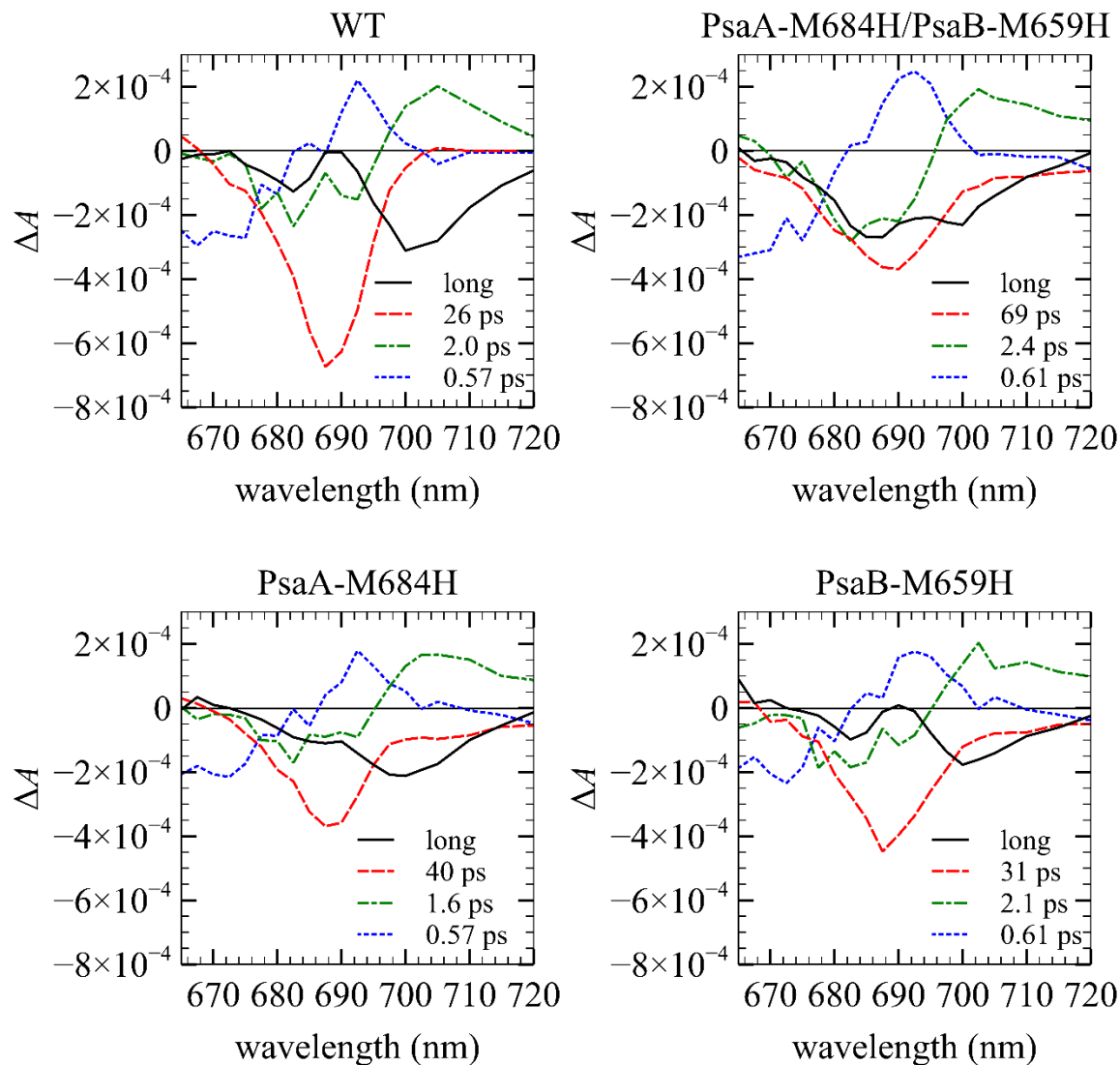
Figure 4.15: DADS for WT and Met→His PS I are shown, all signals as measured under the specified experimental conditions, not scaled. For similar amplitudes of the two short component DADS (dotted blue and dashed-dotted green), all three mutants' antenna decay DADS (dashed red) have only 50% − 60% of the amplitude seen in the corresponding WT DADS. The lifetime for this DADS is increased most in the double mutant, which was best fitted with 69 ps, nearly 3 times as long as for the WT. The long components of both variants containing the A-branch mutation lack the 690 nm absorption band. The double mutant's long component also has a more intense PB feature than observed in the other strains around 685 nm, likely indicating $^{T}P_{700}^{*}$ formation.
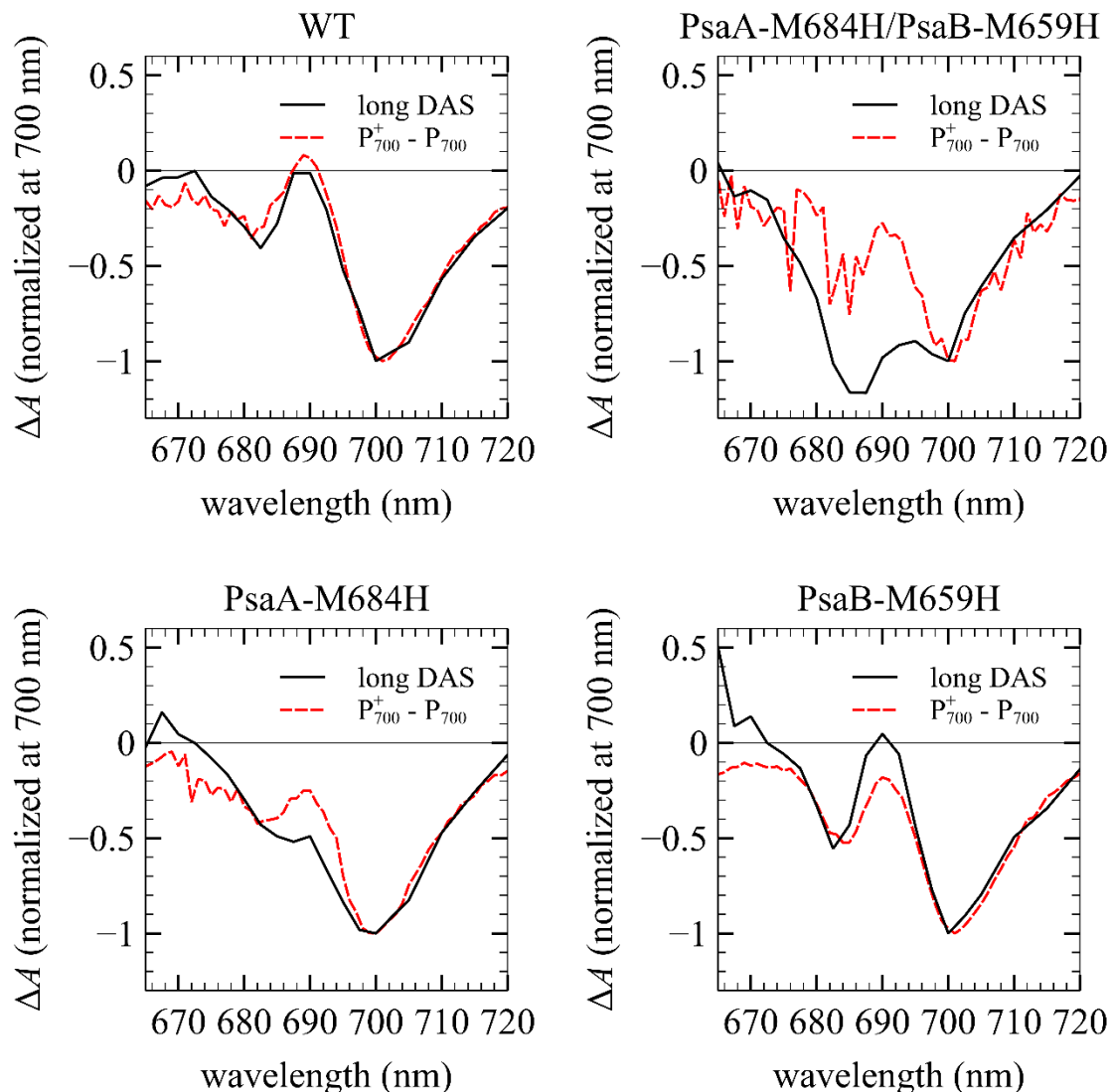
Figure 4.16: Long component DADS are compared with (P_{700}^+ - P_{700}) spectra for WT and all three Met→His mutant PS I by normalization of signals around 700 nm. The single mutants' 700 nm bleaching bands from both spectra agree well, though discrepancies are found between the ~680 nm bleaching and 690 nm absorption features. High noise in the double muant's (P_{700}^+ - P_{700}) spectrum makes the comparison more difficult, though P_{700}^+ bleaching can still be discerned in both spectra. The long component DADS in this case has a stronger bleaching feature near 685 nm than that at 700 nm, indicating $^TP_{700}^*$ formation.

The Asn→Met mutants' two shorter-lifetime DADS are comparable to those of WT PS I (see Figure 4.13). The B-branch mutant's global fit includes a 1.3 ps lifetime in place of the ~2.0 ps time found for the other three strains, though the spectral shapes are similar in all cases, and uncertainty is greatest for shorter lifetimes DADS. The excitation trapping times of all mutants are

only marginally longer than those of the WT: 31 ps for the double and A-branch mutants, and 28 ps for the B-branch mutant, which may still be within experimental uncertainty of the WT excitation trapping time. The shapes of these and both shorter component DADS are comparable for all four strains. The ratio of long component DADS amplitude to antenna decay signal is lower for the A-branch mutant than the WT, potentially indicating a lower P_{700}^+ formation efficiency of the former. In the double mutant, the shape of the long component DADS is markedly different from those of all other strains, as its PB band around 700 nm is weaker than that near 680 nm, and the 690 nm absorption band is much less pronounced than in the other three variants. These differences are likely indications of triplet excited state formation ($^TP_{700}^*$) on the special pair Chls. A triplet state may last for microseconds and would easily outlive the sub-nanosecond range of the ultrafast experiment, but its signature would not appear in the (P_{700}^+ - P_{700}) spectrum. This suggests that the long-lasting state observed in the ultrafast experiment is not primarily P_{700}^+ but rather $^TP_{700}^*$. Figure 4.14 compares the long component DADS with the (P_{700}^+ - P_{700}) spectrum for each of the four variants, showing minor differences for the single mutants but a clear discrepancy for the double mutant, illustrating this conclusion.

The Met→His mutation did not significantly affect the two shorter component DADS but, when applied to the A-branch, it measurably slowed the observed antenna decay process (see Figure 4.15). The respective excitation trapping times for the double, A-branch and B-branch mutants were 69 ps, 40 ps and 31 ps. The corresponding components were also notably less intense than in the WT: ~60% of its intensity of the double and A-branch mutants, and ~70% for the B-branch mutant. The long-time DADS's shape remained unchanged for the B-branch mutant, whereas the double mutant's corresponding DADS roughly resembles that observed in the A_{-1} double mutant, with an even weaker absorption feature near 690 nm. Similarly, this finding leads to the interpretation that by ~600 ps, most complexes have reached a state involving $^TP_{700}^*$ rather than P_{700}^+. The A-branch mutant's long DADS is comparable to that of WT PS I, save that it largely lacks the 690 nm absorption feature. However, its negative feature near 680 nm is not stronger than that of the WT, in proportion to its own 700 nm bleaching band. It is possible that by 600 ps, A-branch mutant PS I complexes, have formed some $^TP_{700}^*$ though a smaller yield than in the double mutant. Comparisons between these long DADS and the (P_{700}^+ - P_{700}) spectra are provided in Figure 4.16. This figure highlights the A-branch mutant's lack of a clear absorption band at 690 nm, which shows up only in its (P_{700}^+ - P_{700}) spectrum. The corresponding band is somewhat

weaker in the B-branch mutant's (P_{700}^+ - P_{700}) spectrum than in its long DADS. These minor changes at 690 nm may result from slight, mutation-induced alterations of the excitonic spectrum depending on the interactions among all RC Chls. The comparison is more difficult for the double mutant, whose (P_{700}^+ - P_{700}) signal-to-noise ratio is small due to the weak signal, but as with the A_{-1} double mutant, the long DADS contains a clear bleaching band near 685 nm which is not prominent in the (P_{700}^+ - P_{700}) spectrum.

4.6 A_1 Reduction Dynamics

4.6.1   Method

A_1 reduction dynamics were measured using a similar method to that described in Section 4.5, the only difference being in probe wavelength. The absorption spectrum of A_1^- contains a Soret band in the $380 - 390$ nm region, allowing direct monitoring of A_1 reduction, as P_{700}^+ does not contribute to ΔA at such wavelengths (Brettel, 1988; Brettel & Vos, 1999; Dashdorj, Xu, Cohen, et al., 2005; Giera et al., 2009; Lüneberg et al., 1994). A frequency-doubling crystal replaced the sapphire plate in the detection system (see Section 3.2) to produce probe light specifically around 390 nm rather than a broadband continuum. The resulting probe spectrum is included in Figure 4.4. The samples described in Section 4.3 were used, with peak Q_y absorbance within 0.68 ± 0.04. Signals shown below have been scaled by this absorbance maximum.

4.6.2   Results

The model of Equation (4.2) was used to fit 390 nm probe kinetics, with all parameters listed for WT and all mutant PS I in Table 4.3. Four decay components had imposed lifetimes fixed at the values extracted from the Q_y global analysis of Section 4.5.2, and their amplitudes relative to that of the full signal were as follows: 0.57 ps (-2.5%), 2.0 ps (5.8%), 26 ps (94%), and long (-33%). Following earlier works (Brettel & Vos, 1999; Dashdorj, Xu, Cohen, et al., 2005; Giera et al., 2009; Shelaev et al., 2010), the two shorter lifetimes are ascribed to spectral equilibration, and the negative signal in the first ~30 ps after excitation is ascribed to antenna bleaching. The A_1 PhQ's reduction appears as the nondecaying positive signal because A_1^-, which absorbs light at 390 nm, needs at least ~20 ns to donate its extra electron to F_X (Brettel, 1988; Joliot & Joliot, 1999; Mathis & Sétif, 1988; Sétif & Brettel, 1993). P_{700}^+ also lives long enough to

be detected well-beyond 600 ps but does not absorb light significantly at this wavelength (Brettel & Vos, 1999). Therefore, comparing the long component's amplitude to that of the negative short-time signal reveals the efficiency of A_1 reduction.

Table 4.3: Fit parameters for ultrafast A_1 reduction dynamics experiment are summarized. Each pair of columns (Asn→Met, Met→His and Tyr→Phe) represents one of the three mutant families under investigation. The top section lists the WT parameters three times identically to facilitate comparison with any mutant. Note that all three Asn→Met mutants required a fifth, ~100 ps component not found for other strains, ascribed to slow reduction of A_1.

family→	Asn→Met		Met→His		Tyr→Phe	
affected RC branch ↓	lifetime (ps)	relative amplitude (%)	lifetime (ps)	relative amplitude (%)	lifetime (ps)	relative amplitude (%)
WT	long	-33	long	-33	long	-33
	26	94	26	94	26	94
	2.0	5.8	2.0	5.8	2.0	5.8
	0.57	-2.5	0.57	-2.5	0.57	-2.5
double	long	-11	long	-5.5	long	-28
	150	38	69	63	-	-
	31	54	12	31	27	91
	2.1	-2.9	2.4	-0.4	8.1	-6
	0.6	7.8	0.61	5.9	0.8	9
A-branch	long	-34	long	-38	long	-31
	150	21	-	-	-	-
	31	74	40	89	25	91
	2.1	1.6	1.6	10	8.8	-6
	0.6	3.5	0.57	0.3	0.8	8
B-branch	long	-37	long	-34.	long	-32
	90	7.6	-	-	-	-
	28	86	31	91	27	92
	1.3	0.5	2.1	0.6	9.7	-5
	0.59	5.7	0.61	8.5	1.0	8
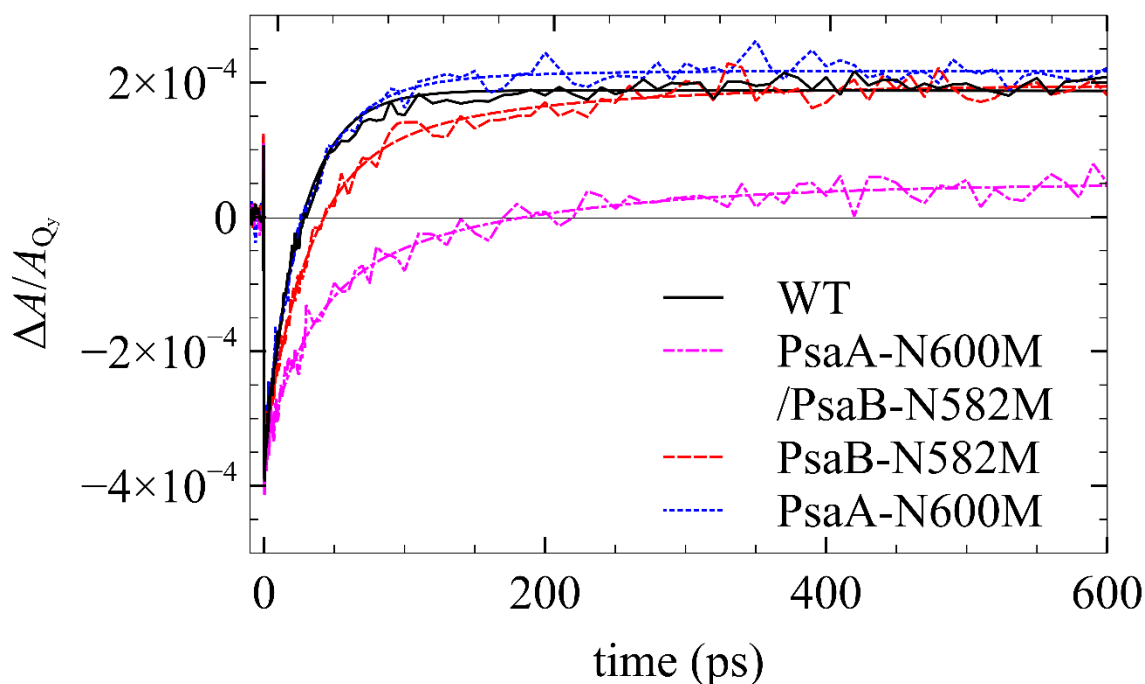
Figure 4.17: WT (solid black) and A_{-1} mutant kinetics at 390 nm have been normalized to the WT's early $\Delta A/\Delta A_{Q_y}$ signal for comparison of A_1^- yields relative to antenna bleaching. Theoretical fits are shown with smooth curves of matching styles and colors. The single mutants' (dashed red and dotted blue) A_1^- yields are very close to that of the WT, whereas the A_1^- yield of the double mutant (dashed-dotted magenta) is thrice less.

390 nm kinetics of each A_{-1} mutant, shown in Figure 4.17, were fitted using the four lifetimes found in its global Q_y analysis, plus a fifth component of lifetime ~100 ps, ascribed to a slow population of the A_1^- state. The long component for the A-branch mutant is slightly weaker than that for the B-branch mutant, which may indicate that the former's ET to A_1 is more strongly affected if reduction of PhQ-A and PhQ-B have equal effects on the RC's absorbance. The double mutant's long component, at just -11% of the amplitude of the total signal, is thrice as weak as those of the single-mutant and WT PS I, suggesting inefficient A_1 reduction. The possibility of a mutation-induced spectral shift of A_1 has also been considered, but the A_1 Chl is located far from the mutation near A_{-1}'s axial ligand, making such a shift unlikely; furthermore, the probe spectrum, though centered at 390 nm, was ~10 nm wide (see Figure 4.4), easily encompassing any minor spectral shifts affecting A_1^-'s Soret absorption band.
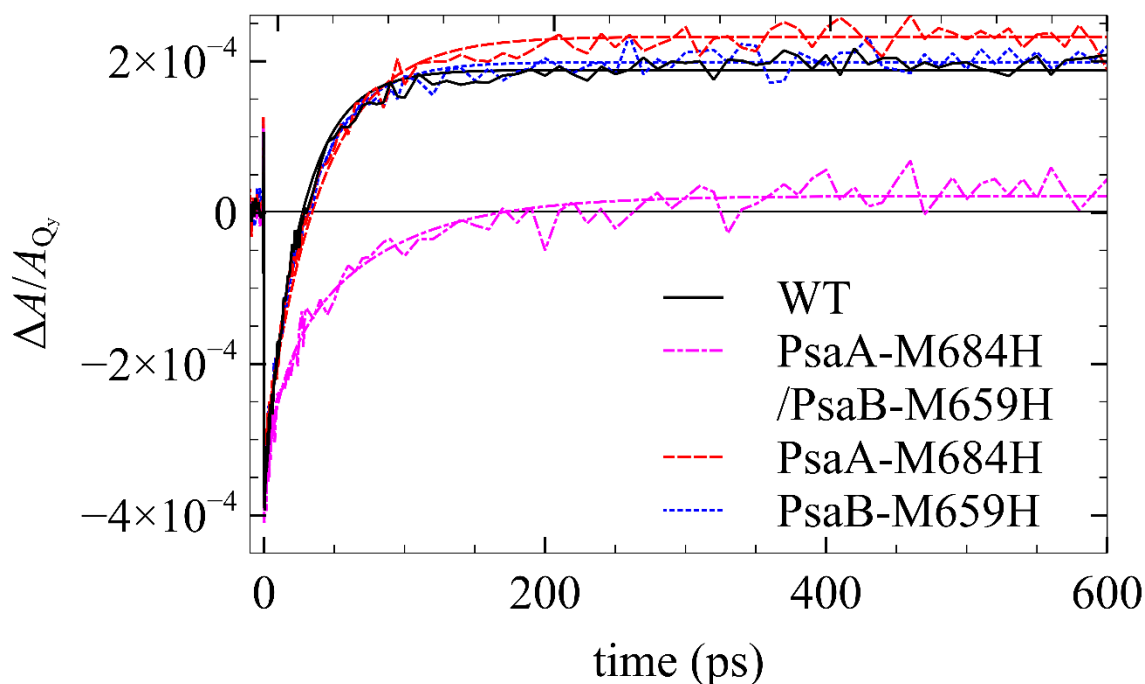
Figure 4.18: WT (solid black) and Met→His mutant kinetics at 390 nm have been normalized to the WT's early $\Delta A/\Delta A_{Q_y}$ signal for comparison of A_1^- yields. Theoretical fits are shown with smooth, curves of matching styles and colors. Single mutants (dashed red and dotted blue) are largely unaffected in A_1^- formation, as seen by their signals' near overlap with that of the WT. The double mutant's (dashed-dotted magenta) long-living positive signal is only ~20% as strong as that of the WT, indicating poor A_1 reduction.

The Met→His single mutants' 390 nm kinetics could be fitted adequately using the same lifetimes as found in their respective Q_y global analyses. For the double mutant, a fifth component of lifetime 12 ps was included for good agreement between the measured and fitted curves.

The Tyr→Phe family's 390 nm kinetics (Figure 4.19) were the least affected, nearly overlapping with those of WT, with fitting parameters comparable to those of the WT. This suggests that the lost peripheral H-bond to A_0 plays no significant part in ET to A_1.
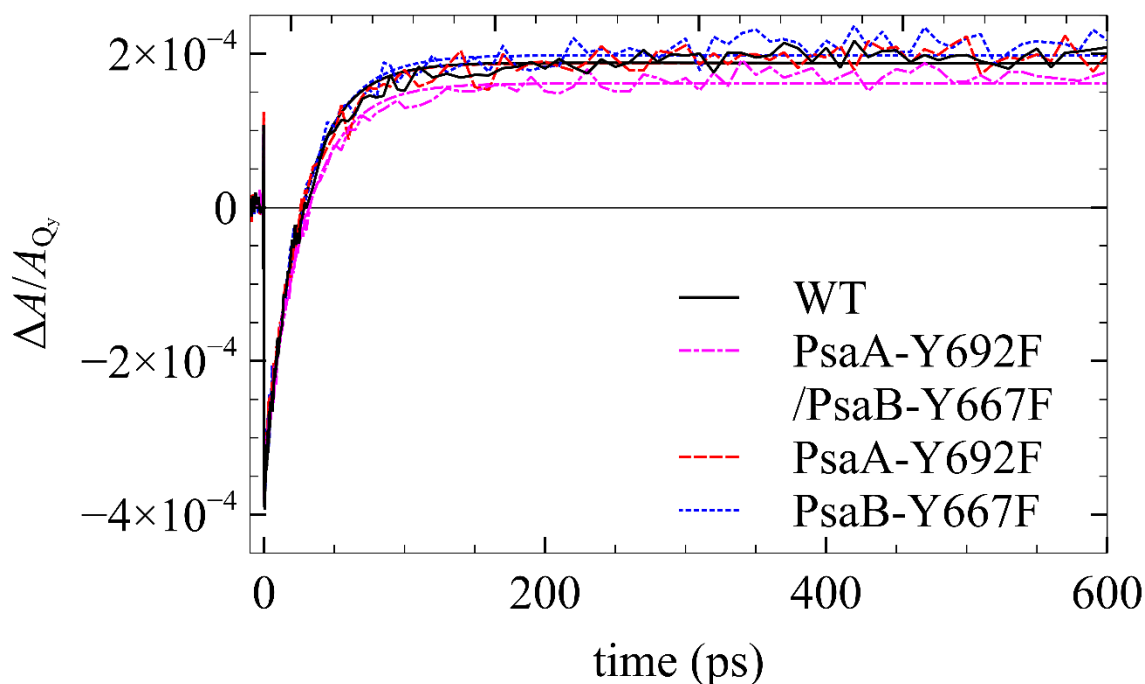
Figure 4.19: WT (solid black) and Tyr→Phe mutant kinetics at 390 nm have been normalized to the WT's early $\Delta A/\Delta A_{Q_y}$ signal for comparison of A_1^- yields. Theoretical fits are shown with smooth, curves of matching styles and colors. The overlap with WT data suggests that this mutation does not measurably affect A_1 reduction, as confirmed by fitting parameters.

4.7   Ultrafast (Open - Closed) RC Spectroscopy

4.7.1   Method

Many studies have shown that the dynamics of energy transfer and trapping in PS I are nearly independent of the oxidation state of P_{700} (Hastings, Kleinherenbrink, et al., 1994; Kumazaki, Kandori, et al., 1994; Nujis et al., 1986; Savikhin & Jankowiak, 2014; Savikhin, Xu, Chitnis, & Struve, 2000; Savikhin, Xu, Martinsson, et al., 2001; Shuvalov et al., 1986). In these experiments, ΔA signal contributions from energy transfer processes in the antenna were separated from contributions due to ET in the RC, the latter being blocked whenever RCs are closed. By measuring ΔA spectra with RCs open and closed, then, subtracting the latter from the former, we can isolate the signals stemming from P_{700}^+ formation and consequent ET processes, obtaining more direct information on these, untangled from EET processes.

The experiments presented in this section were performed on the WT and Tyr→Phe mutant PS I samples similarly to DADS measurements specified in Section 4.5, using the fs pump-probe

spectrometer with modifications described in Section 3.2.1. Samples' Q_y absorbance maxima were within 0.68 ± 0.03. The kinetics at 700 nm probe were recorded for RCs that were open and closed, and the differences $\Delta\Delta A$(open - closed) between these were calculated. Kinetic curves were also measured at 685 nm, where a strong ΔA signal was expected at early times based on previous measurements, for open RCs alone. Fixed-time $\Delta\Delta A$ profiles were measured over the 660 – 720 nm range in 1 nm increments for probe delays of 8 ps and 200 ps, and the difference $\Delta\Delta\Delta A$ between these two times was also calculated.

4.7.2   Results

700 nm Dynamics

700 nm ΔA dynamics for PS I with open and closed RCs and the difference between them $\Delta\Delta A$(open - closed) for all Tyr→Phe mutants are shown in Figure 4.20, fitted (smooth curves) with parameters summarized in Table 4.1. The 700 nm signal is expected to be dominated by the signal from the red antenna pigments and the formation of the P_{700}^+ radical. The latter is characterized by a strong PB signal whose risetime represents the apparent excitation trapping by the RC and the formation of the P_{700}^+ radical, followed by the nondecaying (within the time window of the experiment) steady PB signal. Superimposed on that is the PB signal arising from population and depopulation of the red antenna Chl pool, characterized with a risetime of a few picoseconds (energy transfer time from bluer initially excited Chls to red Chls) and a decay time comparable with the P_{700}^+ formation time. The mutual amplitudes of these two components are expected to depend on the number of red Chls in the PS I complex. Because steady-state absorption spectra (see Figure 4.7, Section 4.3.2) already suggest that the number of red Chls may be affected by some mutations, the 700 nm kinetics can serve as a supportive argument for the proposed interpretation. Indeed, Figure 4.20A shows that the short-time PB associated with antenna Chls is markedly stronger in the WT than in the Tyr→Phe mutants, reinforcing the conclusion that the mutant PS I complexes do not assemble with a full set of Chls.
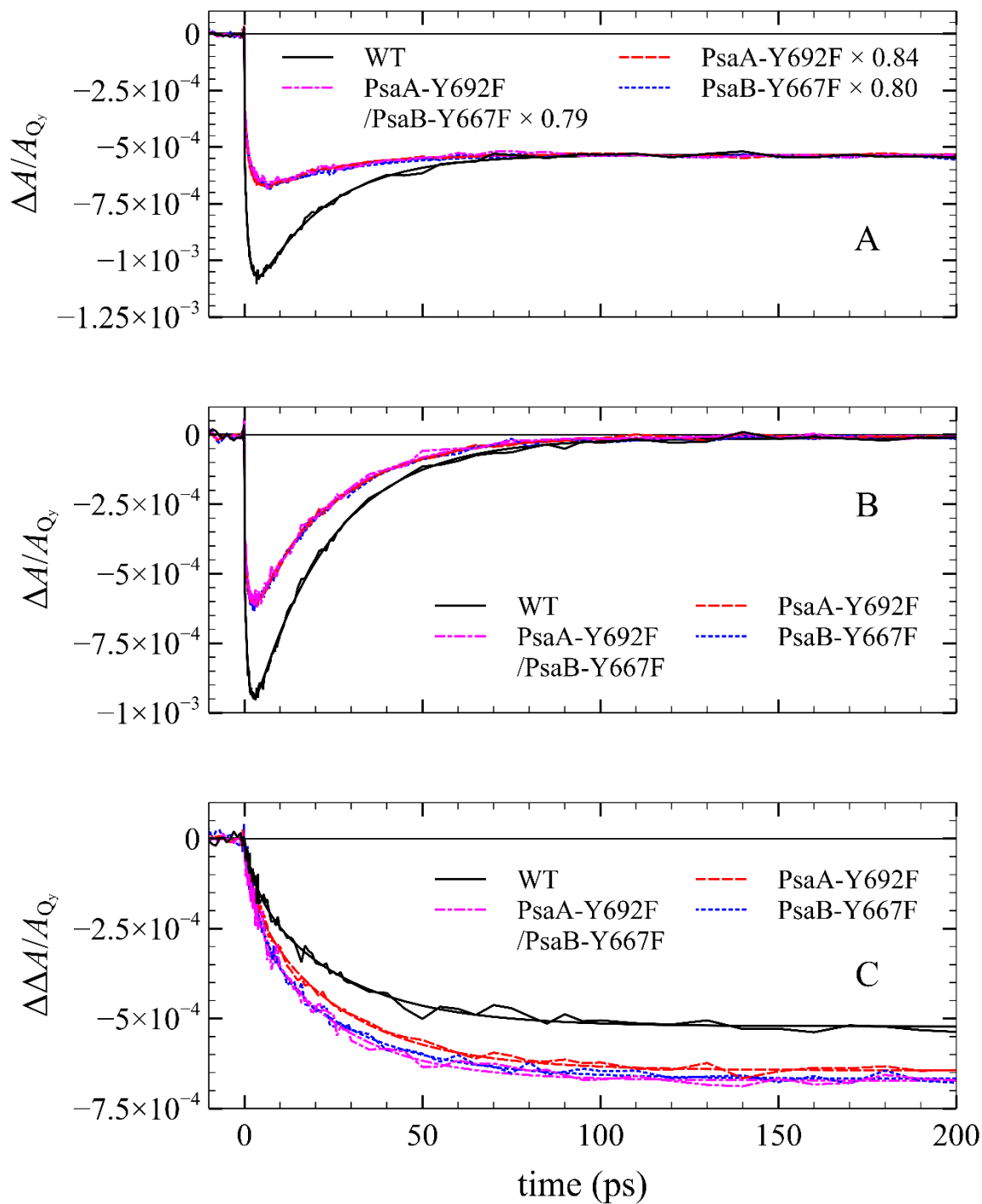
Figure 4.20: 700 nm ΔA kinetics for PS I with open (A) and closed (B) RCs, as well as $\Delta\Delta A$(open - closed) (C) are shown on a common time scale. All have been divided by Q_y maximum absorbance of each sample. The open RC mutant curves have additionally been scaled by factors ~0.8 to match the WT's long-time signal, facilitating shape comparison. The larger signal of WT at short times confirms that the missing pigments belong to the antenna. This is supported by the larger $\Delta\Delta A$ signals for mutants, showing greater P_{700}^+ accumulation.

Table 4.4: Summarized are the fitting parameters for ultrafast 700 nm kinetics for the WT and Tyr→Phe mutants. Decays for open RCs, closed RCs, and the difference between them have each been fitted independently and the results listed below. The shorter components (<5 ps) are ascribed to EET from higher- to lower-energy Chls in the antenna. Only the open RC decays require two such short components for adequate fitting. The second longest component (19 – 28 ps) is associated with the antenna decay time and corresponds to primary CS. The long component represents all processes much slower than the 300 ps scope of the experiment. This represents only approximately 1% of the total amplitude of the closed RC signal, showing that the 532 nm laser illumination closed a vast majority but not a totality of the RCs.

P_{700} state→	open		closed		open - closed	
strain ↓	lifetime (ps)	relative amplitude (%)	lifetime (ps)	relative amplitude (%)	lifetime (ps)	relative amplitude (%)
WT	long	43	long	1	long	100
	20	57	22	99	26	-75
	1.7	-36	1.0	-54	3.7	-20
	0.6	-22				
PsaA-Y692F /PsaB-Y667F	long	72	long	1	long	100
	19	28	22	99	23	-71
	3.2	-28	1.2	-48	3.3	-21
	0.9	-28				
PsaA-Y692F	long	72	long	1	long	100
	19	28	22	99	26	-74
	2.2	-30	1.2	-47	3.4	-20
	0.9	-24				
PsaB-Y667F	long	73	long	1	long	100
	24	27	23	99	28	-59
	2.8	-24	1.1	-46	4.8	-36
	1.1	-30				

The major difference in kinetics with closed RCs is the absence of the long, non-decaying component associated with the formation of P_{700}^+. This is, of course, expected, as P_{700} is pre-oxidized in these experiments and, instead of initiating charge transfer, serves as an excitation quencher. The $\Delta\Delta A$(open - closed) profiles thus isolate signal due to the formation of P_{700}^+ and ET. The (open - closed) kinetics can be fitted with a set of slightly longer lifetimes (and relative amplitudes compared to that of the total signal), which are as follows for WT: 3.7 ps (-20%), 26 ps (-75%), and long (100%). The only notable divergence from this is in the B-branch mutant, whose two shorter-lifetime parameters are 4.8 ps (-36%) and 28 ps (-59%). Kinetics for open RCs at

685 nm are also shown in Figure 4.21, and their fitting parameters are listed side-by-side with those of the 390 nm kinetics in Table 4.5.

Table 4.5: Fitting parameters for WT and Tyr→Phe mutant PS I ultrafast decay kinetics at 685 nm and 390 nm are compared. For the 685 nm probe experiment, only three components were necessary for adequate fitting as the ~0.6 ps component DADS found for the WT in Section 4.5.2 crosses zero around 685 nm. The components have lifetimes 2 – 3 ps corresponding to slow equilibration among bulk antenna Chls, as well as a 28 – 30 ps for antenna decay, and a minor (<10% of total signal amplitude) component encompassing processes not decaying within the experiment's 300 ps timeframe.

probe→	685 nm		390 nm	
strain ↓	lifetime (ps)	relative amplitude (%)	lifetime (ps)	relative amplitude (%)
WT	long	8	long	-29
	28	53	25	90
	2.4	39	7.3	-7
			0.7	10
PsaA-Y692F /PsaB-Y667F	long	9	long	-28
	30	58	27	91
	2.9	33	8.1	-6
			0.8	9
PsaA-Y692F	long	7	long	-31
	29	70	25	91
	2.2	23	8.8	-6
			0.8	8
PsaB-Y667F	long	9	long	-32
	28	60	27	92
	2.8	32	9.7	-5
			1.0	8
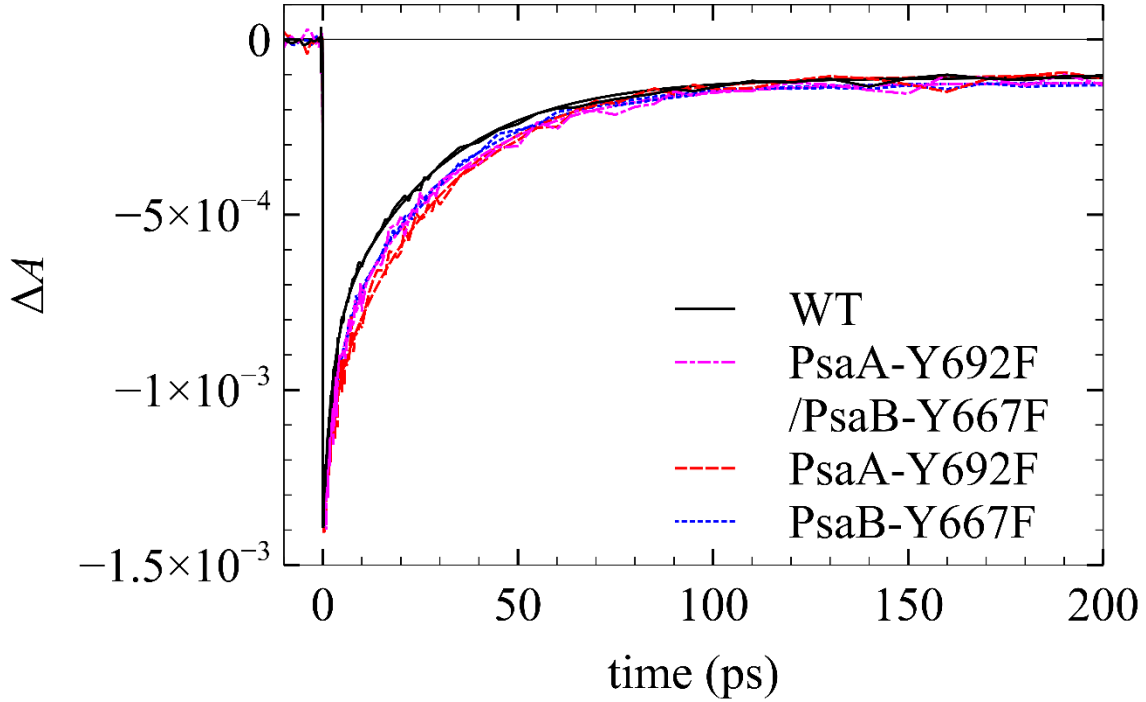
Figure 4.21: Kinetics of WT and Tyr→Phe mutant PS I at 685 nm are scaled to match WT signal at short (~0.2 ps) times. Theoretical fits, shown as smooth curves of matching styles, reveal slightly faster and weaker antenna decay component for WT (28 ps, 53%) than for the mutants (28 – 30 ps, 58% – 70%), amplitudes expressed relative to the respective total signal amplitudes.

Q_y-Region $\Delta\Delta A$ & $\Delta\Delta\Delta A$ Spectra ($P_{700}^+A_0^-$ - $P_{700}^+A_0$)

$\Delta\Delta A$(open - closed) profiles, as mentioned in Section 4.7.1, can reveal spectral changes due to ET processes in PS I by isolating their respective signals from the signals associated with the energy transfer. As discussed previously in this chapter, the major contribution to (open - closed) absorption difference at 700 nm is the formation of the P_{700}^+ radical, whose absorption difference spectrum is maximized at this wavelength (Figure 4.11). Upon formation of P_{700}^+, the electron is expected to rapidly transfer to A_0, whose lifetime (due to subsequent ET to A_1) is comparable with the antenna lifetime and thus, its kinetics are not readily distinguishable in the ΔA signals measured for open RCs. However, it has been shown that at ~8 ps, the population of A_0^- is maximized, and thus, one should expect a spectral signature specific to A_0 absorption at this time (Savikhin, Xu, Martinsson, et al., 2001). To visualize the A_0 optical spectrum, we measured $\Delta\Delta A$(open - closed) spectra at fixed time delays:8 ps, when, along with P_{700}^+, there is also A_0^- (i.e., $P_{700}^+A_0^-$), and 200 ps, when the electron has proceeded to the secondary acceptor ($P_{700}^+A_1^-$). As A_1 is a PhQ and does not absorb in the studied spectral range—where subsequent

97

acceptors also do not absorb—the only difference in the shape of the spectra is due to the presence of A_0^- in 8 ps spectra.
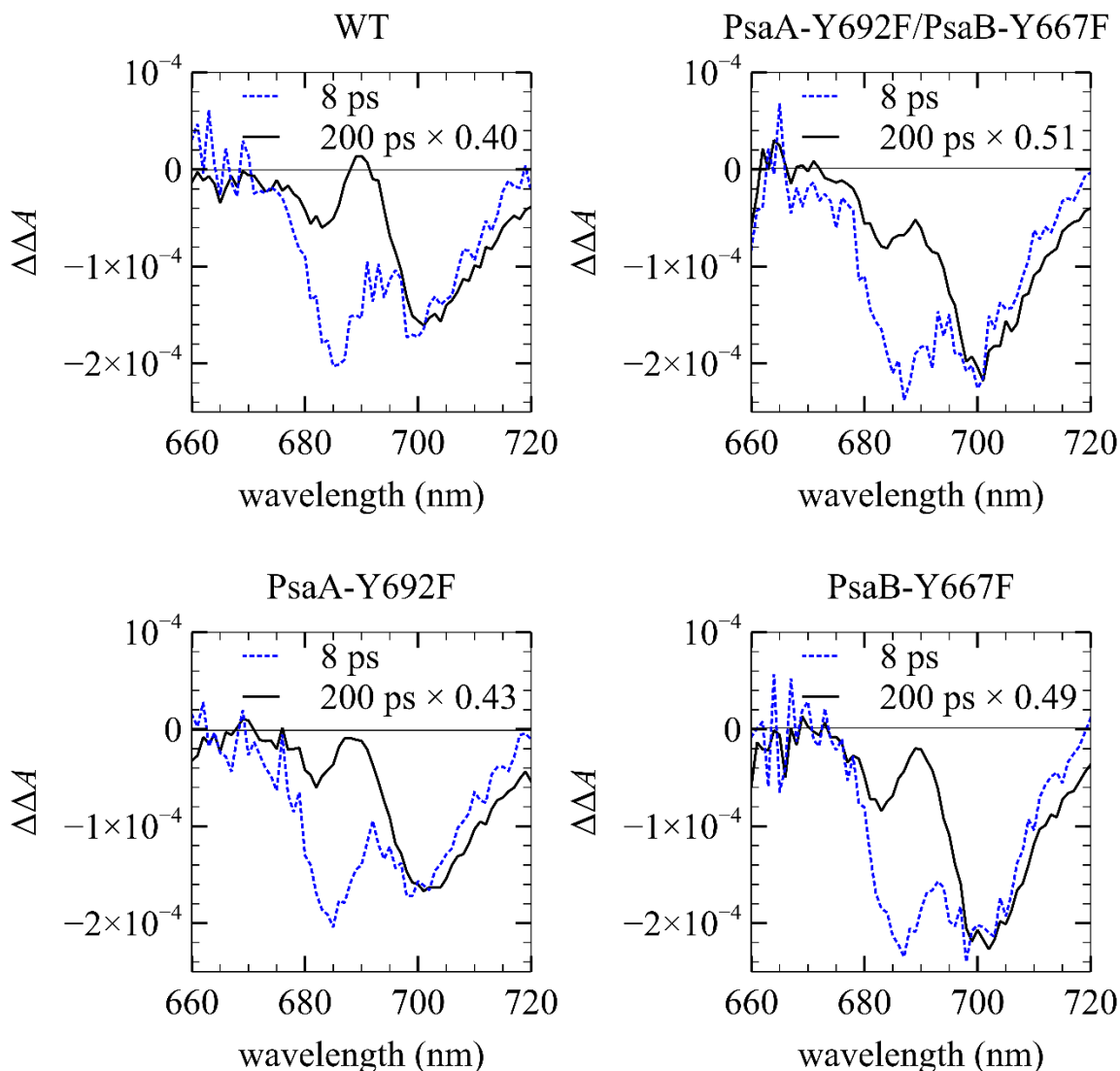
Figure 4.22: Transient $\Delta\Delta A$ (open - closed) spectra of WT and Tyr→Phe mutants of PS I are plotted 8 ps (dotted blue) and 200 ps (solid black) after excitation at 660 nm. The 200 ps spectra are scaled to match the 8 ps signals at 700 nm, resulting in a difference between them of a single absorption band (see Figure 4.24). The 200 ps spectra, with their 700 nm PB bands and 690 nm absorption, resemble the steady-state $(P_{700}^+ - P_{700})$ spectra, to which they are compared in Figure 4.23
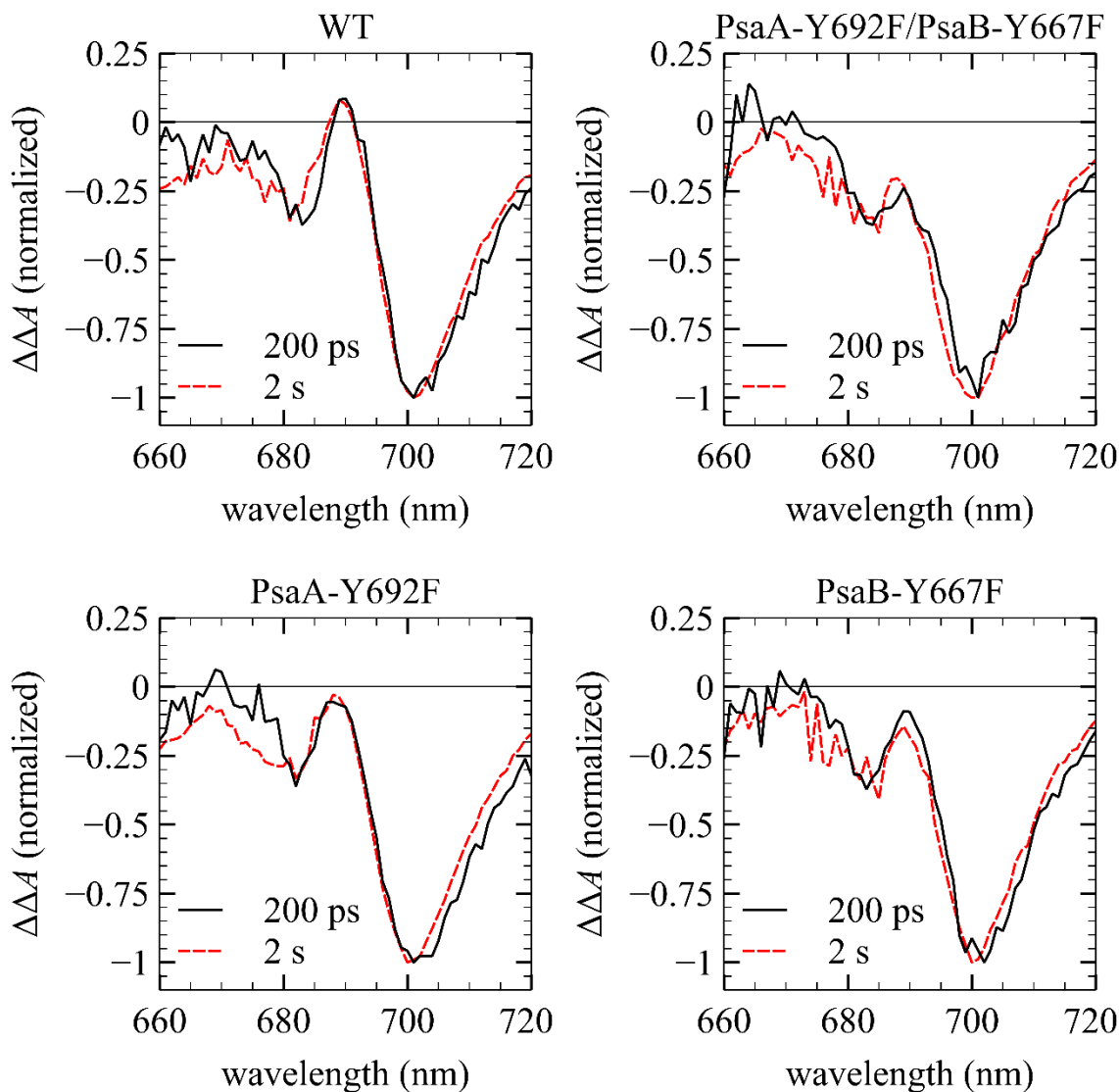
Figure 4.23: The WT and Tyr→Phe mutant $\Delta\Delta A$ spectra 200 ps after excitation at 660 nm (see Figure 4.22) are compared with corresponding $(P_{700}^+ - P_{700})$ spectra (see Figure 4.11) after both have been normalized by the 700 nm band's amplitude. Both spectra are dominated by the 700 nm PB band and show a smaller absorption band at 690 nm. This 690 nm feature is somewhat weaker in both single mutants and much weaker in the double mutant, quite possibly as a result of slightly perturbed excitonic interactions among RC Chls.

Profiles for WT and Tyr→Phe mutant PS I over the 660 – 720 nm range are shown for fixed time delays of 8 ps (dotted blue curves) and 200 ps (solid black curves) in Figure 4.22. The 8 ps signals are as measured under the specified experimental conditions whereas the 200 ps curves have been scaled to match these at 700 nm. Following Savikhin, Xu, Martinsson, et al. (2001), the

scaling factor is interpreted as the amount of P_{700}^+ formed by 8 ps compared to the amount at 200 ps. This ratio is 0.40 for WT PS I and up to 0.51 for the double mutant. At 8 ps, when ET has proceeded to A_0 but not yet to A_1 in a large portion of RCs, an ~11 nm-wide bleaching band, centered around 685 nm for the WT (685 – 687 nm for mutants), was observed in all PS I variants and ascribed to the A_0's Q_y electronic transition.
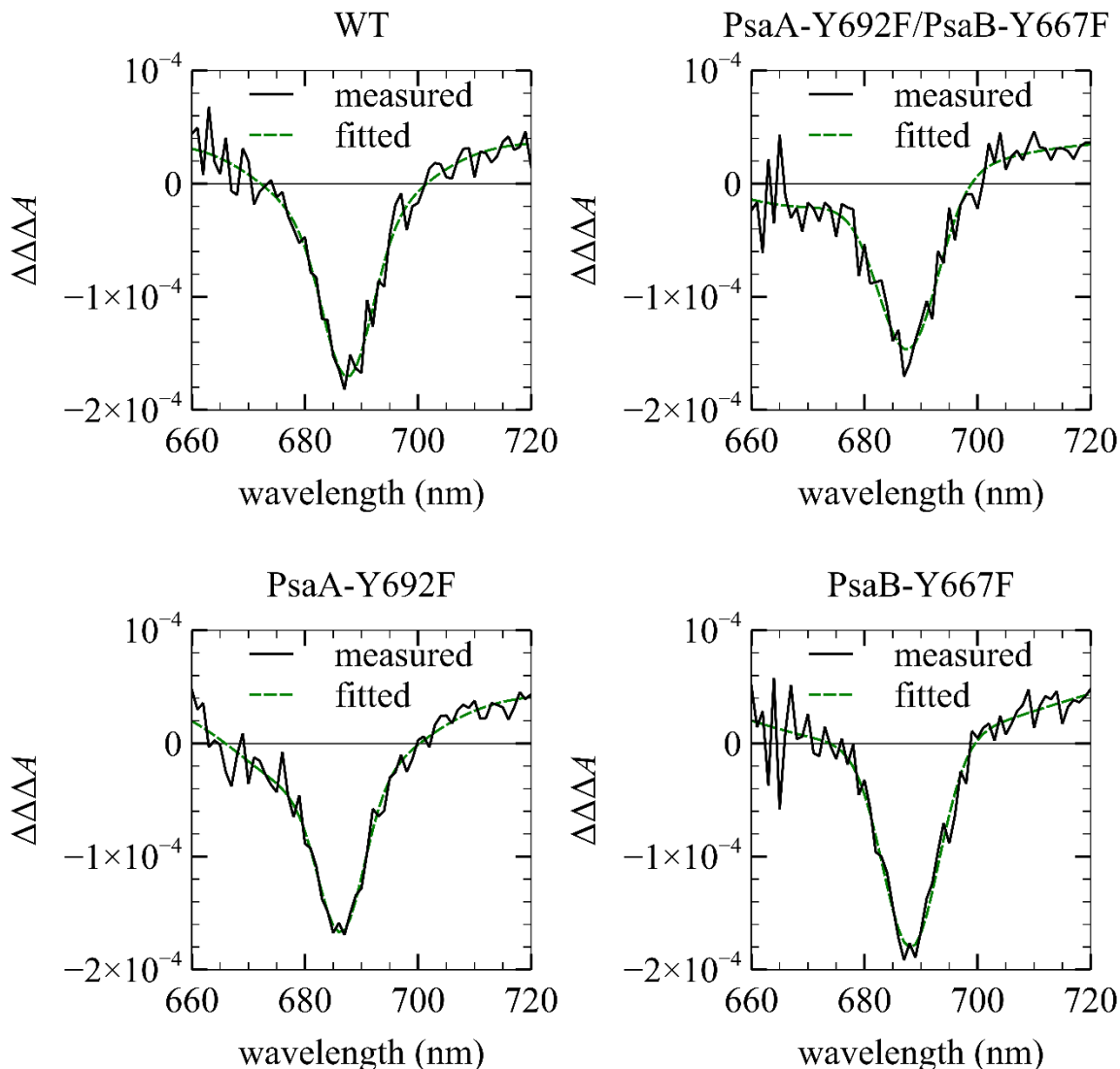
Figure 4.24: $\Delta\Delta\Delta A$ signals for WT and Tyr→Phe mutants of PS I were obtained by subtracting $\Delta\Delta A$ spectra at 8 ps from those at 200 ps (see Figure 4.22). Each curve is fitted with a sum of two Gaussians, narrow and wide. The single narrow (10 nm FWHM) band at 688 nm is attributed to A_0.

Spectra at both delay times contain a bleaching band at 700 nm corresponding to that observed in the (P_{700}^+ - P_{700}) spectra (Figure 4.11). In fact, the 200 ps spectra resemble these, as by 200 ps, electrons have moved on from A_0^-, and subsequent cofactors do not absorb at these wavelengths. The familiar ~690 nm absorption band (691 nm center, 9 nm FWHM, in WT) was thus also visible at 200 ps. Figure 4.23 compares both spectra, normalized at 700 nm. The 690 nm band is somewhat weaker in the single mutants and much weaker in the double mutant. Triplet state formation could be suspected as the culprit of this effect as in the axial ligand double mutants; however, as the Tyr→Phe mutations affect neither A_1 reduction nor long-living P_{700}^+ formation, altered excitonic interactions among the RC Chls are more likely responsible.

Subtracting the scaled $\Delta\Delta A$ spectra at 200 ps from those at 8 ps yielded the $\Delta\Delta\Delta A$ spectra plotted in Figure 4.24. These show a broad absorption feature at wavelengths longer than 700 nm, attributed to A_0^-, in addition to the sharp PB peaks. A two-Gaussian fit, (dashed green) places the sharp A_0 absorption band at 688 nm, with width 10 nm for the WT, similar to the A_0 bleaching band at 686 – 687 nm found by Hastings, Hoshina, et al (1995) and Hastings, Kleinherenbrink, et al. (1994), and farther red than the ~685 nm reported by White et al. (1996) Chauvet, Dashdorj, et al. (2012), and Savikhin, Xu, Martinsson, et al. (2001).

4.8   Discussion

This section elaborates on the two parallel studies of the Asn→Met and Met→His mutations in the quest to understand their impacts on the PS I RC and, more importantly, shed light on the role of A_{-1} in primary CS.

4.8.1   Confirmation of Cyanobacterial PS I RC's Preference for CS Along A-Branch

Findings from our experiments generally show greater effects of mutations targeting the RC's A-branch than of those targeting the B-branch. For all three mutant families, this is confirmed in the steady-state (P_{700}^+ - P_{700}) spectra, whose P_{700}^+ bleaching bands at 700 nm are all more intense for the B-branch mutants than for their corresponding A-branch mutants. In the Asn→Met mutant family, the long component DADS is weaker for the A-branch mutant than for its B-branch counterpart, indicating lower P_{700}^+ yield (see Figure 4.13). Similarly, the Met→His B-branch mutant's long DADS resembles that of the WT PS I in shape, whereas the corresponding A-branch

DADS is visibly distorted, with its 690 nm absorption feature largely missing (see Figure 4.15). In the 390 nm kinetics, the positive nondecaying component corresponding to A_1 reduction also has a marginally larger amplitude for B-branch mutants than for A-branch mutants of the Asn→Met and Tyr→Phe varieties. These results all agree with the consensus that CS in the PS I RC takes places primarily along the A-branch.

4.8.2 Special Pair Triplet State Formation & Altered CS Branching

For both axial ligand mutant families, the long component DADS of the B-branch variants closely resemble the (P_{700}^+ - P_{700}) spectra, whereas the A-branch variants' DADS show visible discrepancies, namely stronger bleaching bands around $680 – 685$ nm or weaker absorption features at 690 nm (see Figure 4.14 and Figure 4.16). These differences are greatly amplified in the case of the double mutants, whose $680 – 685$ nm bands are more intense than those at 700 nm. Excitation of both double mutant PS I complexes is therefore thought to result primarily not in P_{700}^+ but in $^TP_{700}^*$. Using the 390 nm kinetics, it is possible to calculate the approximate ratio of electrons properly transferred along either branch to those recombining with the special pair to form such a triplet state. Because A_1 reduction dominates ΔA in this region, unlike P_{700}^+ (Brettel, 1988; Brettel & Vos, 1999; Dashdorj, Xu, Cohen, et al., 2005; Giera et al., 2009; Lüneberg et al., 1994), the amplitude of the nondecaying positive component from A_1^- can be compared to the negative signal from the antenna immediately after excitation. Assuming 100% efficiency of A_1^- formation in the WT, the Asn→Met single mutants performed about equally well, whereas in the double mutant, whose long component is ~3 times weaker, nearly ⅔ of electrons can be inferred to turn back before arriving at A_1, recombining with P_{700}^+ instead to form $^TP_{700}^*$. The situation is worse for the Met→His double mutant, whose corresponding long component is ~6 times weaker than that of the WT. The single mutants' virtually unaffected A_1^- yields can be explained by redistributions of ET, which proceeds almost exclusively along the unaltered branch. Note that the redirection of ET from a damaged branch to an intact one may be a significant evolutionary advantage, which helps to explain how an RC structure featuring two active branches has survived over countless generations despite the additional cost to organisms of assembling both branches. Without compensation by the intact branch, and assuming that the A- and B-branches remained responsible for a respective 65% and 35% of CS in this system, (Sétif & Brettel, 1993), the A_1^- yields of the Asn→Met A- and B-branch mutants would not exceed 57% and 77%, respectively

(or 46% and 71% in the case of Met→His mutants)—much less than seen in Figure 4.17 (or Figure 4.18). These numbers account for a ⅓-efficient Asn→Met mutated branch in each case (or ⅙ for Met→His), though it is not clear from the double mutant experiment that each mutated branch independently exhibits this efficiency. Note, however, that though a long-lived P_{700}^+ state does not affect 390 nm absorption significantly, $^{T}P_{700}^*$ may, and future ns – μs-scale experiments might help to confirm or refine our conclusions about branching, taking advantage of the tenfold difference in F_X reduction time from PhQ-A (~200 ns) compared to PhQ-B (~20 ns) (Brettel, 1988; Joliot & Joliot, 1999; Mathis & Sétif, 1988; Sétif & Brettel, 1993).

4.8.3   Double Axial Mutation Consequences for Affected Organisms

With or without glycose, axial ligand double mutant bacteria were reported to fail to grow in the presence of light, which can effectively kill photosynthetic organisms unable to use its energy. Our measurement of the (P_{700}^+ - P_{700}) spectrum (Figure 4.9) shows that some ET to the terminal acceptors still occurs, albeit insufficiently for sustaining the organism. Together, DADS and 390 nm kinetics (Sections 4.5 – 4.6) suggest that most electrons recombine with the oxidized special pair instead of reaching A_1, thus giving rise to the long-living triplet state $^{T}P_{700}^*$ identified from the long component DADS. This triplet state's spectra are clearly distinct from those of P_{700}^+, as highlighted in Figure 4.14 and Figure 4.16.

4.8.4   Mutation-Induced Redox Potential Shifts & Nature of the First ET Step

With the exact role of A_{-1} an open question as of this writing, various groups have proposed that A_{-1} is the true primary electron donor, reducing A_0 before oxidizing P_{700}, giving the sequence $(P_{700}A_{-1}A_0)^* \rightarrow P_{700}A_{-1}^+A_0^- \rightarrow P_{700}^+ A_{-1} A_0^-$ (Holzwarth et al., 2006; Li et al., 2006; Müller, Niklas, et al., 2003; Müller, Slavov, et al., 2010). Other authors such as Shelaev et al. (2010) oppose this model, also contradicted by the results presented here. Our conclusion that A_{-1} is the likely true primary electron acceptor relies on ET theory from Section 2.4 paired with careful consideration of the effects of the axial ligand mutations on the redox potentials of the targeted cofactors. This section enumerates various scenarios and proceeds by elimination to explain the data in terms of these questions.

PsaB-N582M & PsaA-N600M

To date, the redox potential of A_{-1}, unlike those of all other PS I RC cofactors, remains sparsely studied both experimentally and theoretically. One initial hypothesis is that because A_{-1} must serve as an intermediary in CS between P_{700}^* and A_0, which are too far apart at 20 Å for direct ET within a few picoseconds, its redox potential should lie between those of these cofactors, in the -1320 – -1010 mV range (Kleinherenbrink et al., 1994; Krabben et al., 2000; Ptushenko et al., 2008; Savikhin & Jankowiak, 2014; Shuvalov, 1976; Vos & van Gorkom, 1988)—this way, each ET step is independently exergonic. The Asn→Met mutations, removing the water axial ligand to A_{-1}, must shift its redox potential outside this range, making one of the two ET steps endergonic. Any smaller redox potential shift would be unlikely to produce such drastic effects as observed in the double mutants.

There are a few reasons to reject the idea that the mutation lowers the redox potential of A_{-1} below -1320 mV. Regardless of A_{-1}'s role in primary CS, ET from A_{-1} to A_0 would not be adversely affected, but the step from P_{700}^* to A_{-1} would become endergonic and therefore much slower, according to Equations (2.59) and (2.61). If A_{-1} is the true primary electron acceptor, the drop in redox potential should impair excitation trapping by the RC: The first ET step would take much longer to achieve, and the excitation energy would remain among antenna Chls for a correspondingly longer time. The DADS associated with excitation trapping, however, was not significantly affected even in the double mutant (see Figure 4.13). Alternatively, if A_{-1} is the primary electron donor, excitation trapping time of even the double mutant should roughly match that of the WT, in agreement with our observations. However, without significant ET from P_{700}^* to A_{-1}, the double mutant's substantial $^TP_{700}^*$ formation within a few hundred picoseconds (see Figure 4.14) would still be surprising: $P_{700}^* \rightarrow {}^TP_{700}^*$ intersystem crossing in Chl, which requires a spin flip by the outer electron, is much slower than this and could not have been detected by our experiments. Lastly, completely blocking ET from P_{700}^* to A_{-1} along one branch could redirect all ET through the intact branch, but steady-state $(P_{700}^+ - P_{700})$ spectra suggest otherwise (see Figure 4.9), as even the single mutants saw less long-living P_{700}^+ formation than did the WT.

The surviving possibility is that the Asn→Met mutation near A_{-1} raises this cofactor's redox potential above that of A_0, as shown in Figure 4.25 (left). This conclusion agrees with Ptushenko et al. (2008), who have reported that a water axial ligand to Chl contributes between -110 mV and -90 mV to its redox potential. This should mildly facilitate ET from P_{700}^* to

A_{-1} but hinder the step from A_{-1} to A_0. If A_{-1} is the primary electron donor, again, the excitation trapping time should significantly increase, a result not observed in our experiments. The only remaining explanation, compatible with all results on the Asn→Met mutants, is that A_{-1} is the true primary electron acceptor. The excitation trapping time is then not affected, and electrons reaching A_{-1} from P_{700}^* can either proceed forward to A_0 or recombine with P_{700}^+ to form $^TP_{700}^*$, the latter process being clearly favored as shown by double mutant long component DADS.

Hartzler, Niedzwiedzki et al. (2014) and Hartzler, Slipchenko, and Savikhin (2018) have measured the energy of the excited triplet state for monomeric Chl a to lie 272 meV below that of the singlet excited state, with an additional ~40 meV difference for a strongly interacting pair of Chls a such as P_{700}. The cumulative 312 meV energy difference between P_{700}^* and $^TP_{700}^*$ places the latter's redox potential around -1008 mV, ignoring the two Chls' mutual orientation (Hartzler, Slipchenko, & Savikhin, 2018)—above, and possibly very close to A_0's redox potential. This is in line with the observation that traveling along a mutated RC branch, a portion of the electrons do proceed to A_0 instead of recombining with P_{700}^+ to form $^TP_{700}^*$. The slow reduction of A_1 observed in the 390 nm kinetics can help to quantify A_{-1}'s redox potential along the mutated branch. Despite that the mutation is assumed to alter only A_{-1}'s redox potential and not affect the $A_0^-{\rightarrow}A_1$ ET rate directly, the population rate of the A_1^- state still depends on the availability of its electron donor A_0^-. The exponential fit components corresponding to slow A_1 reduction have lifetimes of the order of 100 ps, roughly 10 times as long as the expected lifetime in WT PS I. This means that the A_0^- state in the mutated branch is populated ~10 times less than the A_{-1}^- state, so the equilibrium constant between these is $K = [A_{-1}^-A_0]/[A_{-1}A_0^-] \approx 10$, as per Equation (2.60). This corresponds to a separation $\Delta G^0 \approx 2\, k_B\, T = 50$ meV between the two states at room temperature.

PsaA-M684H & PsaB-M659H

The logic applied to determine the direction of the A_{-1} redox potential shift resulting from the Asn→Met mutation can easily be applied to the A_0 Met→His mutants to similar ends. Qualitatively, the two families yielded similar results, including decreased long-living P_{700}^+ yield, impaired A_1 reduction, and $^TP_{700}^*$ formation. As before, these effects can all be explained by a lower redox potential for A_0 than for A_{-1}, implying that the Met→His mutation lowers A_0's redox potential below that of A_{-1}, as illustrated in Figure 4.25 (right). This again agrees with Ptushenko et al. (2008), according to whom a His axial ligand, which is stronger, contributes ~-130 mV more

than does a Met axial ligand to a Chl (Sun et al., 2014). The greatest difference between the Asn→Met and Met→His findings is that in the latter, the excitation trapping times found for the A-branch and double mutants were 40 ps and 69 ps, irrefutably longer than the 26 ps identified for the WT. This result can still be explained with A_{-1} as the true primary electron acceptor if its redox potential is close enough to that of P_{700}^{*}. In this case, the electron from P_{700}^{*} may spend similar amounts of time at P_{700}^{*} and A_{-1}^{-}, from which it is largely unable to proceed forward to A_0, and the excitation from P_{700}^{*} may return to the antenna, increasing the observed excitation trapping time.
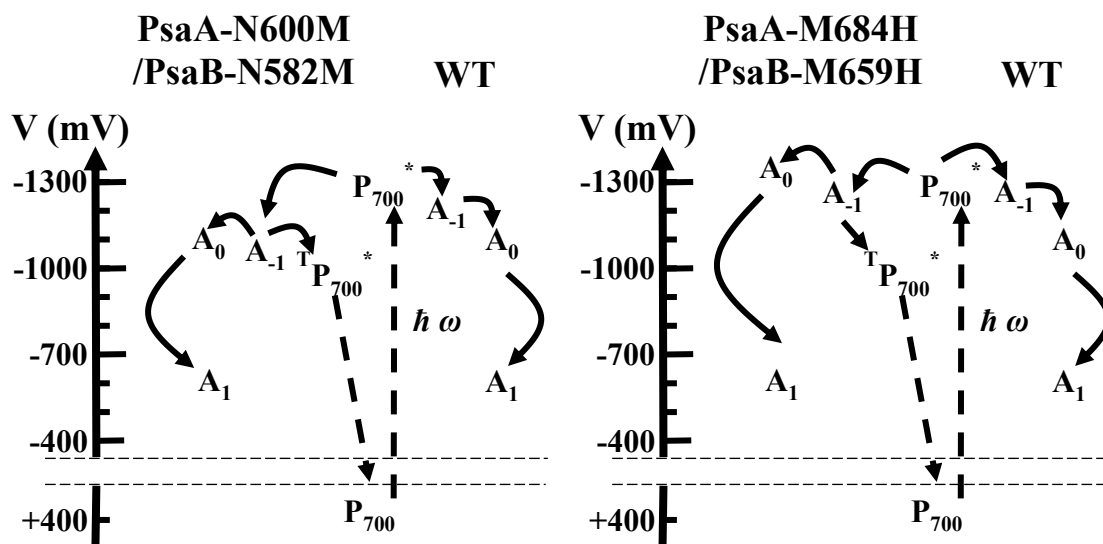
Figure 4.25: Approximate redox potentials are shown for PS I RC cofactors from P_{700} to A_1, and the WT is compared with Asn→Met mutants (left) and Met→His mutants (right). The A_{-1} redox potential in the WT has been placed artificially between those of P_{700}^{*} and A_0, where it likely lies. The redox potential units, mV, can be conveniently multiplied by the electronic charge to obtain the corresponding energies for the electron at any cofactor. Dashed arrows represent state transitions, and solid arrows represent possible ET steps. The Asn→Met mutation makes the A_{-1} redox potential less negative, and the Met→His mutation makes that of A_0 more negative, both resulting in energetically uphill ET from A_{-1} to A_0. Recombination with the special pair from A_{-1}^{-} to form $^{T}P_{700}^{*}$ then becomes a favorable alternative, as observed experimentally.

4.8.5   Conclusions

The data from the axial ligand mutant studies point to the following conclusions. First, A_{-1} appears to be the PS I RC's true first electron acceptor, contrary to conventional naming, so that the primary CS occurs via the $P_{700}^{+}A_{-1}^{-}A_0$ state. Second, the effects of the mutations studied were to raise or lower the affected cofactor's redox potential by respectively weakening (or outright eliminating) or strengthening the axial ligand. Third, in a PS I RC with a severely impaired branch,

the intact branch may take over a large portion of its sister's duties, allowing the photosynthetic organism to survive—this may have helped to preserve the PS I RC's two active branches over the course of evolution.

CHAPTER 5.   (P_{700}^+ - P_{700}) SPECTRUM SIMULATIONS VIA SIX-CHLOROPHYLL MODELING OF THE PS I RC

This brief chapter summarizes our attempts to generate the (P_{700}^+ - P_{700}) spectrum from theoretical models of the PS I RC, based chiefly on exciton theory as established in Section 2.3. For the simulations presented here, the RC was simplified to its six Chls, considering solely dipole-dipole interactions. The transition energies for individual pigments were taken from literature, though as these values are generally not precisely known, several attempts were made with different sets of diagonal energies (Equation (2.23)) in the excitonic Hamiltonian (Equation (2.28)). Similarly, in some cases, off-diagonal terms (Equation (2.29)) were not purely the results of dipole-dipole calculations (Equation (2.22)) but were corrected according to Damjanović et al. (2002); these authors acknowledged that, as noted in Section 2.3.1, the dipole-dipole approximation is expected to be inaccurate for pairs of pigments which are close together, such as the P_{700} Chls. The main conclusion from these excitonic simulations is that simply considering dipole-dipole interactions among the six Chls of the PS I RC is insufficient for building its excitonic Hamiltonian accurately.

The exciton spectra shown in Figure 5.1 were obtained by diagonalizing various excitonic Hamiltonians for the RC as instructed in Section 2.3.2, which produced stick spectra, and applying broadening of 100 cm^{-1} to each band. Chl positions and orientations were taken from the structure by Jordan et al. (2001). The Hamiltonian matrices described by Equations (5.1) – (5.4) list energies in cm^{-1}, and the order of the rows and columns in terms of the pigments they represent is as follows: eC-A1—eC-B1—eC-B2—eC-A2—eC-A3—eC-B3. The spectra in Panel A were generated from a Hamiltonian in which diagonal elements corresponded to absorption at 690 nm, 682 nm and 685 nm for eC-1, eC-2 and eC-3 on either branch, respectively, and all off-diagonal terms were naively treated as dipole-dipole interactions (Equation (5.1)). The Panel B spectra used the Hamiltonian from Damjanović et al. (2002) (Equation (5.2)), which differs in all diagonal terms—to which a spectral shift has been applied to account for environmental effects—and off-diagonal terms representing interactions between pairs of close pigments, for which the dipole-dipole approximation gives dubious values. Panel C spectra correspond to a Hamiltonian (Equation (5.3)) combining elements of the first two: The diagonal energies are from Equation (5.1), whereas the rest matches Equation (5.2). For Panel D, the Hamiltonian (Equation (5.4)) is a truncated form of

Equation (5.1), using only the four elements pertaining to the special pair Chls and the dipole-dipole interactions between them. To imitate P_{700}^+, Hamiltonians in which eC-A1, eC-B1 or both have been deleted were used, and the resulting spectra were subtracted from the previously generated absorption spectra with the aim of recreating the $(P_{700}^+ - P_{700})$ signals. The only simulated $(P_{700}^+ - P_{700})$ spectrum bearing any resemblance to any measured spectra (see Section 4.4.2) is that of Panel D, which considers only special pair Chls and pure dipole-dipole interactions. It displays negative bands near 700 nm and 680 nm and a positive band near 690 nm, though their relative amplitudes do not match those measured. Further modeling will require better knowledge of the spectral properties of PS I cofactors as well as more careful consideration of the nature of the interactions among them.
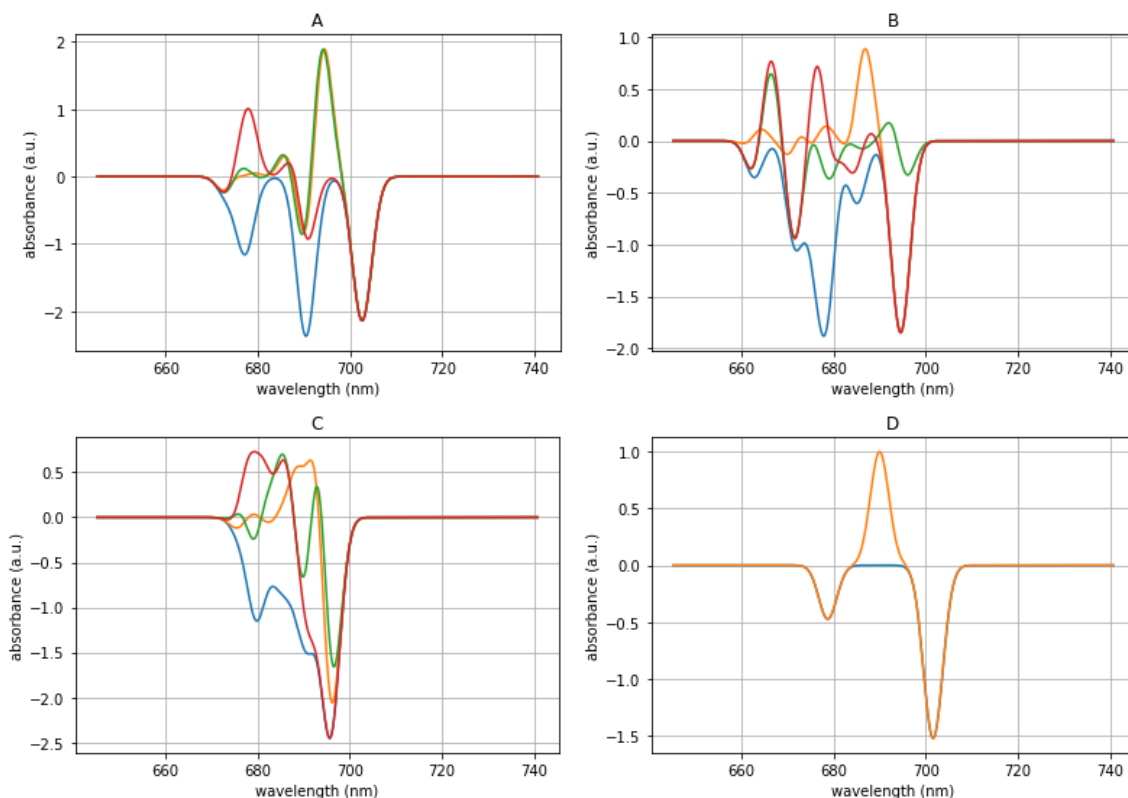
Figure 5.1: Exciton spectra (A – D) have been tentatively simulated based on Hamiltonians described by Equations (5.1) – (5.4). Blue curves are open RC absorption spectra (inverted); yellow, red and green curves correspond to $(P_{700}^+ - P_{700})$ spectra based on Hamiltonians from which eC-A1, eC-B1 or both, respectively, have been deleted. In (D), where only two identical pigments were considered, deleting either one yielded the same spectrum, and deleting both would make for a trivial result.

$$H_{\mathrm{A}} = \begin{bmatrix} 14493 & 240 & -104 & -22 & 15 & 6.7 \\ 240 & 14493 & -21 & -97 & 6.1 & 15 \\ -104 & -21 & 14663 & 29 & 123 & -9.9 \\ -22 & -97 & 29 & 14663 & -11 & 142 \\ 15 & 6.1 & 123 & -11 & 14599 & 2.8 \\ 6.8 & 15 & -9.9 & 142 & 2.8 & 14599 \end{bmatrix} \mathrm{cm}^{-1} \qquad (5.1)$$

$$H_{\mathrm{B}} = \begin{bmatrix} 14455 & 90 & -104 & -22 & 15 & 6.7 \\ 90 & 14943 & -21 & -97 & 6.1 & 15 \\ -104 & -21 & 14711 & 29 & 101 & -9.9 \\ -22 & -97 & 29 & 14996 & -11 & 44 \\ 15 & 6.1 & 101 & -11 & 14647 & 2.8 \\ 6.8 & 15 & -9.9 & 44 & 2.8 & 14754 \end{bmatrix} \mathrm{cm}^{-1} \qquad (5.2)$$

$$H_{\mathrm{C}} = \begin{bmatrix} 14493 & 90 & -104 & -22 & 15 & 6.7 \\ 90 & 14493 & -21 & -97 & 6.1 & 15 \\ -104 & -21 & 14663 & 29 & 101 & -9.9 \\ -22 & -97 & 29 & 14663 & -11 & 44 \\ 15 & 6.1 & 101 & -11 & 14599 & 2.8 \\ 6.8 & 15 & -9.9 & 44 & 2.8 & 14599 \end{bmatrix} \mathrm{cm}^{-1} \qquad (5.3)$$

$$H_{\mathrm{D}} = \begin{bmatrix} 14493 & 240 \\ 240 & 14493 \end{bmatrix} \mathrm{cm}^{-1} \qquad (5.4)$$

APPENDIX A. SHAKER SUPPLEMENTARY MATERIALS

This appendix provides details on the shaker's controls as well as care and maintenance.

Controls

The user interface can display three types of menus: "Select Plate" (the main menu), "Motion settings," and "Motor settings." The "Select Plate" menu has a row of three round, pink buttons labeled "Park," Sapph" and "CaF2" at the top of the screen, each corresponding to a configuration of motion settings saved in memory. To run any of these, press the corresponding pink button, which will become selected and highlighted red.

The motion parameters—center of pattern, size of pattern and pattern size change per cycle—of any of the "Park," "Sapph," and "CaF2" configurations can be changed independently when the respective mode is selected by selecting "Motion settings." To navigate back to the "Select Plate" menu, press the round "Return" button in the bottom right corner of the screen.

Under "Plate center position (mm)"are variables Xc and Yc in mm, defined respectively as $\frac{x_1+x_4}{2}$ and $\frac{y_1+y_4}{2}$ (see Octagonal Motion). Use the left and right arrow buttons below these to adjust them by 1 mm increments within their respective ranges: $0 - 100$ mm for Stage X and $0 - 25$ mm for Stage Y. Note that positions are measured from the stepping motors, meaning higher numbers correspond to lower positions for Stage Y.

Under "Motion amplitude (mm)" are variables D1 and D2, the respective minimum and maximum sizes of the described octagons, equal to $|x_4 - x_1|$ (or equivalently, $|y_4 - y_1|$) (see Octagonal Motion). These can be adjusted in the same fashion as Xc and Yc within a range of $0 - 25$ mm. To immobilize the shaker, set D2 = 0. The controller prevents setting D1 > D2 in two ways: If D1 = D2, attempts to increase D1 have no effect, whereas decreasing D2 also decreases D1 to the same value. If $Xc \pm \frac{D2}{2}$ or $Yc \pm \frac{D2}{2}$ falls outside the corresponding stage's travel range, both stages will freeze as soon as one reaches and attempts to exceed its limit. The shaker will resume motion when either offending parameter is rectified. Note that the maximum allowed value of 25 mm for D1 or D2 (equal to Stage Y's range) will always result in this problem, as Xc and Yc can be only whole numbers of millimeters.

Under "Octagon size step (μm)," is a parameter dD which can be adjusted like the others. This is the amount by which each next octagon described is smaller than its predecessor. The nth octagon has size D = D2 - (n - 1) dD until D ≤ D1, at which point the cycle repeats. Despite the "(μm)" label, the number that appears as dD is in units of 200 μm instead. Setting dD to 10 would thus result in describing a set of octagons each 2 mm smaller in diameter than the previous. dD can, in principle, be varied by increments of 10 over the range of 10 – 1000; however, any value over 120 will invariably result in octagons of constant diameter D2.

The "Motor settings" menu lets the user adjust the cruising speed, acceleration and current of the shaker. These settings are global and do not pertain specifically to the "Park," "Sapph" or "CaF2" configuration.

To set the cruising speed of both stages, press the arrow buttons below the "Cruise speed" field. This allows adjustments by 1 mm/s increments over the range of 2 – 29 mm/s, though speeds exceeding 20 mm/s are not recommended, as they often result in Stage Y eventually losing track of its position and, consequently, shifting its center of oscillation. Note that when the octagonal paths devolve into rounded squares for small oscillation amplitudes (see Octagonal Motion, Figure 3.5), the shaker's speed as it rounds a corner dips to $\frac{Cruise\ speed}{\sqrt{2}}$, as geometry dictates, and slower still if the squares become smaller and their corners sharper.

To set the acceleration of both stages, press the arrow buttons below the "Acceleration" field. This permits adjustments by 10 mm/s^2 increments over the range of 20 – 240 mm/s^2. Keep the acceleration high enough to allow each stage to reach its cruising speed long before reaching its resting position. It can be shown that this condition will be satisfied provided that D1 × *Acceleration* > (*Cruise speed*)^2. Greater accelerations will also make the shaker's average speed faster and result in motion more closely resembling octagons than rounded squares. Experience shows that 200 mm/s^2 is a reasonable setting at which, combined with 16 mm/s cruising speed, the shaker can run for hours.

To set the current used to drive the shaker, press the arrow buttons below the "Current" field. This field indicates the amount of current supplied to the shaker as a percentage of the total available. This number can be set within the range of 18 – 100% in 5% increments. This means that if the current was set to 18% more recently than 100%, it can be adjusted to 23%, 28%, 33% and so forth all the way to 98% and 100%. Conversely, if the current was more recently at 100%,

its available values are 18% and all greater multiples of 5%. It is difficult to imagine an experiment benefited by using less than 100% of the available current to drive the shaker, but testing shows that settings short of 60% cause the device to immediately and audibly malfunction as the stepping motors promptly become stuck.

At the bottom of the "Motor settings" menu, left of the "Return" button, is a "Bonus" button leading to a hidden menu from which a modest selection of music can be played to enhance the user's working conditions. This feature having no effect on the shaker; however, it lies beyond the scope of this work, and investigation of its details is left as an exercise for the reader.

Each translation stage's motor has a manual control knob which can be used if the controller is disconnected from power or from the shaker. The indicator near the knob should glow green instead of red, in this case. This is especially useful for ensuring that the motion space of the shaker and its attachments is completely clear of obstacles whenever the shaker's position, attachments or surroundings have changed, and damage to all of these can thus be prevented. Make sure to home each stage first to give it access to its full travel range. Return each control knob to its neutral position before connecting the controller, or the conflicting commands may damage the motors.

Care & Maintenance

The shaker may run smoothly for hours at a time if properly maintained. Two of the most sensitive parts are the rotating lead screws of both stages, especially that of Stage X, which is much more exposed due to its length and more likely to collect dust due to its horizontal orientation. In addition to minimizing the amount of dust in the environment—practice which benefits all optics—keep the shaker covered whenever possible. Remove any dust using compressed air from a can. Listen for unusual noise such as squeaking but avoid applying any object or substance to the lead screws without first consulting the manufacturer. Super Lube® multi-purpose synthetic oil has been used with possible benefits and no ill effects. It can be applied gradually without spilling using a micropipette with a tip designed for volumes up to 100 μL. Add small amounts at a time and run the stage back and forth several times to spread the lubricant. If signs of rust appear on the rails, contact the manufacturer.

APPENDIX B. ADDITIONAL DATA

This appendix is a compilation of (P_{700}^+ - P_{700}) spectra measured for mutants not studied in any further depth in this work. Figure B1 shows these spectra for all nine A_{-1} mutants available, justifying the selection of the Asn→Met variants for ultrafast spectroscopy. Figure B2 shows the spectrum for the PsaB-W664F mutant, in which a tryptophan (Trp, W) residue near an 11-water molecule cluster between the two A_1 PhQs has been changed to Phe. Figure B3 shows the (P_{700}^+ - P_{700}) spectra for four pairs single mutants in which connecting Chls were targeted.
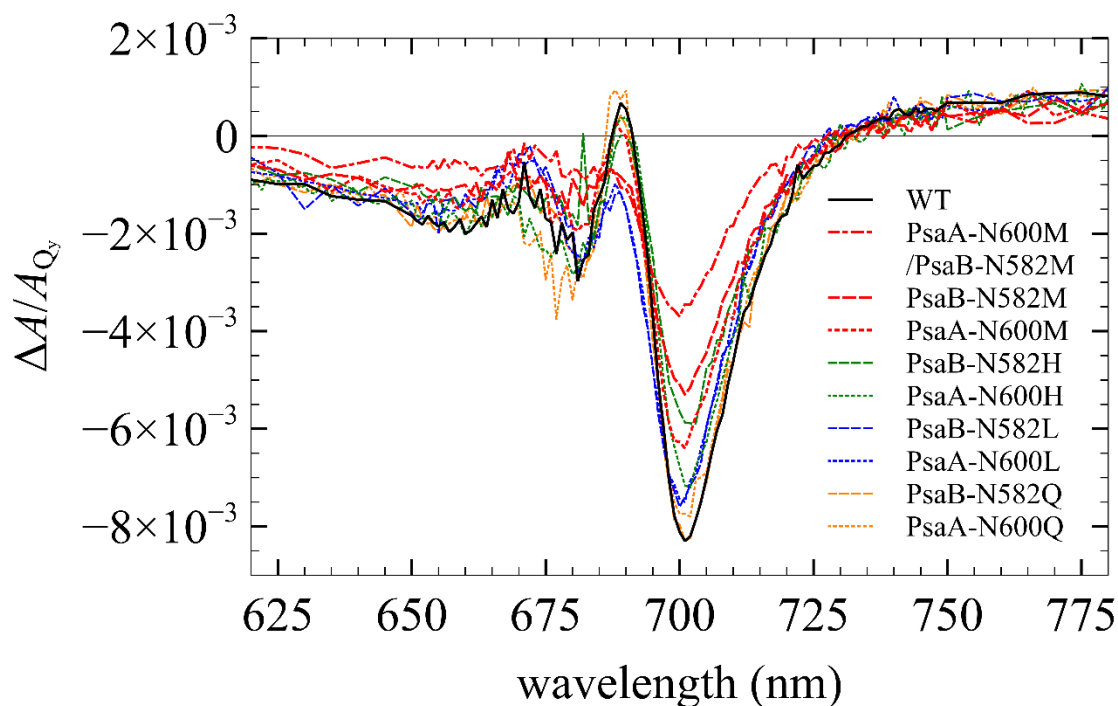
Figure B.1: (P_{700}^+ - P_{700}) spectra for all A_{-1} mutants are compared, confirming the set of single Asn→Met mutants form the least long-living P_{700}^+. This result is the basis for selecting this pair of mutants and the corresponding double mutant for more complex experiments.
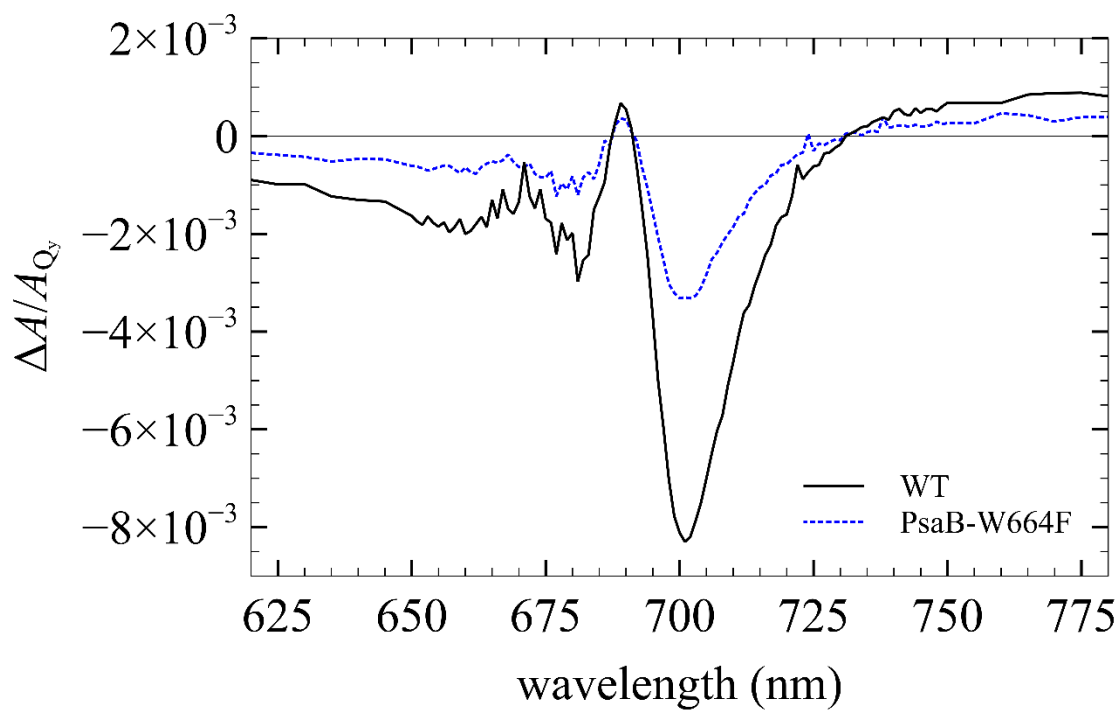
Figure B.2: (P_{700}^+ - P_{700}) spectra for WT and PsaB-W664F
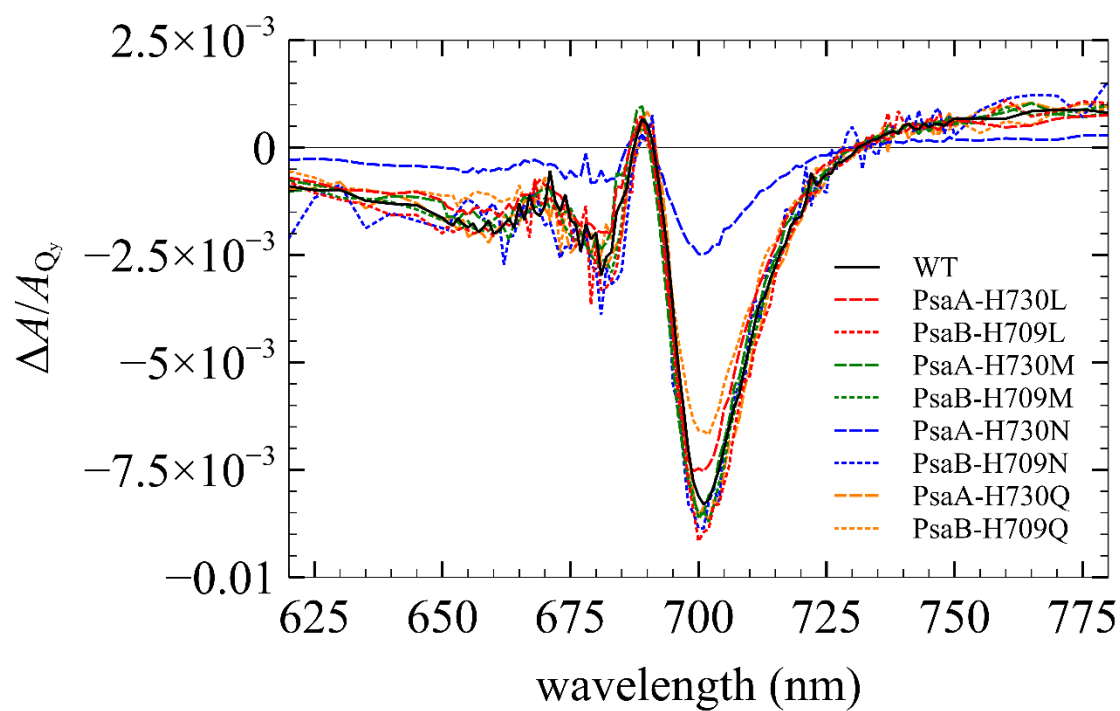
Figure B.3: (P_{700}^+ - P_{700}) spectra for connecting Chl mutants

REFERENCES

Amunts, A., Drory, O., & Nelson, N. (2007). The structure of a plant photosystem I supercomplex at 3.4 Å resolution. *Nature, 447*(7140), 58-63.

Amunts, A., Toporik, H., Borovikova, A., & Nelson, N. (2010). Structure determination and improved model of plant photosystem I. *Journal of Biological Chemistry, 285*(5), 3478-3486.

Badshah, S. L., Sun, J., Mula, S., Gorka, M., Baker, P., Luthra, R., . . . Redding, K. E. (2018). Mutations in algal and cyanobacterial Photosystem I that independently affect the yield of initial charge separation in the two electron transfer cofactor branches. *Biochimica et Biophysica Acta (BBA)-Bioenergetics, 1859*(1), 42-55.

Bautista, J. A., Rappaport, F., Guergova-Kuras, M., Cohen, R. O., Golbeck, J. H., Wang, J. Y., . . . Diner, B. A. (2005). Biochemical and Biophysical Characterization of Photosystem I from Phytoene Desaturase and ζ-Carotene Desaturase Deletion Mutants of Synechocystis Sp. PCC 6803 EVIDENCE FOR PsaA- AND PsaB-SIDE ELECTRON TRANSPORT IN CYANOBACTERIA. *Journal of Biological Chemistry, 280*(20), 20030-20041.

Berera, R., van Grondelle, R., & Kennis, J. T. (2009). Ultrafast transient absorption spectroscopy: principles and application to photosynthetic systems. *Photosynthesis research, 101*(2-3), 105-118.

Berthold, T., Donner von Gromoff, E., Santabarbara, S., Sehle, P., Link, G., Poluektov, O. G., . . . Kothe, G. (2012). Exploring the electron transfer pathways in photosystem I by high-time-resolution EPR: Observation of the B-side radical pair P700+ A1B–in whole cells of the deuterated green alga Chlamydomonas reinhardtii at cryogenic temperatures. *Journal of the American Chemical Society, 134*(12), 5563-5576.

Blankenship, R. E. (2013). *Molecular mechanisms of photosynthesis.* John Wiley & Sons.

Bolton, J. R., & Archer, M. D. (1991). Basic electron-transfer theory. In J. R. Bolton, N. Mataga, & G. McLendon (Eds.), *Introduction to Electron Transfer in Inorganic, Organic and Biological Systems* (pp. 7-23).

Breton, J., Nabedryk, E., & Leibl, W. (1999). FTIR study of the primary electron donor of photosystem I (P700) revealing delocalization of the charge in P700+ and localization of the triplet character in 3P700. *Biochemistry, 38*(36), 11585-11592.

Brettel, K. (1988). Electron transfer from A1− to an iron-sulfur center with t= 200 ns at room temperature in photosystem I Characterization by flash absorption spectroscopy. *FEBS letters, 239*(1), 93-98.

Brettel, K. (1997). Electron transfer and arrangement of the redox cofactors in photosystem I. *Biochimica et Biophysica Acta (BBA)-Bioenergetics, 1318*(3), 322-373.

Brettel, K., & Leibl, W. (2001). Electron transfer in photosystem I. *Biochimica et Biophysica Acta (BBA)-Bioenergetics, 1507*(1-3), 100-114.

Brettel, K., & Vos, M. H. (1999). Spectroscopic resolution of the picosecond reduction kinetics of the secondary electron acceptor A1 in photosystem I. *FEBS letters, 447*(2-3), 315-317.

Brodeur, A., & Chin, S. L. (1999). Ultrafast white-light continuum generation and self-focusing in transparent condensed media. *Journal of the Optical Society of America B, 16*(4), 637-650.

Byrdin, M., Jordan, P., Krauß, N., Fromme, P., Stehlik, D., & Schlodder, E. (2002). Light harvesting in photosystem I: modeling based on the 2.5-Å structure of photosystem I from Synechococcus elongatus. *Biophysical journal, 83*(1), 433-457.

Byrdin, M., Santabarbara, S., Gu, F., Fairclough, W. V., Heathcote, P., Redding, K., & Rappaport, F. (2006). Assignment of a kinetic component to electron transfer between iron–sulfur clusters FX and FA/B of Photosystem I. *Biochimica et Biophysica Acta (BBA)-Bioenergetics, 1757*(11), 1529-1538.

Cardona, T., Sedoud, A., Cox, N., & Rutherford, A. W. (2012). Charge separation in photosystem II: a comparative and evolutionary overview. *Biochimica et Biophysica Acta (BBA)-Bioenergetics, 1817*(1), 26-43.

Chauvet, A. A., Dashdorj, N., Golbeck, J. H., Johnson, T. W., & Savikhin, S. F. (2012). Spectral resolution of the primary electron acceptor A0 in photosystem I. *The Journal of Physical Chemistry B*, 3380-3386.

Chauvet, A., Jagannathan, B., Golbeck, J. H., & Savikhin, S. (2009). Type I reaction center from the green sulfur bacterium Chlorobium tepidum: is Chl a a primary electron acceptor? *Biophysical Journal, 96*(3), 526a-527a.

Chitnis, P. R. (2001). Photosystem I: function and physiology. *Annual review of plant biology, 52*(1), 593-626.

Cohen, R. O., Shen, G., Golbeck, J. H., Xu, W., Chitnis, P. R., Valieva, A. I., . . . Stehlik, D. (2004). Evidence for asymmetric electron transfer in cyanobacterial photosystem I: analysis of a methionine-to-leucine mutation of the ligand to the primary electron acceptor A0. *Biochemistry, 43*(16), 4741-4754.

Crofts, A. R., & Rose, S. (2007). Marcus treatment of endergonic reactions: a commentary. *Biochimica et Biophysica Acta (BBA)-Bioenergetics, 1767*(10), 1228-1232.

Damjanović, A., Vaswani, H., Fromme, P., & Fleming, G. (2002). Chlorophyll excitations in photosystem I of Synechococcus elongatus. *The Journal of Physical Chemistry B, 106*(39), 10251-10262.

Dashdorj, N., Xu, W., Cohen, R. O., Golbeck, J. H., & Savikhin, S. (2005). Asymmetric electron transfer in cyanobacterial Photosystem I: charge separation and secondary electron transfer dynamics of mutations near the primary electron acceptor A0. *Biophysical journal, 88*(2), 1238-1249.

Dashdorj, N., Xu, W., Martinsson, P., Chitnis, P. R., & Savikhin, S. (2004). Electrochromic shift of chlorophyll absorption in photosystem I from Synechocystis sp. PCC 6803: a probe of optical and dielectric properties around the secondary electron acceptor. *Biophysical Journal, 86*(5), 3121-3130.

De la Rosa, M. A., Molina-Heredia, F. P., Hervás, M., & Navarro, J. A. (2006). Convergent evolution of cytochrome c 6 and plastocyanin. In J. H. Golbeck (Ed.), *Photosystem I* (Vol. 24, pp. 683-696). Dordrecht, Netherlands: Springer.

Dexter, D. (1953). A theory of sensitized luminescence in solids. *The Journal of Chemical Physics, 21*(5), 836-850.

Diaz-Quintana, A., Leibl, W., Bottin, H., & Sétif, P. (1998). Electron transfer in photosystem I reaction centers follows a linear pathway in which iron− sulfur cluster FB is the immediate electron donor to soluble ferredoxin. *Biochemistry, 37*(10), 3429-3439.

Du, M., Xie, X., Jia, Y., Mets, L., & Fleming, G. R. (1993). Direct observation of ultrafast energy transfer in PSI core antenna. *Chemical physical letters, 201*(5-6), 535-542.

Fairclough, W. V., Forsyth, A., Evans, M. C., Rigby, S. E., Purton, S., & Heathcote, P. (2003). Bidirectional electron transfer in photosystem I: electron transfer on the PsaA side is not essential for phototrophic growth in Chlamydomonas. *Biochimica et Biophysica Acta (BBA)-Bioenergetics, 1606*(1-3), 43-55.

Förster, T. (1960). Transfer mechanisms of electronic excitation energy. *Radiation Research Supplement*, 326-339.

Fromme, P., & Grotjohann, I. (2006). Structural analysis of cyanobacterial photosystem I. In J. H. Golbeck (Ed.), *Photosystem I: The Light-Driven Plastocyanin: Ferredoxin Oxidoreductase* (pp. 47-69). Dordrecht, Netherlands: Springer.

Fromme, P., Jordan, P., & Krauß, N. (2001). Structure of photosystem I. *Biochimica et Biophysica Acta (BBA)-Bioenergetics, 1507*(1-3), 5-31.

Gatzen, G., Müller, M. G., Griebenow, K., & Holzwarth, A. R. (1996). Primary Processes and Structure of the Photosystem II Reaction Center. 3. Kinetic Analysis of Picosecond Energy Transfer and Charge Separation Processes in the D1− D2− cyt-b559 Complex Measured by Time-Resolved Fluorescence. *The Journal of Physical Chemistry, 100*(17), 7269-7278.

Gibasiewicz, K., Ramesh, V. M., Lin, S., Redding, K., Woodbury, N. W., & Webber, A. N. (2003). Excitonic interactions in wild-type and mutant PSI reaction centers. *Biophysical journal, 85*(4), 2547-2559.

Gibasiewicz, K., Ramesh, V. M., Lin, S., Woodbury, N. W., & Webber, A. N. (2002). Excitation Dynamics in Eukaryotic PS I from Chlamydomonas reinhardtii CC 2696 at 10 K. Direct Detection of the Reaction Center Exciton States. *The Journal of Physical Chemistry B, 106*(24), 6322-6330.

Giera, W., Gibasiewicz, K., Ramesh, V. M., Lin, S., & Webber, A. (2009). Electron transfer from A− 0 to A 1 in Photosystem I from Chlamydomonas reinhardtii occurs in both the A and B branch with 25–30-ps lifetime. *Physical Chemistry Chemical Physics, 11*(25), 5186-5191.

Gobets, B., & van Grondelle, R. (2001). Energy transfer and trapping in photosystem I. *Biochimica et Biophysica Acta (BBA)-Bioenergetics, 1507*(1-3), 80-99.

Gobets, B., Van Stokkum, I. H., Rögner, M., Kruip, J., Schlodder, E., Karapetyan, N. V., . . . van Grondelle, R. (2001). Time-resolved fluorescence emission measurements of photosystem I particles of various cyanobacteria: a unified compartmental model. *Biophysical journal, 81*(1), 407-424.

Golbeck, J. H., & Bryant, D. A. (1991). Photosystem I. In *Current topics in bioenergetics* (Vol. 16, pp. 83-177). Academic Press, Inc.

Grotjohann, I., & Fromme, P. (2005). Structure of cyanobacterial photosystem I. *Photosynthesis research, 85*(1), 51-72.

Guergova-Kuras, M., Boudreaux, B., Joliot, A., Joliot, P., & Redding, K. (2001). Evidence for two active branches for electron transfer in photosystem I. *Proceedings of the National Academy of Science, 98*(8), 4437-4442.

Hartzler, D. A., Niedzwiedzki, D. M., Bryant, D. A., Blankenship, R. E., Pushkar, Y., & Savikhin, S. (2014). Triplet excited state energies and phosphorescence spectra of (bacterio) chlorophylls. *The Journal of Physical Chemistry B, 118*(26), 7221-7232.

Hartzler, D. A., Slipchenko, L. V., & Savikhin, S. (2018). Triplet–Triplet Coupling in Chromophore Dimers: Theory and Experiment. *The Journal of Physical Chemistry A, 122*(33), 6713-6723.

Hasson, K. C. (1997). *Time-resolved studies of the protein bacteriorhodopsin using femtosecond laser pulses.* (Doctoral dissertation, Harvard University).

Hastings, G., Hoshina, S., Webber, A. N., & Blankenship, R. E. (1995). Universality of energy and electron transfer processes in photosystem I. *Biochemistry, 34*(47), 15512-15522.

Hastings, G., Kleinherenbrink, F. A., Lin, S., McHugh, T. J., & Blankenship, R. E. (1994). Observation of the reduction and reoxidation of the primary electron acceptor in photosystem I. *Biochemistry, 33*(11), 3193-3200.

Hastings, G., Reed, L. J., Lin, S., & Blankenship, R. E. (1995). Excited state dynamics in photosystem I: effects of detergent and excitation wavelength. *Biophysical journal, 69*(5), 2044-2055.

Hayes, J. M., Matsuzaki, S., Rätsep, M., & Small, G. J. (2000). Red chlorophyll a antenna states of photosystem I of the cyanobacterium Synechocystis sp. PCC 6803. *The Journal of Physical Chemistry B, 104*(23), 5625-5633.

Hecks, B., Wulf, K., Breton, J., Leibl, W., & Trissl, H.-W. (1994). Primary charge separation in photosystem I: a two-step electrogenic charge separation connected with P700+ A0-and P700+ A1-formation. *Biochemistry, 33*(29), 8619-8624.

Hilborn, R. C. (1982). Einstein coefficients, cross sections, f values, dipole moments, and all that. *American Journal of Physics, 50*(11), 982-986.

Høj, P. B., Svendsen, I., Scheller, H. V., & Møller, B. L. (1987). Identification of a chloroplast-encoded 9-kDa polypeptide as a 2 [4Fe-4S] protein carrying centers A and B of photosystem I. *Journal of Biological Chemistry, 262*(26), 12676-12684.

Holzwarth, A. R., Müller, M. G., Niklas, J., & Lubitz, W. (2006). Ultrafast transient absorption studies on photosystem I reaction centers from Chlamydomonas reinhardtii. 2: mutations near the P700 reaction center chlorophylls provide new insight into the nature of the primary electron donor. *Biophysical journal, 90*(2), 552-565.

Hopfield, J. J. (1974). Electron transfer between biological molecules by thermally activated tunneling. *Proceedings of the National Academy of Sciences, 71*(9), 3640-3644.

Ishikita, H., & Knapp, E.-W. (2003). Redox potential of quinones in both electron transfer branches of photosystem I. *Journal of Biological Chemistry, 278*(52), 52002-52011.

Joliot, P., & Joliot, A. (1999). In vivo analysis of the electron transfer within photosystem I: are the two phylloquinones involved? *Biochemistry, 62*(2), 11130-11136.

Jordan, P., Fromme, P., Witt, H. T., Klukas, O., Saenger, W., & Krauß, N. (2001). Three-dimensional structure of cyanobacterial photosystem I at 2.5 Å resolution. *Nature, 411*(6840), 909-917.

Kamiya, N., & Shen, J.-R. (2003). Crystal structure of oxygen-evolving photosystem II from Thermosynechococcus vulcanus at 3.7-Å resolution. *Proceedings of the National Academy of Sciences, 100*(1), 98-103.

Kasha, M. (1950). Characterization of electronic transitions in complex molecules. *Discussions of the Faraday society, 9*, 14-19.

Kleinherenbrink, F. A., Hastings, G., Wittmershaus, B. P., & Blankenship, R. E. (1994). Delayed fluorescence from Fe-S type photosynthetic reaction centers at low redox potential. *Biochemistry, 33*(10), 3096-3105.

Kouřil, R., van Oosterwijk, N., Yakushevska, A. E., & Boekema, E. J. (2005). Photosystem I: a search for green plant trimers. *Photochemical & Photobiological Sciences, 4*(12), 1091-1094.

Krabben, L., Schlodder, E., Jordan, R., Giacometti, D., Lee, H., Webber, A. N., & Lubitz, W. (2000). Influence of the axial ligands on the spectral properties of P700 of photosystem I: a study of site-directed mutants. *Biochemistry, 39*(42), 13012-13025.

Krieger-Liszkay, A., & Trebst, A. (2006). Tocopherol is the scavenger of singlet oxygen produced by the triplet states of chlorophyll in the PSII reaction centre. *Journal of experimental botany, 57*(8), 1677-1684.

Kumazaki, S., Ikegami, I., Furusawa, H., Yasuda, S., & Yoshihara, K. (2001). Observation of the excited state of the primary electron donor chlorophyll (P700) and the ultrafast charge separation in the spinach Photosystem I reaction center. *The Journal of Physical Chemistry, 105*(5), 1093-1099.

Kumazaki, S., Iwaki, M., Ikegami, I., Kandori, H., Yoshihara, K., & Itoh, S. (1994). Rates of primary electron transfer reactions in the photosystem I reaction center reconstituted with different quinones as the secondary acceptor. *The Journal of Physical Chemistry, 98*(43), 11220-11225.

Kumazaki, S., Kandori, H., Petek, H., Yoshihara, K., & Ikegami, I. (1994). Primary photochemical processes in P700-enriched photosystem I particles: trap-limited excitation decay and primary charge separation. *The Journal of Physical Chemistry, 98*(40), 10335-10342.

Kurisu, G., Zhang, H., Smith, J. L., & Cramer, W. A. (2003). Structure of the cytochrom b6f complex of oxygenic photosynthesis: tuning the cavity. *Science, 302*(5647), 1009-1014.

Lewis, G. N., & Kasha, M. (1944). Phosphorescence and the triplet state. *Journal of the American Chemical Society, 66*(12), 2100-2116.

Li, Y., van der Est, A., Lucas, M. G., Ramesh, V. M., Gu, F., Petrenko, A., . . . Redding, K. (2006). Directing electron transfer within Photosystem I by breaking H-bonds in the cofactor branches. *Proceedings of the National Academy of Sciences, 103*(7), 2144-2149.

Lüneberg, J., Fromme, P., Jekow, P., & Schlodder, E. (1994). Spectroscopic characterization of PS I core complexes from thermophilic Synechococcus sp: Identical reoxidation kinetics of A− 1 before and after removal of the iron-sulfur-clusters FA and FB. *FEBS letters, 338*(2), 197-202.

Mamedov, M. D., Gadzhieva, R. M., Gourovskaya, K. N., Drachev, L. A., & Semenov, A. Y. (1996). Electrogenicity at the donor/acceptor sides of cyanobacterial photosystem I. *Journal of bioenergetics and biomembranes, 28*(6), 517-522.

Marcus, R. A. (1956). On the theory of oxidation-reduction reactions involving electron transfer. I. *The Journal of Chemical Physics, 24*(5), 966-978.

Marcus, R. A., & Sutin, N. (1985). Application of electron-transfer theory to several systems of biological interest. In M. E. Michel-Beyerle (Ed.), *Antennas and Reaction Centers of Photosynthetic Bacteria* (pp. 226-233). Berlin, Heidelberg, New York, Tokyo: Springer-Verlag.

Mathis, P., & Sétif, P. (1988). Kinetic studies on the function of A1 in the Photosystem I reaction center. *FEBS letters, 237*(1-2), 65-68.

McConnell, M. D., Sun, J., Siavashi, R., Webber, A., Redding, K. E., Golbeck, J. H., & van der Est, A. (2015). Species-dependent alteration of electron transfer in the early stages of charge stabilization in Photosystem I. *Biochimica et Biophysica Acta (BBA)-Bioenergetics, 1847*(4-5), 429-440.

Melkozernov, A. N., Su, H., Lin, S., Bingham, S., Webber, A. N., & Blankenship, R. E. (1997). Specific mutation near the primary donor in photosystem I from Chlamydomonas reinhardtii alters the trapping time and spectroscopic properties of P700. *Biochemistry, 36*(10), 2898-2907.

Millqvist-Fureby, A., Larsson, A., Järn, M., Ahniyaz, A., Macakova, L., & Elofsson, U. (2014). Mesoporous solid carrier particles in controlled delivery and release. In *Microencapsulation in the Food Industry* (pp. 299-319). Academic Press.

Moser, C. C., & Dutton, P. L. (1992). Engineering protein structure for electron transfer function in photosynthetic reaction centers. *Biochimica et Biophysica Acta (BBA)-Bioenergetics, 1101*(2), 171-176.

Moser, C. C., & Dutton, P. L. (2006). Application of Marcus theory to photosystem I electron transfer. In J. H. Golbeck (Ed.), *Photosystem I* (Vol. 24, pp. 583-594). Dordrecht, Netherlands: Springer.

Moser, C. C., Keske, J. M., Warncke, K., Farid, R. S., & Dutton, P. L. (1992). Nature of biological electron transfer. *Nature, 355*(6363), 796-802.

Moser, C. C., Page, C. C., & Dutton, P. L. (2006). Darwin at the molecular scale: selection and variance in electron tunnelling proteins including cytochrome c oxidase. *Philosophical Transactions of the Royal Society B: Biological Sciences, 361*(1472), 1295-1305.

Muhiuddin, I. P., Heathcote, P., Carter, S., Purton, S., Rigby, S. E., & Evans, M. C. (2001). Evidence from time resolved studies of the P700+/A1− radical pair for photosynthetic electron transfer on both the PsaA and PsaB branches of the photosystem I reaction centre. *FEBS letters, 503*(1), 56-60.

Müller, M. G., Niklas, J., Lubitz, W., & Holzwarth, A. R. (2003). Ultrafast transient absorption studies on photosystem I reaction centers from Chlamydomonas reinhardtii. 1. A new interpretation of the energy trapping and early electron transfer steps in photosystem I. *Biophysical journal, 85*(6), 3899-3922.

Müller, M. G., Slavov, C., Luthra, R., Redding, K. E., & Holzwarth, A. R. (2010). Independent initiation of primary electron transfer in the two branches of the photosystem I reaction center. *Proceedings of the National Academy of Sciences, 107*(9), 4123-4128.

Nakamura, A., Suzawa, T., Kato, Y., & Watanabe, T. (2005). Significant species-dependence of P700 redox potential as verified by spectroelectrochemistry: comparison of spinach and Theromosynechococcus elongatus. *FEBS letters, 579*(11), 2273-2276.

Nakamura, A., Suzawa, T., Kato, Y., & Watanabe, T. (2011). Species dependence of the redox potential of the primary electron donor P700 in photosystem I of oxygenic photosynthetic organisms revealed by spectroelectrochemistry. *Plant and cell physiology, 52*(5), 815-823.

Nelson, N., & Junge, W. (2015). Structure and energy transfer in photosystems of oxygenic photosynthesis. *Annual review of biochemistry, 84*, 659-683.

Nelson, N., & Yocum, C. F. (2006). Structure and function of photosystems I and II. *Annu. Rev. Plant Biol., 57*, 521-565.

Nujis, A. M., Shuvalov, V. A., van Gorkom, H. J., Plijter, J. J., & Duysens, L. N. (1986). Picosecond absorbance difference spectroscopy on the primary reactions and the antenna-excited states in photosystem I particles. *Biochimica et Biophysica Acta (BBA)-Bioenergetics, 850*(2), 310-318.

Orr, L., & Govindjee. (2010). Photosynthesis online. *Photosynthesis research, 105*(2), 167-200.

Owens, T. G., Webb, S. P., Mets, L., Alberte, R. S., & Fleming, G. M. (1987). Antenna size dependence of fluorescence decay in the core antenna of photosystem I: estimates of charge separation and energy transfer rates. *Proceedings of the National Academy of Sciences, 84*(6), 1532-1536.

Page, C. C., Moser, C. C., Chen, X., & Dutton, P. L. (1999). Natural engineering principles of electron tunnelling in biological oxidation–reduction. *Nature, 402*(6757), 47-52.

Pålsson, L.-O., Flemming, C., Gobets, B., van Grondelle, R., Dekker, J. P., & Schlodder, E. (1998). Energy transfer and charge separation in photosystem I: P700 oxidation upon selective excitation of the long-wavelength antenna chlorophylls of Synechococcus elongatus. *Biophysical journal, 74*(5), 2611-2622.

Penzkofer, A., Beidoun, A., & Lehmeier, H. J. (1993). Spectral superbroadening of self-focused picosecond laser pulses in D2O. *Optical and quantum electronics, 25*(5), 317-349.

Ptushenko, V. V., Cherepanov, D. A., Krishtalik, L. I., & Semenov, A. Y. (2008). Semi-continuum electrostatic calculations of redox potentials in photosystem I. *Photosynthesis Research, 97*(1), 55-74.

Ramesh, V. M., Gibasiewicz, K., Lin, S., Bingham, S. E., & Webber, A. N. (2004). Bidirectional electron transfer in photosystem I: accumulation of A0-in A-side or B-side mutants of the axial ligand to chlorophyll A0. (1375, Ed.) *Biochemistry, 43*(5), 1369.

Ramesh, V. M., Gibasiewicz, K., Lin, S., Bingham, S. E., & Webber, A. N. (2007). Replacement of the methionine axial ligand to the primary electron acceptor A0 slows the A0− reoxidation dynamics in Photosystem I. *Biochimica et Biophysica Acta (BBA)-Bioenergetics, 1767*(2), 151-160.

Rappaport, F., Diner, B. A., & Redding, K. (2006). Optical measurements of secondary electron transfer in photosystem I. In J. H. Golbeck (Ed.), *Photosystem I* (Vol. 24, pp. 223-244). Dordrecht, The Netherlands: Springer.

Redding, K., & van der Est, A. (2006). The directionality of electron transport in photosystem I. In J. H. Golbeck (Ed.), *Photosystem I* (Vol. 24, pp. 413-437). Dordrecht, Netherlands: Springer.

Santabarbara, S., Heathcote, P., & Evans, M. C. (2005). Modelling of the electron transfer reactions in Photosystem I by electron tunnelling theory: The phylloquinones bound to the PsaA and the PsaB reaction centre subunits of PS I are almost isoenergetic to the iron–sulfur cluster FX. *Biochimica et Biophysica Acta (BBA)-Bioenergetics, 1708*(3), 283-310.

Santabarbara, S., Kuprov, I., Fairclough, W. V., Purton, S., Hore, P. J., Heathcote, P., & Evans, M. C. (2005). Bidirectional electron transfer in photosystem I: determination of two distances between P700+ and A1-in spin-correlated radical pairs. *Biochemistry, 44*(6), 2119-2128.

Savikhin, S. (2006). Ultrafast optical spectroscopy of photosystem I. In J. H. Golbeck (Ed.), *Photosystem I* (Vol. 24, pp. 155-175). Dordrecht, Netherlands: Springer.

Savikhin, S., & Jankowiak, R. (2014). Mechanism of primary charge separation in photosynthetic reaction centers. In *The Biophysics of Photosynthesis* (pp. 193-240). New York: Springer.

Savikhin, S., Buck, D. R., & Struve, W. S. (1999). The Fenna-Matthews-Olson protein: a strongly coupled photosynthetic antenna. In D. L. Andrews, & A. A. Demidov (Eds.), *Resonance Energy Transfer* (pp. 399-434). New York: John Wiley & Sons.

Savikhin, S., Xu, W., Chitnis, P. R., & Struve, W. S. (2000). Ultrafast primary processes in PS I from Synechocystis sp. PCC 6803: roles of P700 and A0. *Biophysical Journal, 79*(3), 1573-1586.

Savikhin, S., Xu, W., Martinsson, P., Chitnis, P. R., & Struve, W. S. (2001). Kinetics of charge separation in and A0-→ A1 electron transfer in Photosystem I reaction centers. *Biochemistry, 40*(31), 9282-9290.

Savikhin, S., Xu, W., Soukoulis, V., Chitnis, P. R., & Struve, W. S. (1999). Ultrafast primary processes in photosystem I of the cyanobacterium Synechocystis sp. PCC 6803. *Biophysical journal, 76*(6), 3278-3288.

Schaffernicht, H., & Junge, W. (1981). Analysis of the complex band spectrum of P700 based on photoselection studies with photosystem I particles. *Photochemistry and Photobiology, 34*(2), 223-232.

Scheer, H. (2006). An overview of chlorophylls and bacteriochlorophylls: biochemistry, biophysics, functions and applications. In *Chlorophylls and bacteriochlorophylls* (pp. 1-26). Dordrecht, Netherlands: Springer.

Sétif, P. (2001). Ferredoxin and flavodoxin reduction by photosystem I. *Biochimica et Biophysica Acta (BBA)-Bioenergetics, 1507*(1-3), 161-179.

Sétif, P. Q., & Bottin, H. (1994). Laser flash absorption spectroscopy study of ferredoxin reduction by photosystem I in Synechocystis sp. PCC 6803: evidence for submicrosecond and microsecond kinetics. *Biochemistry, 33*(28), 8495-8504.

Sétif, P., & Brettel, K. (1993). Forward electron transfer from phylloquinone A1 to iron-sulfur centers in spinach photosystem I. *Biochemistry, 32*(31), 7846-7854.

Shelaev, I. V., Gostev, F. E., Mamedov, M. D., Sakisov, O. M., Nadtochenko, V. A., & Semenov, A. Y. (2010). Femtosecond primary charge separation in Synechocystis sp. PCC 6803 photosystem I. *Biochimica et Biophysica Acta, 1797*(8), 1410-1420.

Shuvalov, V. A. (1976). The study of the primary photoprocesses in photosystem I of chloroplasts recombination luminescence, chlorophyll triplet state and triplet-triplet annihilation. *Biochimica et Biophysica Acta (BBA)-Bioenergetics, 430*(1), 113-121.

Shuvalov, V. A., Nujis, A. M., Von Gorkom, H. J., Smit, H. W., & Duysens, L. N. (1986). Picosecond absorbance changes upon selective excitation of the primary electron donor P-700 in photosystem I. *Biochimica et Biophysica Acta (BBA)-Bioenergetics, 850*(2), 319-323.

Struve, W. S. (1995). Theory of electronic energy transfer. In *Anoxygenic photosynthetic bacteria* (pp. 297-313). Dordrecht, Netherlands: Springer.

Sun, J., Hao, S., Radle, M., Xu, W., Shelaev, I., Nadtochenko, V., . . . Golbeck, J. H. (2014). Evidence that histidine forms a coordination bond to the A0A and A0B chlorophylls and a second H-bond to the A1A and A1B phylloquinones in M688HPsaA and M668HPsaB variants of Synechocystis sp. PCC 6803. *Biochimica et Biophysica Acta (BBA)-Bioenergetics, 1837*(8), 1362-1375.

Sutin, N. (1991). Nuclear and Electronic Factors in Electron Transfer: Distance Dependence of Electron-Transfer Rates. In J. R. Bolton, N. Mataga, & G. McLendon (Eds.), *Introduction to Electron Transfer in Inorganic, Organic and Biological Systems* (pp. 25-43).

van Amerongen, H., Valkunas, L., & van Grondelle, R. (2000). *Photosynthetic Excitons*. Singapore: World Scientific.

van Gurp, M., van der Heide, U., Verhagen, J., Piters, T., van Ginkel, G., & Levine, Y. K. (1989). Spectroscopic and orientational properties of chlorophyll a and chlorophyll b in lipid membranes. *Photochemistry and Photobiology, 49*(5), 663-672.

Vassiliev, I. R., Jung, Y.-S., Mamedov, M., AYu, S., & Golbeck, J. H. (1997). Near-IR absorbance changes and electrogenic reactions in the microsecond-to-second time domain in photosystem I. *Biophysical journal, 72*(1), 301-315.

Velthuys, B. R. (1980). Mechanisms of electron flow in photosystem II and toward photosystem I. *Annual Review of Plant Physiology, 31*(1), 545-567.

Vos, M. H., & van Gorkom, H. J. (1988). Thermodynamics of electron transport in Photosystem I studied by electric field-stimulated charge recombination. *Biochimica et Biophysica Acta (BBA)-Bioenergetics, 934*(3), 293-302.

Warshel, A., & Parson, W. W. (2001). Dynamics of biochemical and biophysical reactions: insight from computer simulations. *Quarterly reviews of biophysics, 34*(4), 563-679.

White, N. T., Beddard, G. S., Thorne, J. R., Feehan, T. M., Keyes, T. E., & Heathcote, P. (1996). Primary charge separation and energy transfer in the photosystem I reaction center of higher plants. *The Journal of Physical Chemistry, 100*(29), 12086-12099.

Witt, H., Schlodder, E., Teutloff, C., Niklas, J., Bordignon, E., Carbonera, D., . . . Lubitz, W. (2002). Hydrogen bonding to P700: site-directed mutagenesis of threonine A739 of photosystem I in Chlamydomonas reinhardtii. *Biochemistry, 41*(27), 8557-8569.

Xu, W., Chitnis, P. R., Valieva, A., van der Est, A., Brettel, K., Guergova-Kuras, M., . . . Zybailov, B. (2003). Electron transfer in cyanobacterial photosystem I II. Determination of forward electron transfer rates of site-directed mutants in a putative electron transfer pathway from A0 through A1 to FX. *Journal of Biological Chemistry, 278*(30), 27876-27887.

Yang, G., & Shen, Y. R. (1984). Spectral broadening of ultrashort pulses in a nonlinear medium. *Optics letters, 9*(11), 510-512.

Zouni, A., Witt, H.-T., Kern, J., Fromme, P., Krauß, N., Saenger, W., & Orth, P. (2001). Crystal structure of photosystem II from Synechococcus elongatus at 3.8 Å resolution. *Nature, 409*(6821), 739-743.

VITA

Antoine Martin was born on July 24th, 1990, second of two children to parents Annie and Jean-Paul Martin, in Thouars, France. After growing up halfway there and halfway in Turlock, California, he proceeded to study physics at the University of Wisconsin-Madison, earning a bachelor's degree in May 2012. With this dissertation, he will complete his doctorate in physics in December 2020 from Purdue University.

PUBLICATIONS

This dissertation is published in part based on the following manuscripts.

Manuscripts in preparation:

1. Role of H_2O A_{-1} axial ligand by PsaA-N600M and PsaB N582M mutations in PS I from *Synechocystis* sp. PCC 6803. **A. Martin**, L. Luo, W. Xu, & S. Savikhin.

2. Role of conserved PsaB-Trp664 in photosystem I: Evidence for the Inversion of A_{1A} and A_{1B} midpoint potentials in a Trp→Phe variant of *Synechocystis* sp. PCC 6803. V. Kurashov, L. Luo, **A. Martin**, S. Savikhin, J. H. Golbeck, & W. Xu.

3. Role of the hydrogen bond to the A_0 chlorophyll *a* molecule of photosystem I in *Synechocystis* sp. PCC 6803. W. Xu, L. Luo, **A. Martin**, Y. Wang, A. Chistoserdov, J. H. Golbeck, S. Savikhin, & P. R. Chitnis.

Conference presentation:

1. Role of accessory chlorophylls in photosystem I reaction centers investigated via optical spectroscopy on *Synechocystis* sp. PCC 6803 mutants. **A. Martin**, L. Luo, W. Xu, & S. Savikhin (2020). Presented at the *46th Annual Midwest/Southeast Photosynthesis Conference*.